Mechanotransduction Across Time and Length Scales

Mechanotransduction Across Time and Length Scales

A dissertation presented
by
Max Carlton Darnell
to
The Harvard John A. Paulson School of Engineering and Applied Sciences

in partial fulfillment of the requirements
for the degree of
Doctor of Philosphy
in the subject of
Engineering Sciences: Bioengineering

Harvard University
Cambridge, Massachusetts
May, 2017

Dr. David J. Mooney Max Carlton Darnell

Mechanotransduction Across Time and Length Scales

Abstract

Mechanotransduction is a process that spans both time and length scales, from the nanoscale machines that sense substrate properties, to the morphogenesis and healing of whole organs. Studies of mechanotransduction have generated a wealth of knowledge about the mechanisms of the transmission of mechanical cues and their downstream effects, but these studies have largely been limited in the scope of key experimental parameters and outputs. A more comprehensive view of the mechanisms and implications of mechanotransduction would aid in the design of new therapies to leverage these phenomena. Here, we seek to broaden not only the view of the material parameters that cells can sense, but also the scope of the outputs of this sensing. We first focus on a relatively underexplored material property, stress relaxation, and show that stress relaxation can induce counterintuitive behaviors via the simple clutch mechanism of mechanosensing. We then exploit cells' response to stress relaxation, showing that stress relaxation can be used to tune healing for bone tissue engineering. To integrate this complexity into a coherent picture, we then perform a global transcriptomic analysis of substrate sensing, uncovering relationships between the sensing of different material properties and exploring the extent of their downstream effects. Finally, given these developments in understanding the complexity of cell-material interactions, we propose a biomaterial design

methodology to fully leverage this complexity to maximize functionality of therapeutic biomaterials.

Table of Contents

CHAPTER 1

Substrate-guided Cell Phenotype

Abstract

Mechanotransduction is a ubiquitous cellular process that spans time and length scales. This chapter explores several key aspects of mechanotransduction that are addressed in later chapters, namely nanoscale mechanosensing mechanisms, the downstream cellular programs affected by substrate mechanics, and how mechanotransduction could be relevant in clinical settings. Finally, this chapter introduces big-picture questions in the field that later chapters seek to address. By better understanding mechanotransduction, we can better understand its misregulation in disease as well as design strategies to leverage it using therapeutic biomaterials or even drugs.

Introduction

The ability of cells to interact mechanically with their surroundings seems implicit when looking at large-scale organisms, which are clearly mechanical beings. However, only through recent advances in cell and molecular biology methods have researchers been able to identify mechanisms of this interaction. Cells manage and remodel the extracellular matrix (ECM)[1-5], are responsive to properties of the ECM[6-8], and respond to applied forces and strains[1-5, 9, 10].

Clinical practices such as loading recovering soft tissues to improve healing signal[11, 12] that there is a translation of cell-scale mechanosensing events to tissue-level outputs. Thus the cell can be viewed as a signal processing unit, taking in signals from its mechanical environment, processing those inputs to act accordingly, and managing the feedback between these inputs and outputs (Fig. 1).

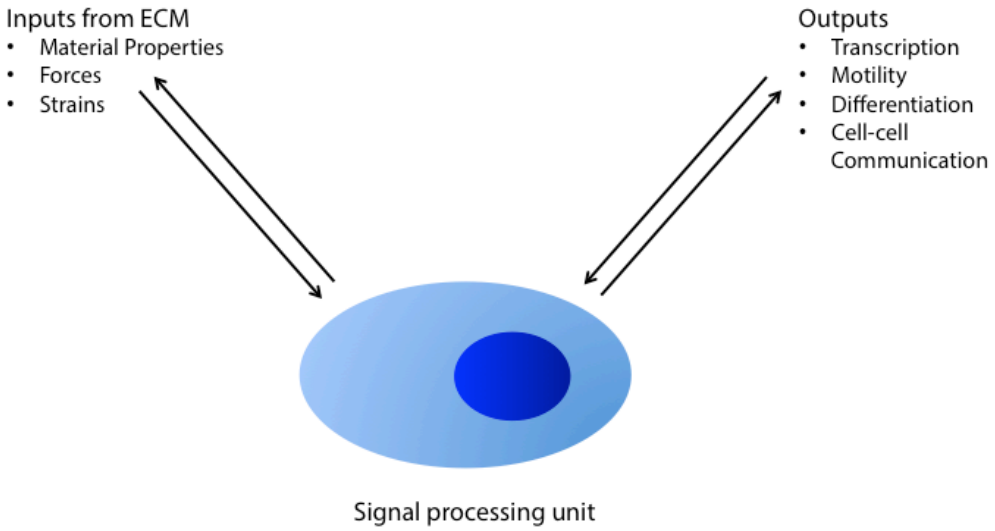

Figure 1: The cell as a mechanical signal processing unit

While initial studies of mechanotransduction used reconstituted ECM as the cell substrate, biomaterials have become an attractive alternative for these studies, since they are highly controllable[13-18]. Interestingly, many of the materials used to study mechanotransduction *in vitro* have the potential to be used therapeutically as scaffolds or cell carriers[13-18]. Furthering the understanding of mechanotransduction in conjunction with improving biomaterials design offers a path towards engineering better therapies[8, 14, 19, 20]. Moreover, the emerging importance of mechanics as morphogenetic cues[21] combined with the field's relative immaturity suggest that it will become increasingly important in the contexts of understanding disease as well as in designing regenerative therapies.

This chapter surveys aspects of mechanotransduction pertaining to each of the three sections in Figure 1, focusing on the nanoscale mechanisms of substrate sensing, moving up in scale to the integration of these signals, and finally moving to the tissue-level implications of mechanotransduction in clinical settings. It finally highlights key limitations in the field's knowledge that subsequent chapters address.

Cells sense substrate properties via integrin-based contacts

Although other mechanisms for stress and strain sensing exist, such as strain-dependent caveoli or mechanically-induced ion channels, cells primarily sense their substrates through their attachment points[6]. The main cell adhesion molecules are called integrins and these bind to specific motifs on ECM proteins[6]. Integrins are transmembrane proteins consisting of α and β subunits. These

subunits are not universally interchangeable and the specific combination of subunits determines the ECM ligand to be recognized. Integrins are linked to the force-generating actin cytoskeleton via a number of adapter proteins that assemble hierarchically. The core set of proteins that can bind both the cytoplasmic domains of β integrins and actin include talin, α-actinin, and filamin. If the adhesion is sufficiently long-lived, additional proteins such as vinculin and paxilin can be recruited, likely by the force-induced exposure of binding sites on talin[6, 22, 23]. This process is called adhesion strengthening and can also occur in the integrin-ECM bond, where a conformational change in the integrins is thought to increase bond strength when the bond is stressed. This arrangement is also known as a catch bond[4, 6, 9]. Conversely, slip bonds, where the bond strength decreases as a function of force application or strain, are found at the actin-talin interface. It is critical to note that this force can be externally applied or cell generated, in which case actomyosin tension generates the force, which is subsequently resisted to varying degrees by the ECM[4, 6, 9].

These bond types are important to understanding the prevailing view of substrate stiffness sensing, which invovles a molecular clutch mechanism[6]. The molecular clutch consists of ECM bound to actin via integrins and associated adapters. Actin exhibits a characteristic rearward flow in the cell called treadmilling in which the F-actin rearward flow is exercised by myosin molecular motors while actin monomers polymerize on the F-actin leading edge and depolymerize on its trailing edge. When force is applied to the clutch, all intermediate bonds are stressed. As mentioned above, the talin-actin bond is a slip

bond. When an adhesion is established, actin rearward flow will stretch this bond relative to the ECM attachment point for that particular linkage. Force will continue to be transmitted until the threshold bond strain is reached, after which the talin-actin bond will rupture. Talin will then randomly bind actin again after some characteristic interval. Bond strengthening and recruitment of additional scaffolding proteins will occur if force persists and the clutch remains intact for longer than the dissociation time-scales of the other scaffolding proteins in the absence of applied force[22, 23].

Many individual clutches bind a single F-actin, meaning that if any of the linkages break, there are still many other linkages retarding the flow. Hence, the average number of intact linkages at any time determines the retardation of actin flow. It is worth noting that the consequence of having more intact linkages is not only the slowing of actin flow, but also the increased linkage lifetime, which in turn increases the duration of downstream signaling initiated at the linkage[22, 23].

Collections of integrins can form a variety of structures, notably focal adhesions and focal complexes. Focal adhesions are clusters of integrins that assemble and strengthen under bundles of actin. They typically only form under large force application or in situations where the substrate stiffness and thus cytoskeletal tension is high. Focal complexes are found in filopodia and lamellapodia and are smaller than focal adhesions. Given their presence in transient cellular structures, they feature rapid disassembly associated with their smaller size[6, 22, 23].

Mechanotransduction affects cell phenotype

There are a number of mechanisms that translate mechanical signals into phenotypic changes in the cell, which can be categorized into direct mechanical effects and indirect signaling effects.

The focal adhesions and contacts mentioned above can be the nexus of signaling. Notably, FAK and Src can quickly be recruited to adhesion sites and initiate downstream signaling[22-24]. These downstream effects have been shown to involve a number of signaling pathways, including MAPK, TGF-β, and BMP/SMAD. As an example of the power of substrate-based signaling, cells from certain lineages lacking ECM adhesions and thus pro-survival MAPK signaling will undergo a special form of apoptosis known as anoikis[25]. Other processes tied into these pathways include cell cycle progression, and the feedback into the regulation of the cytoskeleton, adhesions, and ECM synthesis itself. For example, proteins such as RhoA, Cdc42, and Rac1 are involved in regulating the assembly of focal adhesions and contacts yet themselves are regulated by mechanical signals[6, 24].

A consequence of this feedback is that cell spreading, shape, and motility can be heavily influenced by mechanical signaling[6, 10, 24, 26]. For instance, the Chen lab has published that cytoskeletal stress can be modulated by confining the cell to different areas via micropatterned islands[10, 11]. A huge body of working involving culturing cells on ECM-coated purely elastic polyacrylamide and PDMS gels has established the relationship that cell spreading scales with substrate stiffness, although the universality of this view has been challenged as at

least partly an artifact of the purely elastic nature of these materials[27-29]. This point is address in detail in Chapters 2 and 3.

A landmark paper by the Discher lab showed that mesenchymal stem cell (MSC) differentiation could be controlled by substrate stiffness[30], building off of the Chen lab's work showing that differentiation could be modulated by a cell confinement. This work has implications not only for understanding morphogenesis and how mechanical cues could guide cell fate, but also for regenerative medicine and tissue engineering, wherein a cell's microenvironment could be tuned to optimize regeneration. That work has since been extended to other stem cell types, including pluripotent stem cells[31, 32].

Recent evidence suggests that substrate mechanics induce epigenetic changes in the cell. Work from Song Li's lab has shown differential histone expression as a function of substrate nanotopography[7], while other work has shown differences in iPS conversion mediated by substrate mechanics[33]. Chapter 4 addresses some of these factors in more detail and provides additional evidence for these effects.

The second class of mechanosensing mechanisms is direct in nature, involving direct mechanical linkages between loci of force generation and loci of signaling or transcriptional regulation. One important set of mechanisms is the stress-activated ion channel, which regulates ion flux via membrane stress[22]. Another, which is receiving increased interest, is the direct coupling of the ECM to the nucleus. Cytoskeletal proteins are linked to the nuclear envelope via the LINC complex, which consists of proteins such as SUNs and Nesprins[34]. Along

with lamins, the main class of inner nuclear membrane proteins, these proteins provide an important link between ECM mechanics and the nucleus. Lamins can bind and affect the activation of transcription factors, and since the Discher lab showed that Lamin A expression scales with substrate stiffness[35], there exists a direct mechanism for nuclear transcriptional regulation. In addition, certain segments of DNA known as Matrix Attachment Regions bind to the nuclear envelope, potentially exposing or hiding large numbers of genes[34]. The modulation of force propagation through these linkages would potentially affect this direct chromatin manipulation as well.

Cells sense different aspects of their material microenvironment

The phenotypic outputs affected by mechanotransduction serve as the basis for assays that evaluate the effects of various material parameters on cells. Cell spreading, motility, and MSC differentiation are the most common outputs for these studies and have identified material stiffness[30], nonlinear elasticity[36], stress relaxation[29], nanotopography[37], adhesion ligand composition and density[38], degradability[39, 40], and geometry[41], among others, as driving differences in these outputs. Discrepancies in the data, however, do exist. For instance, it has become clear that culturing cells in 2D versus 3D is significantly different. Chen and Burdick showed that in covalently-crosslinked hydrogels with degradable crosslinks, degradation was necessary to induce MSC osteogenic differentiation[40], even on stiff substrates, which was hypothesized to have to do with the ability of the cells to spread, similar to 2D culture. However, our group had previously

shown that even non-spread MSCs could be driven down an osteogenic lineage in stiff, calcium-crosslinked alginate gels[5]. The reconciliation, however, is that the reversible calcium crosslinks in the alginate gel allow for local rearrangement of adhesion ligands, as evidenced by FRET imaging, and thus the formation of focal adhesions and the buildup of cytoskeletal tension. The covalently-crosslinked gels, however, lacked this feature, requiring bulk degradation of the material to allow the cell to access sufficient numbers of adhesive ligands in order to build sufficient tension. Again, it is this tension that allows the persistent adhesions from which downstream signaling, and thus differentiation, occurs.

Mechanotransduction in clinical settings

Mechanotransduction is important in a number of clinical settings, motivating its study. Briefly, it is involved in atherosclerosis, the healing of orthopedic injuries, cancer progression, and wound healing, among others, and is likely to be involved in other diseases such as Alzheimer's disease which involves plaque formation or diseases of nerve demyelination[42].

Mechanotransduction also represents a key process to be tuned by biomaterials. While many studies have examined the effects of substrate properties *in vitro*, few have translated these phenomena to *in vivo* settings in order to aid regeneration. One study from our group showed that bone healing could be improved by optimizing the stiffness of a transplanted alginate scaffold encapsulating MSCs[43]. Chapter 3 is an extension of this idea examining the effects of stress relaxation on bone regeneration.

Broadening the horizons for mechanotransduction

As mentioned above, the studies showing phenotypic changes in cells in response to substrate mechanics generated the list of outputs to be used in evaluating the importance of various material properties to the cell. However, it is entirely possible that while these outputs are important, their selection by primarily historical means to determine the key material parameters influencing cells has biased the results of the field. Perhaps if different phenomena had been discovered earlier, the field would have been led down a different path. Thus, a global view of mechanotransduction would more thoroughly identify the key outputs and affected processes.

It is not only the experimental outputs that could contribute to a limited understanding of mechanotransduction, but also the experimental setups themselves. For instance, it is widely acknowledged that the different geometric boundary conditions and ECM attachment character of mechanotransduction studies using 2D cell culture contributes to different behavior than in 3D culture[5]. The 3D culture systems, however, are also not without biases. Synthetic polymer matrices might present adhesion molecules in different configurations than fibrular matrices[44]. Moreover, even if stiffness is examined using a controlled system, other material properties such as viscoelasticity and nonlinear elasticity are rarely characterized. It is likely that these material properties not only individually impact cells, but also do so through their interaction.

The above descriptions of mechanosensing mechanisms highlight the high level of detail of the understanding of adhesions themselves and the associated

phenotypic outputs, but the intermediate signaling is far less understood. Attempts to find a universal "mechanostat" which could be downstream of all mechanotransduction processes have not been fruitful. Even important transcription factors such as the Hippo pathway effector YAP, whose activation corresponds to cytoskeletal tension a large fraction of the time[45], does not track with phenotypic outputs completely[45, 46]. Thus the question remains whether there is even one key pathway or signaling funnel for mechanotransduction or whether mechanotransduction is a network process that is biased in one direction or another based on substrate mechanics.

Advances in mechanotransduction have led to a complex view of its effects and mechanisms, but many questions remain. In order to fully exploit this important cellular process, the field would benefit from a more comprehensive view from which to distill key principles, both on the side of the material and on the side of the cell. In this way, by knowing the key material parameters to tune to impact various cellular processes, the biomaterials engineer would have an unprecedented level of control over their designs. By trying to answer the questions outlined above, both the key material properties and key cellular outputs involved in mechanotransduction could possibly be deduced. The subsequent chapters aim to address these questions, with Chapters 2 and 3 focusing on extending the understanding of substrate properties on cells by studying stress relaxation, both in mechanism and application. Chapter 4 provides a global view of mechanotransduction, mapping the networks involved and interactions among different material parameters. Finally, Chapter 5 acknowledges this increase in

biomaterials complexity, and proposes a new biomaterials design methodology through which engineers can maximize biomaterial functionality by leveraging advances in systems biology and experimental design.

References

1. Katz, B.-Z. et al. Physical State of the Extracellular Matrix Regulates the Structure and Molecular Composition of Cell-Matrix Adhesions. *Molecular Biology of the Cell* **11**, 1047-1060 (2000).
2. Dalby, M.J., Gadegaard, N. & Oreffo, R.O.C. Harnessing nanotopography and integrin-matrix interactions to influence stem cell fate. *Nat Mater* **13**, 558-569 (2014).
3. Huang, C.H., Chen, M.H., Young, T.H., Jeng, J.H. & Chen, Y.J. Interactive effects of mechanical stretching and extracellular matrix proteins on initiating osteogenic differentiation of human mesenchymal stem cells. *J Cell Biochem* **108** (2009).
4. Cukierman, E., Pankov, R., Stevens, D.R. & Yamada, K.M. Taking cell-matrix adhesions to the third dimension. *Science* **294** (2001).
5. Huebsch, N. et al. Harnessing traction-mediated manipulation of the cell/matrix interface to control stem-cell fate. *Nat Mater* **9**, 518-526 (2010).
6. Schwartz, M.A. & Simone, D.W. Cell Adhesion Receptors in Mechanotransduction. *Current opinion in cell biology* **20**, 551-556 (2008).
7. Downing, T.L. et al. Biophysical regulation of epigenetic state and cell reprogramming. *Nat Mater* **12**, 1154-1162 (2013).
8. Mammoto, A., Mammoto, T. & Ingber, D.E. Mechanosensitive mechanisms in transcriptional regulation. *Journal of Cell Science* **125**, 3061 (2012).
9. Balaban, N.Q. et al. Force and focal adhesion assembly: a close relationship studied using elastic micropatterned substrates. *Nat Cell Biol* **3** (2001).
10. Bellas, E. & Chen, C.S. Forms, forces, and stem cell fate. *Current Opinion in Cell Biology* **31**, 92-97 (2014).
11. Schindeler, A., McDonald, M.M., Bokko, P. & Little, D.G. Bone remodeling during fracture repair: The cellular picture. *Seminars in Cell & Developmental Biology* **19**, 459-466 (2008).
12. Schultz, G.S. & Wysocki, A. Interactions between extracellular matrix and growth factors in wound healing. *Wound Repair and Regeneration* **17**, 153-162 (2009).
13. Huebsch, N. & Mooney, D.J. Inspiration and application in the evolution of biomaterials. *Nature* **462**, 426-432 (2009).
14. Hench, L.L. & Thompson, I. Twenty-first century challenges for biomaterials. *Journal of The Royal Society Interface* **7**, S379 (2010).
15. Gu, L. & Mooney, D.J. Biomaterials and emerging anticancer therapeutics: engineering the microenvironment. *Nat Rev Cancer* **16**, 56-66 (2016).
16. O'Neill, H.S. et al. Biomaterial-Enhanced Cell and Drug Delivery: Lessons Learned in the Cardiac Field and Future Perspectives. *Advanced Materials* **28**, 5648-5661 (2016).

17. Lee, K.Y. & Mooney, D.J. Alginate: properties and biomedical applications. *Progress in polymer science* **37**, 106-126 (2012).
18. Alsberg, E., Anderson, K.W., Albeiruti, A., Franceschi, R.T. & Mooney, D.J. Cell-interactive Alginate Hydrogels for Bone Tissue Engineering. *Journal of Dental Research* **80**, 2025-2029 (2001).
19. Prestwich, G.D. et al. What Is the Greatest Regulatory Challenge in the Translation of Biomaterials to the Clinic? *Science Translational Medicine* **4**, 160cm114 (2012).
20. Ratcliffe, A. Difficulties in the translation of functionalized biomaterials into regenerative medicine clinical products. *Biomaterials* **32**, 4215-4217 (2011).
21. Janmey, P.A., Wells, R.G., Assoian, R.K. & McCulloch, C.A. From tissue mechanics to transcription factors. *Differentiation; research in biological diversity* **86**, 112-120 (2013).
22. Hoffman, B.D., Grashoff, C. & Schwartz, M.A. Dynamic molecular processes mediate cellular mechanotransduction. *Nature* **475**, 316-323 (2011).
23. Schwartz, M.A. Integrins and Extracellular Matrix in Mechanotransduction. *Cold Spring Harbor Perspectives in Biology* **2**, a005066 (2010).
24. Schwartz, M.A. & Ginsberg, M.H. Networks and crosstalk: integrin signalling spreads. *Nat Cell Biol* **4**, E65-E68 (2002).
25. Frisch, S.M. & Ruoslahti, E. Integrins and anoikis. *Current Opinion in Cell Biology* **9**, 701-706 (1997).
26. Ruiz, S.A. & Chen, C.S. Emergence of patterned stem cell differentiation within multicellular structures. *Stem Cells* **26** (2008).
27. Pelham, R.J. & Wang, Y. Cell locomotion and focal adhesions are regulated by substrate flexibility. *Proc Natl Acad Sci U S A* **94** (1997).
28. Cameron, A.R., Frith, J.E. & Cooper-White, J.J. The influence of substrate creep on mesenchymal stem cell behaviour and phenotype. *Biomaterials* **32**, 5979-5993 (2011).
29. Chaudhuri, O. et al. Substrate stress relaxation regulates cell spreading. *Nat Commun* **6** (2015).
30. Engler, A.J., Sen, S., Sweeney, H.L. & Discher, D.E. Matrix elasticity directs stem cell lineage specification. *Cell* **126** (2006).
31. Sun, Y. et al. Mechanics regulates fate decisions of human embryonic stem cells. *PLoS One* **7** (2012).
32. Evans, N.D. et al. Substrate stiffness affects early differentiation events in embryonic stem cells. *Eur Cells Mater* **18** (2009).
33. Caiazzo, M. et al. Defined three-dimensional microenvironments boost induction of pluripotency. *Nat Mater* **15**, 344-352 (2016).
34. Wang, N., Tytell, J.D. & Ingber, D.E. Mechanotransduction at a distance: mechanically coupling the extracellular matrix with the nucleus. *Nat Rev Mol Cell Biol* **10**, 75-82 (2009).

35. Swift, J. et al. Nuclear Lamin-A Scales with Tissue Stiffness and Enhances Matrix-Directed Differentiation. *Science (New York, N.Y.)* **341**, 1240104-1240104 (2013).
36. Hall, M.S. et al. Fibrous nonlinear elasticity enables positive mechanical feedback between cells and ECMs. *Proceedings of the National Academy of Sciences* (2016).
37. Park, S. & Im, G.-I. Stem cell responses to nanotopography. *Journal of Biomedical Materials Research Part A* **103**, 1238-1245 (2015).
38. Engler, A. et al. Substrate compliance versus ligand density in cell on gel responses. *Biophys J* **86** (2004).
39. McKinnon, D.D., Domaille, D.W., Cha, J.N. & Anseth, K.S. Biophysically Defined and Cytocompatible Covalently Adaptable Networks as Viscoelastic 3D Cell Culture Systems. *Advanced materials (Deerfield Beach, Fla.)* **26**, 865-872 (2014).
40. Khetan, S. et al. Degradation-mediated cellular traction directs stem cell fate in covalently crosslinked three-dimensional hydrogels. *Nat Mater* **12**, 458-465 (2013).
41. Kolesky, D.B., Homan, K.A., Skylar-Scott, M.A. & Lewis, J.A. Three-dimensional bioprinting of thick vascularized tissues. *Proceedings of the National Academy of Sciences of the United States of America* **113**, 3179-3184 (2016).
42. Jaalouk, D.E. & Lammerding, J. Mechanotransduction gone awry. *Nature reviews. Molecular cell biology* **10**, 63-73 (2009).
43. Huebsch, N. et al. Matrix elasticity of void-forming hydrogels controls transplanted-stem-cell-mediated bone formation. *Nat Mater* **advance online publication** (2015).
44. Wen, J.H. et al. Interplay of matrix stiffness and protein tethering in stem cell differentiation. *Nat Mater* **13**, 979-987 (2014).
45. Dupont, S. et al. Role of YAP/TAZ in mechanotransduction. *Nature* **474** (2011).
46. Ovijit Chaudhuri, L.G., Darinka Klumpers, Max Darnell Sidi A. Bencherif, James C. & Weaver, N.H., Hong-pyo Lee, Evi Lippens, Georg N. Duda , David J. Mooney Hydrogels with tunable stress relaxation regulate stem cell fate and activity. *Nat Materials* **Accepted** (2015).

CHAPTER 2

Stochastic Lattice Spring Model of Cell Spreading

Abstract

While many studies have shown the influence of adhesion substrate stiffness on phenotypic outputs such as cell spreading, proliferation, and YAP nuclear localization, the majority of these studies have been conducted on purely elastic materials. Recent evidence, however, illustrates that the viscoelastic properties of the material can also have a dramatic impact, one in which the traditional monotonic scaling of these phenotypic outputs with substrate stiffness is not maintained. We hypothesized that this effect was due to the coupling of adhesion ligand density with the time-dependent mechanical properties of the substrate and proposed a model of cell spreading as a function of substrate mechanics, accounting for adhesion ligand density, stiffness, viscoelasticity, and mechanical connectivity among adhesion sites. This lattice spring model was capable of recapitulating experimental results in which cell spreading is abrogated on high-stiffness, stress relaxing substrates and enhanced on low-stiffness, stress relaxing substrates relative to purely elastic ones, in a ligand density dependent manner. Moreover, we show that each of these behaviors is a function of whether creep or stress relaxation behavior dominates that specific regime. Overall, these results provide mechanistic insight into the sensing of substrate viscoelasticity and help to guide future materials development by through tuning these properties.

Introduction

The extracellular matrix (ECM) has been shown to influence cells in a multitude of ways[1–5]. The mechanical properties of a cell's adhesion substrate have received significant recent interest since the substrate stiffness has been shown to regulate phenotypic outputs including cell spreading, proliferation, migration, and stem cell differentiation[1–5]. However, many of the substrates used to study the mechanisms of this sensing are purely elastic. Commonly used substrates include polyacrylamide and PDMS that have been coated with ECM proteins such as collagen to facilitate adhesion[6].

While these studies have provided significant insight into substrate sensing, they do not reflect a number of the properties of native ECM. One of the most prominent differences between these substrate models and native ECM is that the fibrous nature of native ECM gives rise to viscoelastic behavior, meaning that the stress in the material will relax over time at a constant strain[7-11]. Given that cells are so sensitive to the elasticity of the matrix, our group hypothesized that viscoelasticity and this stress-relaxing quality, which in a sense modulates the instantaneous elasticity of a material, could be similarly sensed by the cells.

In order to address these questions, previous members of our group employed alginate hydrogels that could be either covalently or ionically crosslinked, yielding either elastic, or viscoelastic behavior, respectively[12]. In addition, the crosslink density could be varied to impact the stiffness of the gels, and the density of RGD adhesion ligands could be varied to alter the number of sites on the substrate available for the cells to engage. The canonical view of cell

spreading and proliferation was that these both increased with stiffness[1-5]. However, by plating cells on these gels, it was shown that the stress-relaxing substrates decreased cell spreading relative to purely elastic ones at high stiffness, and that, if the adhesion ligand density was high, viscoelasticity actually rescued cell spreading and proliferation on soft substrates[13].

Since these experimental results suggested that the response of cells to stress relaxation was not monotonic and was ligand density-dependent, we sought to develop a computational model of this process to address the hypothesis that the response to stress relaxation could be captured by solely accounting for material-side effects without including additional sophistication in the cell-side substrate-sensing machinery. Thus, we hypothesized that the cell's integrin-based adhesions could be manipulated by the stress relaxation and ligand density of the substrate into producing a mechanical response equivalent to that on very different, but elastic substrates.

In order to formulate a model that would satisfy these criteria, we adopted the basic architecture of a model of cell spreading by Chan and Odde[14,15]. This model captures the basic coarse-grained cell-side machinery needed to ask the question of whether the material viscoelasticity and adhesion ligand density are sufficient to manipulate the core sensing machinery of the cell and induce spreading. However, the previously published model lacks the ability to specify adhesion ligand density, incorporate more rich material mechanics, and to capture the mechanical coupling between adhesion sites.

The model presented here extends the Chan and Odde model by including a lattice-spring representation of a material which gives fine-tuned control over substrate properties and allows adhesion sites to interact mechanically. Moreover, this representation offers a facile scheme for the incorporation of ligand density into the model.

By simulating a range of viscoelastic materials in this manner, we show that we can not only recapitulate the observed experimental spreading results, but can mechanistically generate hypotheses for the observed effects in each of the mechanical regimes in which behavior on viscoelastic substrates deviates from that on purely elastic ones.

Results and Discussion

We modified the cell spreading model of Chan and Odde by incorporating additional material-side complexity in order to simulate the early effects of substrate viscoelasticity on cell spreading. In this model, actin polymerization at a speed that exceeds that of actin retrograde flow drives spreading. Actin is tethered to the substrate by force-dependent adhesions (slip bonds) that retard retrograde flow, yielding faster spreading. The stiffer the substrate, the faster the disengagement of the slip bonds and the shorter the distortion of the bonds, which restricts the degree of retrograde flow, resulting in more spreading.

To allow for the capture of additional material complexity, the material was represented as a lattice spring network where the connections between mass-bearing nodes can be represented by any spring/damper model of a material (Fig.

2A). This representation has a number of advantages. First, the node representation allows for the easy incorporation of adhesion ligand density by controlling the nodes to which the cell can adhere. Secondly, the modularity of the material models used between nodes allows purely elastic materials to be compared to different viscoelastic ones. Thirdly, the connectivity among adhesions allows for strain fields to propagate through a material, capturing coupling among nodes.

Formulating the model for comparison to the experimental results, we represented the material either by simple springs, representing an elastic material, or by a four-element Burger's model, which allows for tuning the full spectrum of viscoelastic behavior, from creep-dominated Voigt behavior to stress-relaxation-dominated Maxwell behavior.

We first tested the spreading behavior on a purely elastic representation. Consistent with the Chan and Odde model and our experimental results, we found that spreading increased with the stiffness of the substrate (Fig. 2B). If we varied the adhesion ligand density, we found that higher adhesion ligand densities allowed the cell to spread on softer substrates than they otherwise would.

Next, we searched for model parameters that would recapitulate the experimental result that viscoelasticity abrogates cell spreading as long as the adhesion ligand density is low, but enhances it if the substrate is soft and the adhesion ligand density is high. We were able to fine such a parameter set, reproducing the observed behavior (Fig. 2C). Fig. 2D depicts the differences between the viscoelastic and elastic conditions with these parameters, confirming

that spreading is enhanced on soft substrates and reduced on stiff substrates in a ligand density dependent manner as a function of stress relaxation.

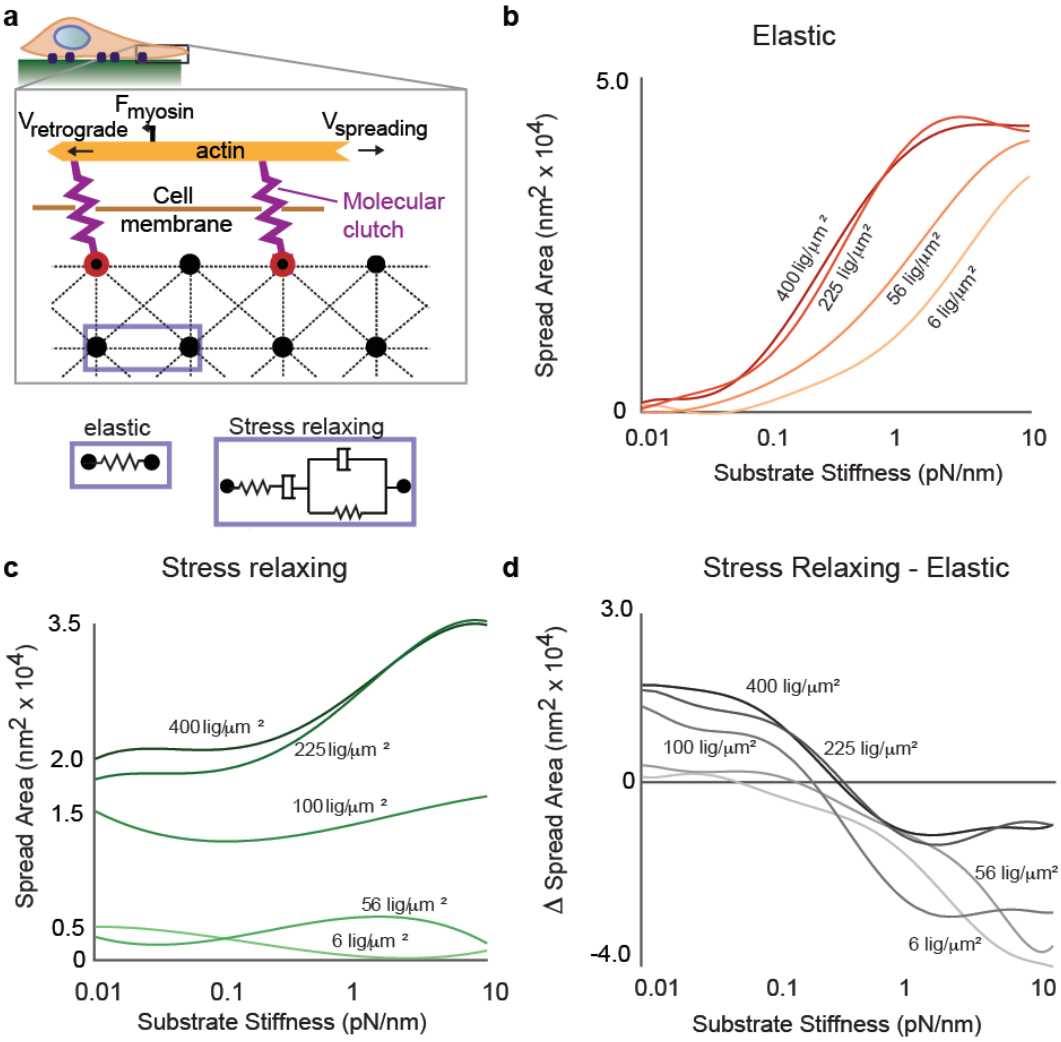

Figure 2: Stochastic lattice spring model predicts increased cell spreading at low initial stiffness on viscoelastic substrates that exhibit stress relaxation relative to elastic substrates. A) Schematic depicting model of cell spreading on elastic or viscoelastic substrates. Actin polymerization at the leading edge of the cell is coupled to the substrate through molecular clutches, and these clutches inhibit retrograde flow of the actin driven by myosin motors. The substrate is modeled as an array of nodes connected by either Hookean springs, representing an elastic substrate, or Burgers model elements, representing a viscoelastic substrate exhibiting stress relaxation. B) Simulation results for cell spreading area on elastic substrates as a function of initial substrate stiffness and adhesion ligand density. C) Simulation results for cell spreading area on substrates with stress relaxation as a function of initial substrate stiffness and adhesion ligand density. Voigt damping coefficient, h_1, was $5x10^{-13}$, and Maxwell damping coefficient, h_2, was $1x10^{-13}$ for this set of simulations. D) Difference in cell spreading area for cells on substrates

with stress relaxation relative to elastic substrates. Greater spreading on substrates with stress relaxation is observed for all conditions at low substrate stiffness.

In order to gain further mechanistic insight, we examined the nature of the Burger's model parameter values that captured this behavior. We tuned the model to the Maxwell or Voigt limits, two common representations of viscoelasticity, in order to observe which representation gave rise to which experimentally observed behavior. We first observed the spreading-stiffness relationships for the Maxwell and Voigt limits by varying ligand density (Fig. 3A-D). We found that the Voigt limit captures the increase in spreading on soft substrates with high ligand density while the Maxwell limit captures the reduction in spreading on all stiff substrates. Next, by tuning the damping coefficients for each of those models at high ligand density, we see that the degree of spreading rescue or abrogation is mediated by those coefficients, suggesting that it is specifically the viscoelastic components that give rise to these two different regimes (Fig. 3E,F).

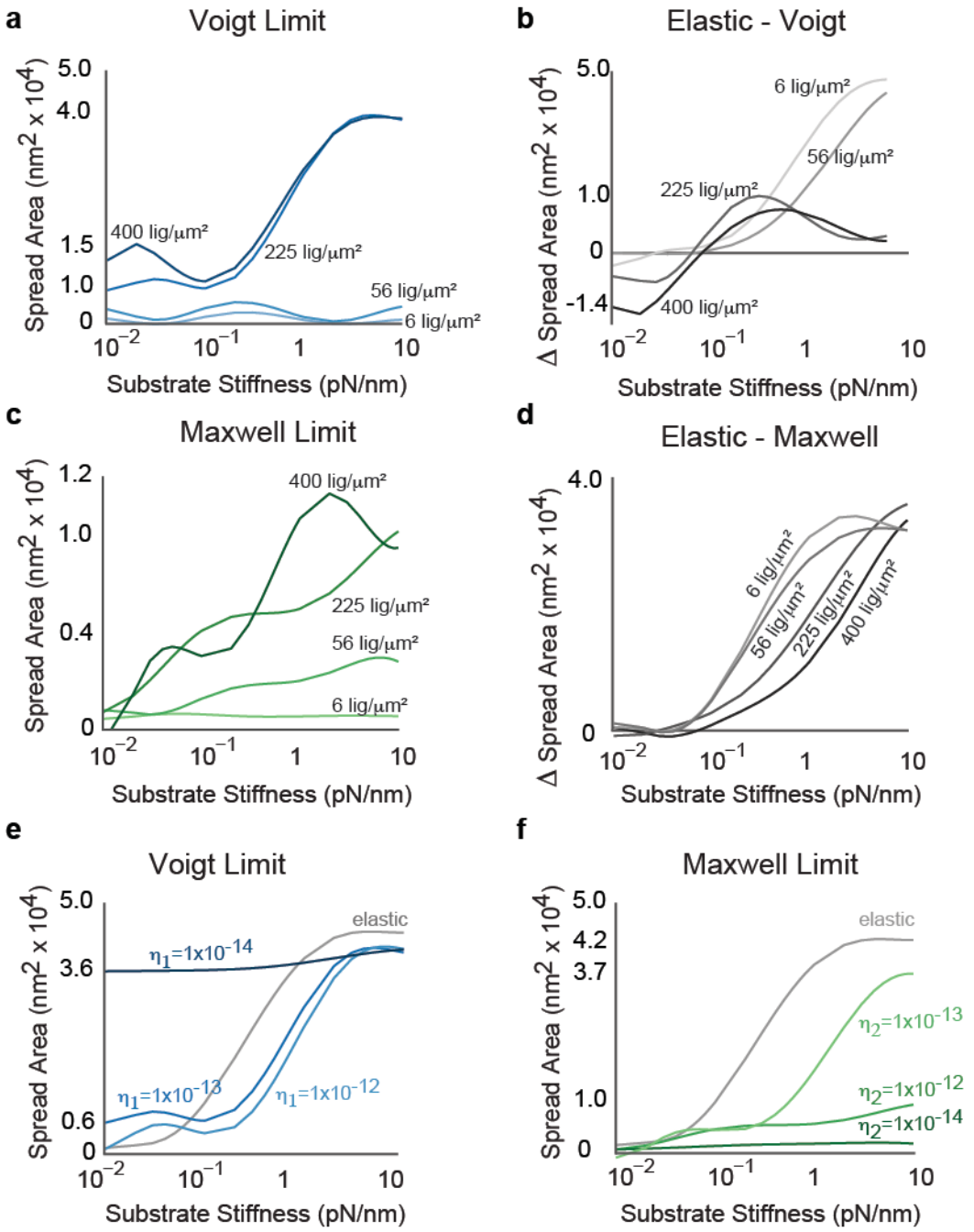

Figure 3: Supplemental model characterization. A,C) Stiffness-spreading relationship for different ligand densities in the Voigt and Maxwell limits of the Burger's Model. B,D) Differences in spreading between the elastic and Voigt or Maxwell limits of the Burger's Model. E,F) Stiffness-spreading relationship at high ligand densities for different damping coefficients for the Voigt or Maxwell limits of the Burger's Model.

To further examine the means by which the simulations predict these discrepancies between elastic and viscoelastic substrates, we observed the dynamics of node spacing throughout the simulations (Fig. 4A). Since cells have been shown to deform the matrix as a function of substrate stiffness, we thought that the node spacing could act as a proxy for material remodeling and give insight into the sensing mechanism. Strikingly, we found that the degree of creep in the material, as dictated by the Voigt damping coefficient, modulated the spacing of the nodes in front of the leading edge of the simulated cell (Fig. 4B). This decrease in internode spacing represents an increase in the effective local adhesion ligand density of the material (Fig. 4A). For materials with low initial adhesion ligand density, this increase in effective density is modest, but for materials with a high adhesion ligand density, this incremental increase represents a large increase in the percentage increase in density. For example, if the creep leads to an average leading edge internode spacing decrease of 10 nm, but the initial spacing was 100 nm, this effect results in a 10% increase in density. If, however, the initial spacing is 40 nm, this same 10 nm effect results in a 25% increase in density. As the previous simulations showed that for a constant stiffness, adhesion ligand density dramatically impacts a cell's ability to spread, our mechanistic study of the internode spacing yielded a plausible mechanism for the coupling of adhesion ligand density to viscoelasticity. Intriguingly, these results are consistent with the experimental observation that cell spreading is correlated with clustering of adhered integrins. The decreased internode spacing demonstrated here is consistent with the notion of enhanced clustering.

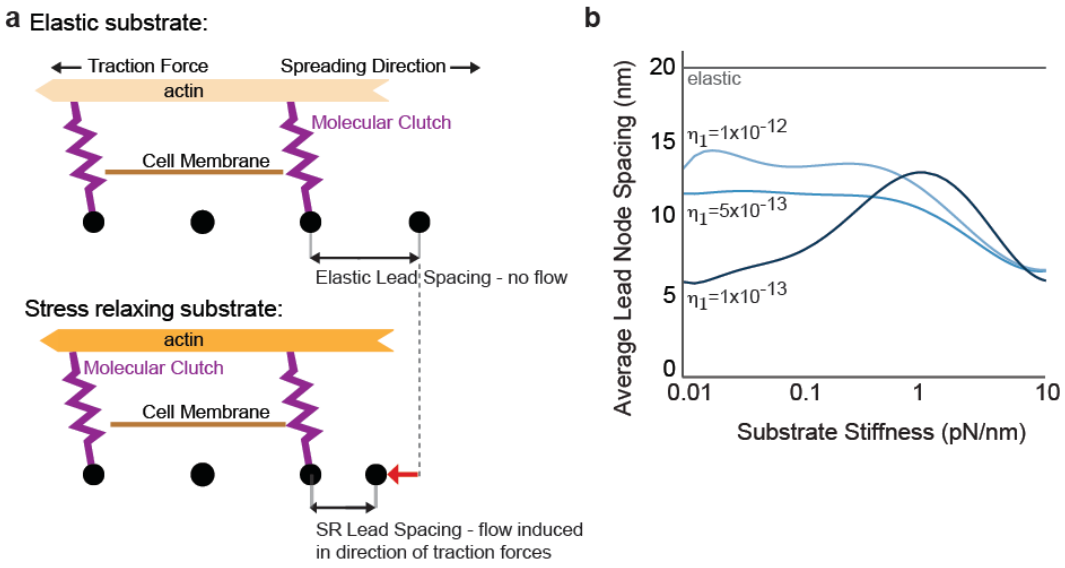

Figure 4: Simulations predict that cell spreading on stress relaxing substrates is associated with flow and plastic deformation of the adhesion substrate. (a) Cartoon of cell spreading on elastic substrate or substrate with stress relaxation. (b) Simulation results for lead node spacing as a function of substrate stiffness for elastic substrates, and stress relaxing substrates with the indicated Burger's model Maxwell damping coefficient (h_1).

Conclusions

In this chapter, a computational model was formulated to address the mechanism of differential spreading on viscoelastic versus elastic substrates. By extending an existing model of cell spreading to include a sophisticated representation of the adhesive substrate, we were able to recreate observed experimental behaviors. Moreover, we showed that the observed increase in spreading on soft viscoelastic substrates of high ligand density is linked to the creep behavior of the material and the resulting changes in local adhesion ligand density. Abrogation of spreading on other viscoelastic substrates was explained through the stress-relaxation of the material. These results suggest that the effects of viscoelasticity on cell substrate sensing can be explained by the temporal and adhesion density-dependent behavior of the substrate without accounting for

additional complexity of the cellular sensing mechanisms. We hope that this mechanistic understanding can be used to design new biomaterials to influence cell fate in therapeutic ways.

Materials and Methods

Model Assumptions

This model builds upon the framework outlined by Chan and Odde[14,15], by incorporating a variety of substrate behaviors as well as adhesion ligand density into a dynamic simulation of cell spreading. The goal of these simulations is to, even with a simple treatment of spreading mechanics, observe stark differences in cell mechanosensing as a function of material-side parameters. The use of a physical output such as cell spreading that, in some cases, correlates with other cell behaviors removes complications concerning intracellular signaling. To that end, the model assumes no feedback into the number or applied force of myosin motors and does not distinguish between bundled and filamentous actin. Due to the short timescales over which differences in cell spreading are simulated, the specific composition of linker proteins from the substrate to actin is not specified. Hence the linker proteins are treated as a simple spring and no adhesion-strengthening is considered.

The linkers are assumed, however, to undergo force-dependent dissociation, given by $k_{off}^{*} = k_{off} e^{F_{clutch}/F_{rup}}$, where k_{off}^{*} is the force-dependent off-rate, k_{off} is the unloaded off-rate, F_{clutch} is the retarding force imposed by each clutch, and F_{rup} is the rupture force per bond. In addition, it is

assumed that integrins bind adhesion ligands prior to incorporation into the adhesion complex, allowing for linkage to actin upon the spreading front reaching a new available ligand.

Inhibition of actin retrograde flow velocity is assumed to obey Eq. 1 as a function of the force sustained in the molecular clutches, where v_{spread} is the cell spreading velocity, v_{poly} is the actin leading edge polymerization velocity, $\sum_{clutch} F_{clutch}$ is the sum of retarding forces sustained in all of the adhesion sites, and F_{stall} is the force required to stop actin retrograde flow velocity. The actin polymerization rate is treated as constant and the spreading velocity is thus given by $v_{spread} = v_{poly} - v_{retrograde}$ where $v_{retrograde}$ is the actin retrograde flow velocity.

$$v_{retrograde} = v_{poly}\left(1 - \frac{\sum_{clutch} F_{clutch}}{F_{stall}}\right)$$

The substrates is modeled as a 2D lattice of mass nodes, with each node connected to its neighbors via a simple spring in the purely elastic case, or, in the viscoelastic case, a Burger's model (Fig. 5A, Eq. 2), where σ is the stress sustained in the linkage, ε is the linkage strain, E_1 is the Maxwell element stiffness, E_2 is the Voigt element stiffness, η_1 is the Maxwell element damping coefficient, and $\eta_2$is the Voigt element damping coefficient. Alginate, the material used experimentally in this study, has previously been modeled using a Burger's model[16]. Material parameter ranges were calibrated based on canonical spreading responses to different parameters in the purely elastic case, with the low end for

stiffness being those purely elastic substrates on which cells do not spread and the high end being those on which cells do spread (Table 1).

$$\sigma + \left(\frac{\eta_1}{E_1} + \frac{\eta_1}{E_2} + \frac{\eta_2}{E_2}\right)\frac{d\sigma}{dt} + \left(\frac{\eta_2}{E_2}\right)\frac{d^2\sigma}{dt^2} = \left(\frac{\eta_1^2\eta_2}{E_1E_2}\right)\frac{d\varepsilon}{dt}\frac{d^2\varepsilon}{dt^2}$$

On the top level of nodes, only certain nodes are made available for binding by the cell, as determined by the ligand density. Ligand densities were approximated based on previous approaches to quantify spacing of RGD ligands on alginate hydrogels for varying degrees of substitution that are consistent with those used in this study[17].

Model Implementation

The following algorithm is carried out in MATLAB (Fig. 5B). At each time step (0.2 ms, Fig. 5C), it is determined whether the cell spreading front has passed a new available adhesion ligand on the substrate. If so, a new bond is formed, determined by k_{on} and the number of adhered clutches is incremented. Given the current filament velocity, a strain of $dt * v_{fil}$ is imposed on the substrate via the clutches. Eq. 2 is discretized using a Backward Euler method and the force between each node and its neighbors is calculated based on the new strain. For each node in the lattice, the resultant horizontal and vertical forces are found by summing the horizontal and vertical components of the force between the node and each of its neighbors; the equations of motion are then solved using an implicit Beeman scheme to find the new position of each node in the lattice for that time step.

At this point, based on the new strain profile of the lattice, the new force sustained in each molecular clutch is calculated using the clutch spring constant,

κ_{clutch}, and each molecular clutch is tested for dissociation per the Bell model described above. The new forces sustained in each clutch are used to update the actin retrograde flow velocity for the next time step.

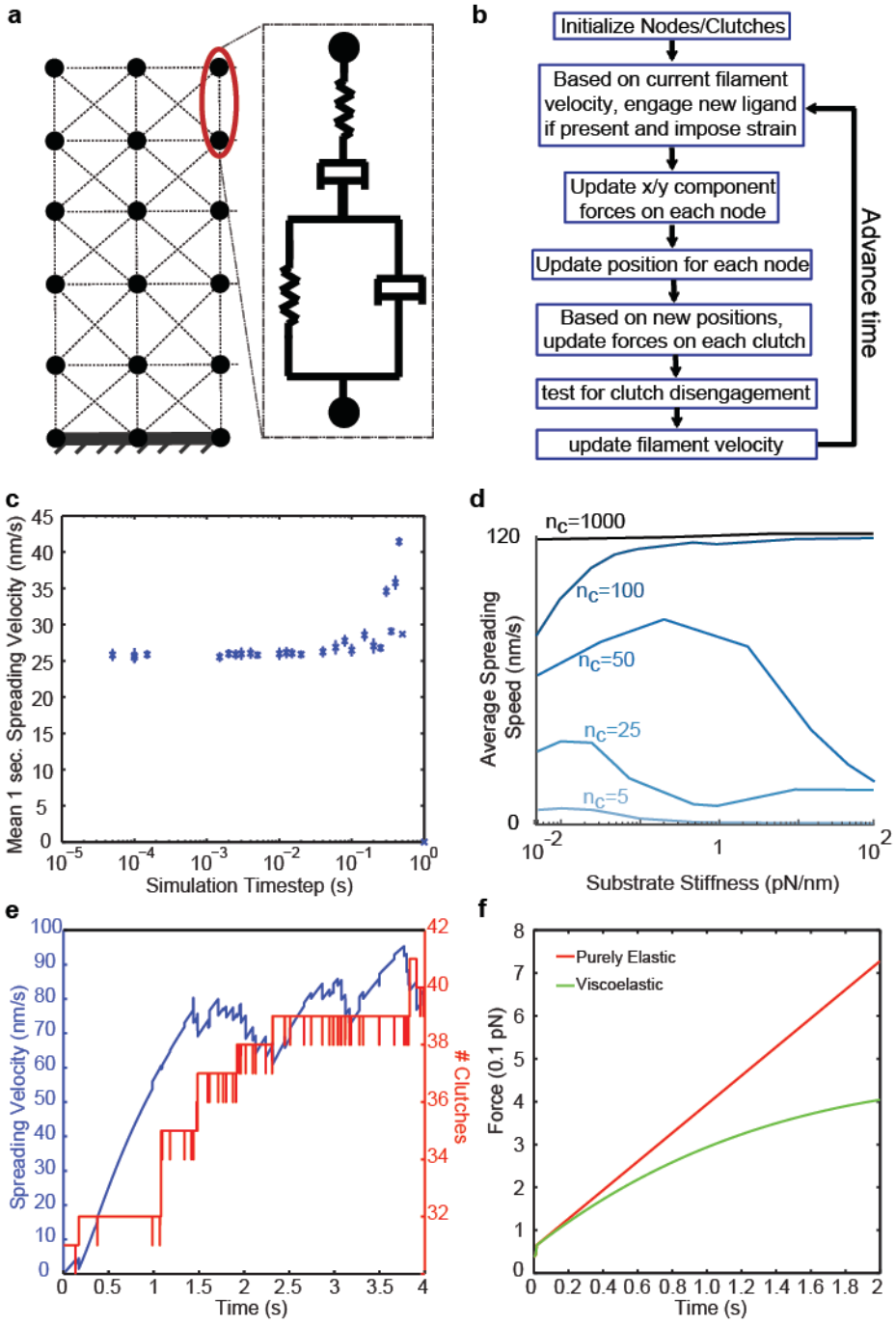

Figure 5: Model formulation. A) Schematic of lattice-spring network used to model the substrate. Simple springs are used as the linkages in a purely elastic

case and the four-element Burger's Model is used in the viscoelastic case. B) Flowchart depicting the simulation algorithm. C) Time-step dependence of algorithm. Simulations were run for 1 sec. in simulation time using various time steps and the resulting average spreading velocities for 20 simulation runs was recorded. Error bars represent S.D. (n=20). D) Average spreading velocity as a function of substrate stiffness if ligand density dependence and substrate lattice are removed. Data is reported as the mean of five simulation runs. E) Spreading velocity (blue) and number of molecular clutches (red) for a representative purely elastic substrate (k=1 pN/nm, 0.02 ligands/nm). Spikes are indicative of bond rupture. F) Example force/extension curves from simulated tensile testing. Substrates were strained at 0.17nm/ms and the resulting force in a given linkage was recorded. A representative purely elastic substrate is given in green and a representative viscoelastic substrate is given in blue, both of the same initial elastic modulus.

Supplemental Model Characterization

By eliminating the ligand density dependence and treating the substrate as a simple spring, the "load and fail" and "frictional slippage" regimes described by Chan and Odde are recreated (Fig. 5D). Upon incorporating the material lattice and ligand density, dissociation events as well as clutch addition due to spreading are noted (Fib. 4E). In order to validate the behavior of the lattice, simulated tensile tests were performed as to confirm purely elastic or viscoelastic behaviors. At a constant strain rate, purely elastic substrates demonstrate a linear force/extension relationship, while viscoelastic substrates demonstrate stress relaxation, confirming the capability of the substrate lattice to capture both purely elastic and viscoelastic behaviors (Fig. 5F).

Associated Publication

Chaudhuri O, Gu L, Darnell M, Klumpers D, Bencherif SA, Weaver JC, et al. Substrate stress relaxation regulates cell spreading. Nat Commun. 2015;6.

References

1. Mammoto, T. & Ingber, D. E. Mechanical control of tissue and organ development. *Dev. Camb. Engl.* **137,** 1407–1420 (2010).
2. DuFort, C. C., Paszek, M. J. & Weaver, V. M. Balancing forces: architectural control of mechanotransduction. *Nat. Rev. Mol. Cell Biol.* **12,** 308–319 (2011).
3. Vogel, V. & Sheetz, M. Local force and geometry sensing regulate cell functions. *Nat. Rev. Mol. Cell Biol.* **7,** 265–275 (2006).
4. Discher, D. E., Janmey, P. & Wang, Y.-L. Tissue cells feel and respond to the stiffness of their substrate. *Science* **310,** 1139–1143 (2005).
5. Wozniak, M. A. & Chen, C. S. Mechanotransduction in development: a growing role for contractility. *Nat. Rev. Mol. Cell Biol.* **10,** 34–43 (2009).
6. Engler, A. *et al.* Substrate compliance versus ligand density in cell on gel responses. *Biophys. J.* **86,** 617–628 (2004).
7. Knapp, D. M. *et al.* Rheology of reconstituted type 1 collagen gel in confined compression. *J. Rheol.* **41,** (1997).
8. Janmey, P. A., Amis, E. J. & Ferry, J. D. Rheology of Fibrin Clots. VI. Stress Relaxation, Creep, and Differential Dynamic Modulus of Fine Clots in Large Shearing Deformations. *J. Rheol.* **27,** (1983).
9. Levental, I., Georges, P. C. & Janmey, P. A. Soft biological materials and their impact on cell function. *Soft Matter* **3,** 299–306 (2007).
10. Liu, Z. & Bilston, L. On the viscoelastic character of liver tissue: experiments and modelling of the linear behaviour. *Biorheology* **37,** 191–201 (2000).
11. Geerligs, M., Peters, G. W. M., Ackermans, P. A. J., Oomens, C. W. J. & Baaijens, F. P. T. Linear viscoelastic behavior of subcutaneous adipose tissue. *Biorheology* **45,** 677–688 (2008).
12. Zhao, X., Huebsch, N., Mooney, D. J. & Suo, Z. Stress-relaxation behavior in gels with ionic and covalent crosslinks. *J. Appl. Phys.* **107,** 63509 (2010).
13. Chaudhuri O, Gu L, Darnell M, Klumpers D, Bencherif SA, Weaver JC, et al. Substrate stress relaxation regulates cell spreading. Nat Commun. 2015;6.
14. Chan, C. E., Odde, D. J. Traction dynamics of filopodia on compliant substrates. Science 322, 1687–91 (2008).
15. Bangasser, B. L., Rosenfeld, S. S. & Odde, D. J. Determinants of maximal force transmission in a motor-clutch model of cell traction in a compliant microenvironment. *Biophys. J.* **105,** 581–592 (2013).
16. Donati, I. et al. New hypothesis on the role of alternating sequences in calcium-alginate gels. Biomacromolecules 6, 1031–40 16.
17. Comisar, W. A., Hsiong, S. X., Kong, H.-J., Mooney, D. J. & Linderman, J. J. Multi-scale modeling to predict ligand presentation within RGD nanopatterned hydrogels. *Biomaterials* **27**, 2322–9 (2006).

CHAPTER 3

Effects of Stress Relaxation on Bone Formation and Scaffold Remodeling *In Vivo*

Abstract

The rate of stress relaxation of adhesion substrates potently regulates cell fate and function in vitro, and here we tested whether it could regulate bone formation *in vivo* by implanting alginate gels with differing rates of stress-relaxation carrying human mesenchymal stem cells into rat calvarial defects. After three months, the rats that received fast-relaxing hydrogels ($t_{1/2} \sim 50s$) showed significantly more new bone growth than those that received slow-relaxing, stiffness-matched hydrogels. Strikingly, substantial bone regeneration resulted from rapidly relaxing hydrogels even in the absence of transplanted cells. Histological analysis revealed that the new bone formed with rapidly relaxing hydrogels was mature and accompanied by extensive matrix remodeling and hydrogel disappearance. This tissue invasion was found to be prominent after just two weeks and the ability of stress relaxation to modulate cell invasion was confirmed with *in vitro* analysis. These results suggest that substrate stress relaxation can mediate scaffold remodeling and thus tissue formation, giving tissue engineers a new parameter for optimizing bone regeneration.

Introduction

Biomaterials have been widely explored to promote tissue regeneration, in part due to their ability to tune the extracellular environment surrounding both transplanted and host cells. Tissue engineers have explored a wide array of cues that can be presented to cells, including but not limited to growth factors, drugs, other cell types, extracellular matrix ligands, and mechanical factors [1-4]. These efforts seek to improve transplanted cell viability, control cell presence both spatially and temporally, and regulate cell fate decisions, all issues that are facilitated with material systems. Despite the broad *in vitro* characterization of the impact of many of these cues on cells, translation of these strategies into the complex *in vivo* milieu has been challenging [5-8].

One set of material cues that has garnered increasing interest is mechanical in nature, involving material properties such as stiffness, porosity, and topography [9, 10]. Since it was first shown that adhesion substrate stiffness can influence mesenchymal stem cell differentiation, that observation has been extended to a variety of cell types and outputs, including stem cells of all germ layers and pluripotent stem cells [2, 11]. Recently, we, among others, demonstrated that one mechanical property that had been previously ill-explored with regards to its effect on cells, the rate of substrate stress relaxation, is a regulator of cell spreading, proliferation, and osteogenic differentiation of encapsulated mesenchymal stem cells *in vitro*, likely due to an increased ability of cells to remodel the extracellular matrix on these substrates relative to purely elastic substrates [12-15].

This manuscript addresses the hypothesis that substrate stress relaxation can regulate bone regeneration *in vivo*. Bone regeneration could be impacted by the ability of stress relaxation to directly impact osteogenesis, or to the ability of cells to readily remodel and invade rapidly relaxing hydrogels. Cell invasion into implants has previously been shown to be necessary for scaffold-based bone regeneration, motivating past work to design degradability and porosity into engineered implants to allow for cell migration [16].To test our hypothesis, human mesenchymal stem cells (hMSCs) were encapsulated in alginate hydrogels with different stress relaxation time-scales and implanted in rat calvarial defects. To examine the intrinsic ability of rapidly relaxing hydrogels to promote bone regeneration, these gels were also placed in defects without hMSCs. Previous studies have demonstrated the ability of substrate stress relaxation to regulate osteogenic differentiation of mouse mesenchymal stem cells *in vitro* [14], but this effect has not been extended to hMSCs or to an *in vivo* setting. Calcium-crosslinked alginate hydrogels were chosen as cell scaffolds, since alginate has been previously shown to allow for the independent control of initial elastic modulus and stress relaxation time [12, 14]. Crosslinking guluronic acid residues on adjacent alginate chains by divalent cations allows for the maintenance of hydrogel microscale architecture independent of crosslinking density and confers viscous damping effects to the hydrogels due to the dynamic nature of the crosslink formation and rupture. Moreover, decreasing the molecular weight of the alginate chains allows for increased chain mobility within the gel mesh and thus a faster relaxation timescale [8, 12, 14]. Alginate hydrogels were fabricated at an

initial stiffness slightly lower than has been reported to be optimal for osteogenic differentiation of MSCs [17] in order to sensitize the cells to the effect of the stress relaxation and ensure that stiffness effects did not dominate the mechanical cues delivered to the cells. The gels were modified with an RGD peptide motif to support cell adhesion but contained no exogenous growth factors or other soluble factors. A recent study featuring similar hydrogels showed that the pore size and RGD distributions between groups were not significantly different [14]. The particular model of bone regeneration was chosen due to its wide use in the field and the possibility of creating a critical-sized defect that does not require external stabilization [18]. After explantation, defects that contained implants with relatively fast stress relaxation times showed markedly more bone formation than defects that contained implants with relatively slow stress relaxation times, as well as extensive matrix remodeling and hydrogel disappearance. Analysis of the early events in this healing process revealed that the fast-relaxing gels are dramatically remodeled within two weeks and *in vitro* studies confirmed that cells are better able to migrate into fast relaxing gels, yielding a new way to control scaffold invasion without the need for engineered chemical degradation or porosity. These results demonstrate that substrate stress relaxation can be a potent parameter for tissue engineers to use to optimize bone regeneration.

Results

We first determined if the native environment of healing bone, the hematoma, would exhibit stress relaxation, to validate the potential physiologic relevance of this parameter for bone regeneration. Human hematomas from adult donors were obtained from the clinic, and subjected to compression testing. These hematomas demonstrated an average relaxation time of ~195 seconds (Fig. 6A), confirming these human tissues demonstrate significant and rapid stress relaxation (Fig. 6A).

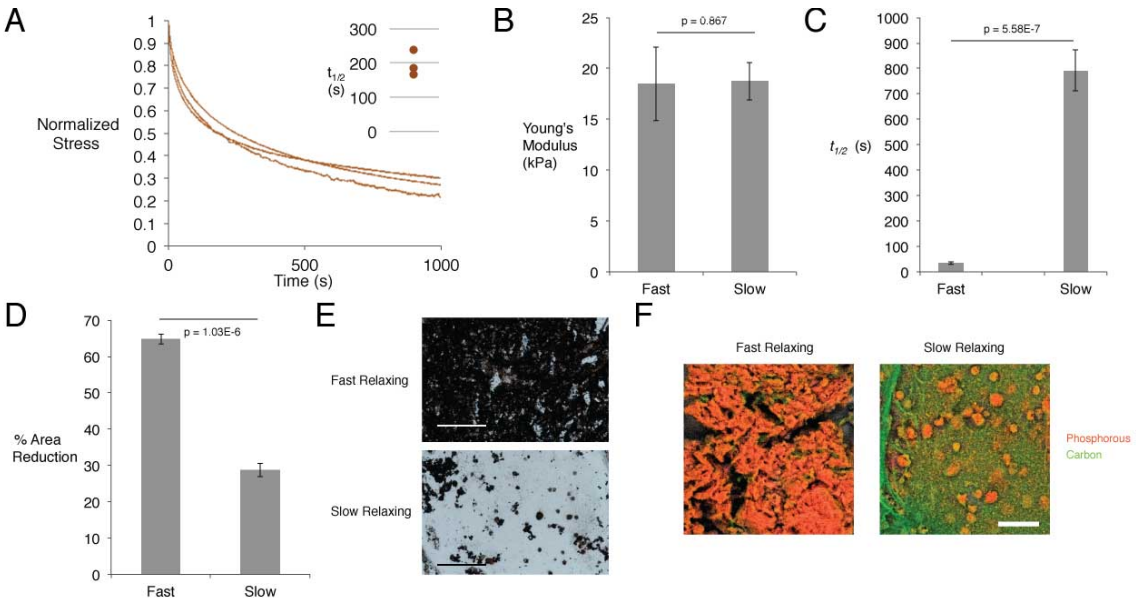

Figure 6
In vitro characterization of alginate hydrogels, and their effects on hMSC osteogenic differentiation. (A) Stress-time curves of human hematomas subjected to compression testing. Curves depict stress relaxation of hematomas held at 15% strain. Inset shows time to 50% of the initial stress in these curves. (B) Young's modulus as determined by compression testing of slow and fast-relaxing alginate hydrogels. (Student's t-test, n=4) (C) Time to 50% stress relaxation at 15% initial strain for slow and fast-relaxing alginate hydrogels. (Student's t-test, n=4) (D) Extent of gel contraction after culture with encapsulated hMSCs for two weeks. (Student's t-test, n=4) (E) Representative von Kossa staining for matrix mineralization between slow and fast-relaxing gels with encapsulated hMSCs in osteo-inductive medium after two weeks. Scale bar represents 300 μm. (F) Representative pseudo-colored EDS elemental maps for slow and fast-relaxing

gels with encapsulated hMSCs in osteo-inductive medium after two weeks. Orange depicts phosphorous and marks phosphate deposition, while green depicts carbon.

Alginate hydrogels were fabricated from either high or low molecular weight polymer to yield distinct rates of stress relaxation, which bracket the rates seen among the hematomas, and their mechanical properties and impact on hMSCs in vitro were first compared. Compression testing confirmed no statistically significant difference in the initial elastic moduli of fast and more slowly relaxing hydrogels (Fig. 6B). As expected, hydrogels fabricated with the high molecular weight alginate demonstrated significantly longer relaxation times than the low molecular weight hydrogels (Fig. 6C). Next, hMSCs were encapsulated in the two types of alginate hydrogels and cultured in osteogenic induction medium for two weeks in order to assess the differences in differentiation of hMSCs in hydrogels with different stress relaxation times. Fast-relaxing gels contracted significantly more than slow-relaxing gels, and, consistent with previous results with mouse stem cells, von Kossa staining of the hydrogels showed significantly more matrix deposition and mineralization for the fast-relaxing hydrogels, indicative of osteogenic differentiation of hMSC (Fig. 6D,E) [14]. To confirm the increased mineralization in fast relaxing gels, energy dispersive X-ray spectroscopy (EDS) was performed to map elemental phosphorous in the interior of the hydrogels. Substantially more phosphorous was found in the fast-relaxing gels, consistent with the von Kossa staining, again indicating a greater osteogenic differentiation of hMSCs and subsequent mineral deposition in the fast-relaxing gels (Fig. 6F).

In order to assess the *in vivo* effects of substrate stress relaxation, both types of hydrogels containing hMSCs, as well as an empty defect control and a fast-relaxing hydrogel without cells, were implanted into a rat (RNU rat) critical-sized (8mm) calvarial defect. For the sake of animal welfare, a slow-relaxing hydrogel without cells was omitted, as *in vitro* results suggested that the condition with cells would already perform sub-optimally [19]. After three months, the rats were euthanized and the skulls were explanted and examined for bone formation using X-ray micro-computed tomography (μCT). An increase in new bone was found for the fast-relaxing hydrogels, and quantification of the new bone volume confirmed a statistically significant difference in the amount of new bone formed and the average percentage of the defect that was spanned by bone, when compared to the gels with slower relaxation (Fig. 7). As expected, the empty defects showed minimal bone regeneration, but intriguingly, the fast-relaxing gels without cells showed healing only slightly less than that of the fast-relaxing gels with cells, with this difference not statistically significant (Fig. 7).

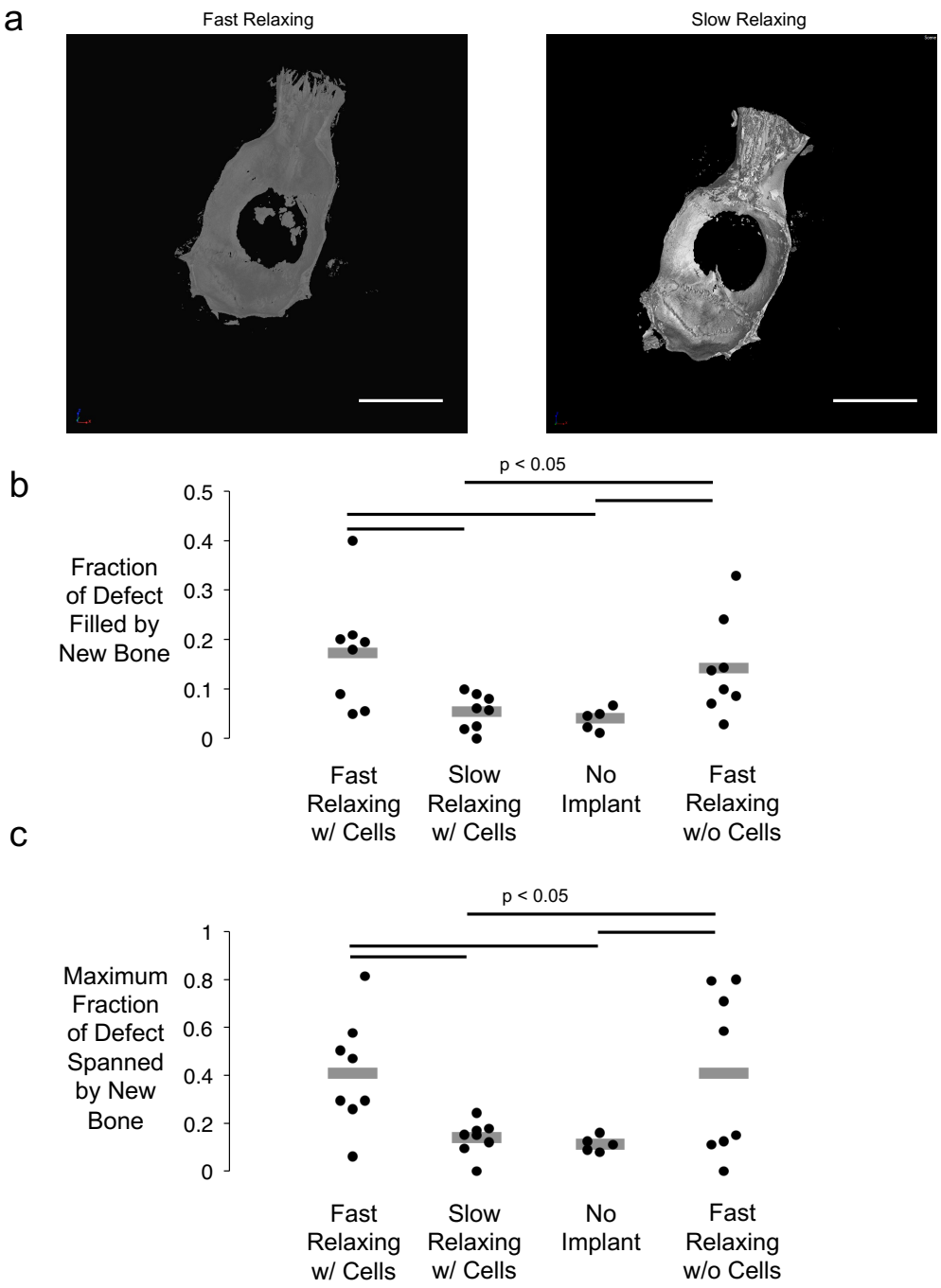

Figure 7

Micro-computed tomography analysis of new bone formation after implantation of hydrogels in rat calvarial defect model. (A) Representative uCT renderings of rat calvaria three months post-injury. Scale bar - 1cm. (B) Maximum fraction of wound spanned after three months calculated by taking the maximum fraction of bone occupying any line drawn through the center of the defect. (One-way ANOVA, Tukey's post-hoc test, n=3-4) (C) Fraction of the original wound area inhabited by new bone after three months. (One-way ANOVA, Tukey's post-hoc test, n=5-8).

The histology of the defects was next examined to assess the structure of the new bone (Figs. 3-4). Masson's Trichrome staining revealed a difference in the thickness of the tissue residing in the defect site, with a nearly two-fold greater thickness in the slow-relaxing case (Fig. 8A-C).

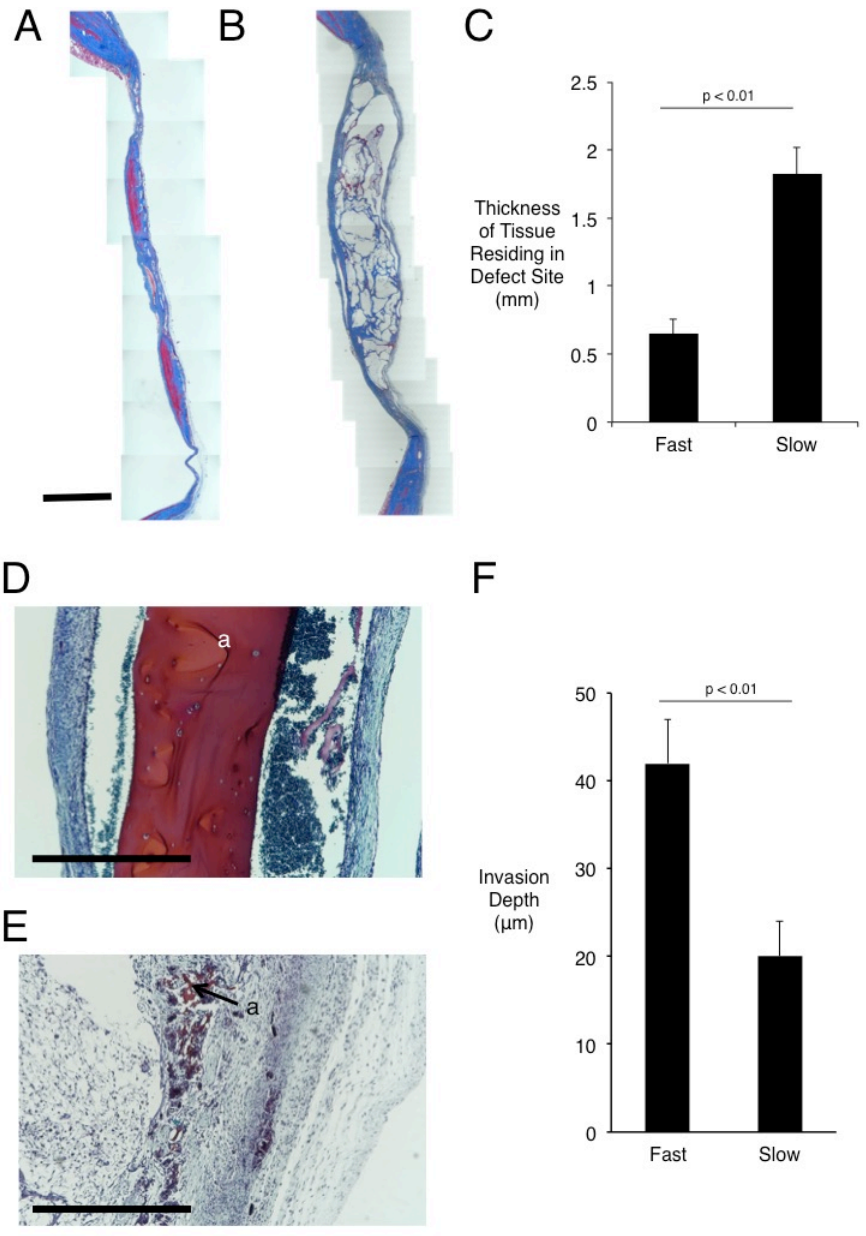

Figure 8
Histological staining and quantification of calvarial wound site remodeling three months post-injury. (A) Masson's Trichrome staining of defect site in fast-

relaxing (A) and slow-relaxing (B) gel conditions. Scale bar – 2mm in A and B. (C) Quantification of thickness of tissue residing in defect site, as determined by measuring tissue sections stained with Masson's Trichrome at various points along the membrane that were incident with the implant (Student's t-test, n=8-10). Error bars represent S.D. (D) Safranin O stain of defect site in slow-relaxing (D) and fast-relaxing (E) cases carrying cells after two weeks of implantation. Scale bars – 1mm. Residual alginate stains red and is marked "a." (F) Quantification of fibroblast infiltration into hydrogels at one week *in vitro* after seeding on surface of gel (Student's t-test, n=15 measurement sites). Error bars represent S.D.

In order to gauge the contribution of hydrogel loss to this thickness effect, fast and slow-relaxing hydrogels bearing cells were explanted after two weeks. Safranin O staining for residual alginate showed an intact gel in the slow-relaxing case, but dramatic remodeling and fibrous tissue infiltration with little remaining alginate in the fast-relaxing case (Fig. 8D,E). Hypothesizing that this effect could be due to the ability of surrounding cells to infiltrate the scaffold, an *in vitro* experiment measuring the infiltration depth of fibroblasts initially seeded on top of the gels after one week showed that cells were able to migrate nearly twice as far into the gel in the fast-relaxing case, consistent with the notion that stress-relaxation modulates the ability of cells to remodel and invade a scaffold (Fig. 8F).

H&E, van Gieson, and Masson's Trichrome stainings of three month histology revealed that the new bone formed in the fast-relaxing condition with cells was mature, featuring collagen-rich and relatively acellular regions with sparse osteocytes (Fig. 9A-C). Furthermore, the presence of elongated osteoblasts on the periphery of the new bone, and osteoid regions rich in disorganized collagen suggest active bone growth. In contrast, the slow-relaxing condition showed sparse, disorganized collagen, without prominent bone growth centers or

mature bone (Fig. 9A-C). Additionally, Alcian Blue staining for residual alginate revealed little remaining hydrogel in the fast-relaxing case, whereas significant residual hydrogel was noted in the slow-relaxing case (Fig. 9D). Coupled with a significantly larger defect thickness for the slow-relaxing condition, these results confirm that the differences in hydrogel remodeling seen at two weeks are maintained through three months (Fig. 8C, 4D).

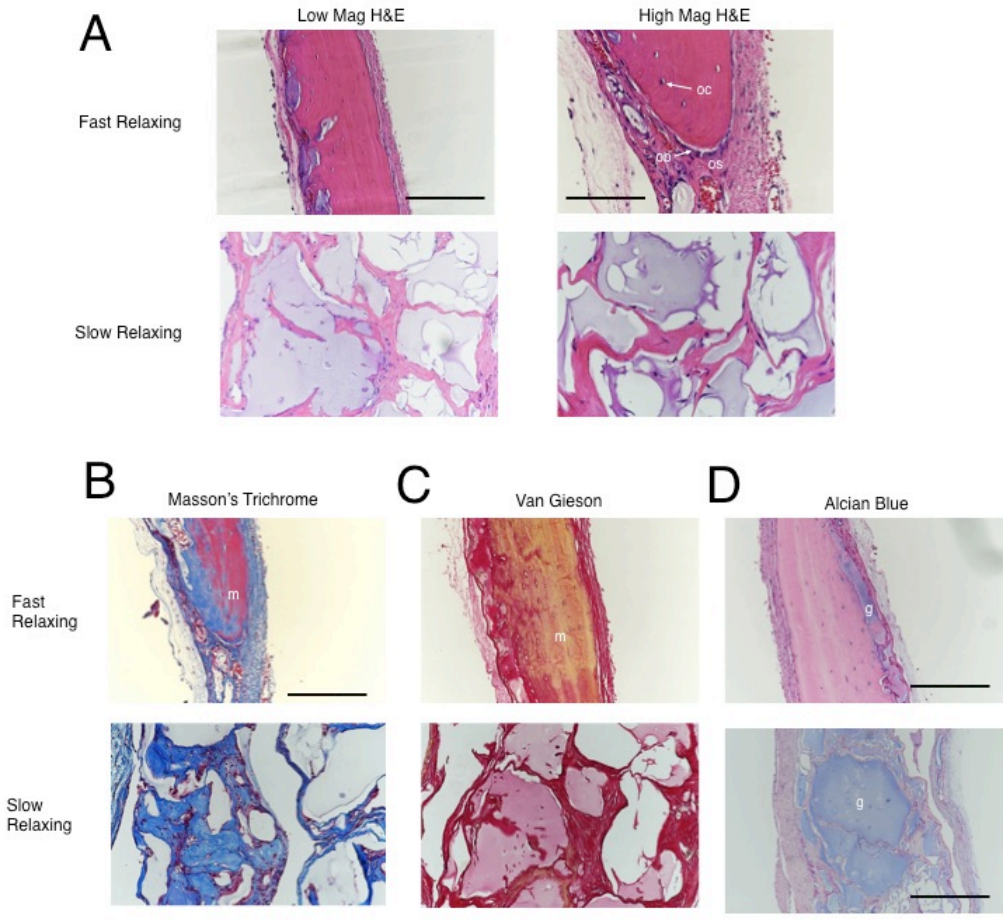

Figure 9
Histological staining of calvarial wound sites three months post-injury. (A) Representative high and low magnification images of Hematoxylin and Eosin stained sections demonstrating new bone in the fast-relaxing case and a disorganized tissue in the slow-relaxing case. 'os' labels the osteoid region, 'oc'

labels osteocytes, and 'ob' labels elongated, activated osteoblasts on the new bone growth front. Low-mag scale bar represents 360 μm and high-mag scale bar represents 180 μm. (B) Representative Masson's trichrome staining demonstrates mature bone ('m') in the fast-relaxing case and disorganized collagen in the slow-relaxing case. Scale bar represents 360 μm. Note the discrepancy in scale due to remodeling effects noted in Figure 3. (C) Representative Van Gieson staining indicates mature bone ('m') in the fast-relaxing case and disorganized collagen in the slow-relaxing case. (D) Representative alcian blue staining to identify residual alginate hydrogel ('g') reveals small remnants in the fast-relaxing case and large remnants in the slow-relaxing case. Scale bar represents 360 μm in the fast-relaxing case and 720 μm in the slow-relaxing case.

In order to gauge the relative contribution of rat versus human cells to the new bone formed in the conditions with transplanted cells, and thus determine the ability of the remodeled scaffold environment to support the viability of transplanted cells, a human mitochondria stain was utilized to label all progeny of the transplanted human cells (Fig. 10).

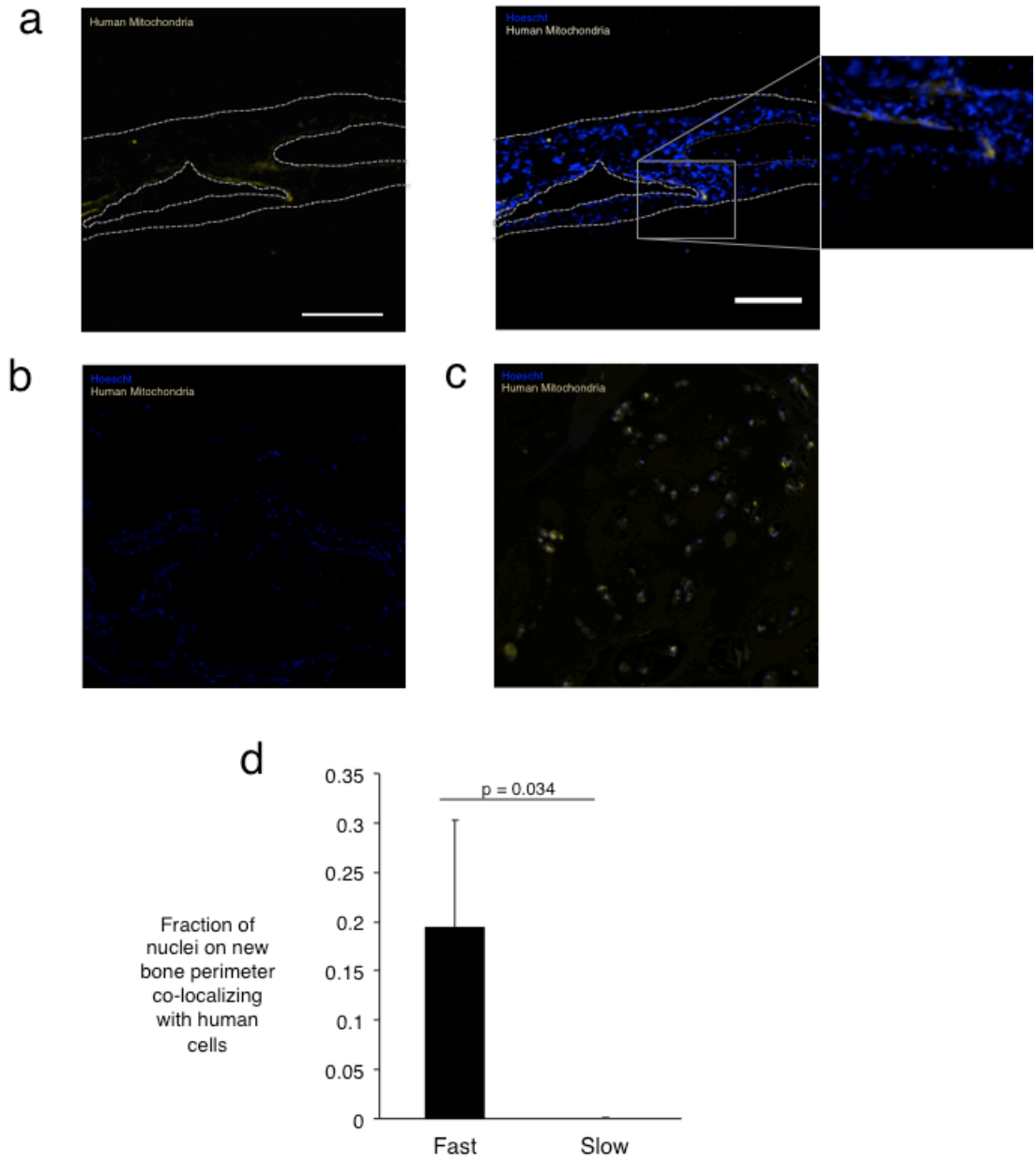

Figure 10
Localization of progeny of transplanted cells in calvarial defect site three months post-injury. (A) Human mitochondrial staining in defects treated with fast-relaxing gels reveals human cells on the new bone periphery. The left panel depicts imaging of the stain used for human mitochondria, while the right depicts the mitochondria overlaid with nuclei stain. The inset shows a higher magnification version of the new bone interface. Scale bar represents 225 μm (B) Human mitochondrial staining in tissues treated with slow-relaxing gel depicting an absence of human cells. (C) Positive control for human mitochondrial staining

in human bone section. (D) Fraction of total cellular nuclei on the new bone perimeter co-localizing with human cells (Student's t-test, n=4). No human cells were detected in the slow-relaxing case. Error bars represent S.D.

Human cells were markedly absent from the slow-relaxing condition, while a small number of human cells were localized to the periphery of new bone in the fast-relaxing condition (Fig. 60A, B). Quantification of the number of cell nuclei on the perimeter of new bone islands co-localizing with human cells, as a measure of the contribution of the transplanted cells to new bone growth, revealed that 20±11% of cells along the new bone periphery were of human origin (Fig. 60D).

Discussion

These results demonstrate that substrate stress relaxation can be a potent regulator of bone formation *in vivo*. Specifically, rat calvarial defects treated with stiffness-matched hydrogels carrying hMSCs or cell free showed significantly more bone formation after three months if the hydrogels exhibited a relatively fast stress relaxation time. As a recent study showed that substrate stiffness can play an important role in bone regeneration *in vivo* [19], those results combined with those of the present study suggest that substrate stiffness together with the stress relaxation timescale can be tuned to optimize the bone-forming capabilities of biomaterials.

The new bone formed in defects with fast-relaxing implants exhibited a morphology of sparse osteocytes, mineralized matrix and osteoid, indicative of the activation of a robust bone regeneration cascade. Given the complicated material and biological environment of bone, the absence of any of these elements

would have suggested that the healing was not taking place in a concerted, directed way. This mature morphology is comparable to the results of previous studies that delivered growth factors such as BMP-2 to defect sites [20], a result that implies a great relative importance of extracellular mechanical properties to bone formation. Based on the apparent potency of both mechanical and biological factors in inducing bone formation, an approach combining mechanical optimization and growth factor delivery, such as one recently reported *in vitro*, could be a promising approach to bone healing in the future [21]. That being said, optimizing each approach in perfect isolation may not be possible, as it has been shown that the interaction between soluble factors and biomaterials, and the resulting differences in the mode of factor presentation to cells are potent regulators of cell behavior [22]. In this situation, biomaterial systems such as that used in this study that allow for the independent control of key material properties will become increasingly important.

The presence of human-derived cells at the new-bone-periphery in conditions with fast-relaxing gels, but absence of human cells in slow-relaxing conditions indicates a role for fast-relaxing gels in providing survival cues to the transplanted cells as well as a persistent role for the remaining cells in the bone healing cascade. Moreover, the presence of these cells in the zone of new bone formation and not in the mature bone suggests that these cells are actively participating in new bone growth. The same fast-relaxing gels without cells demonstrated slightly less regeneration than with cells, supporting a role of the transplanted human cells in new bone formation. A previous study in which

MSCs were encapsulated in alginate hydrogels similar to the slow-relaxing condition here and implanted into subcutaneous pockets in rats reported a marked absence of transplanted cells after just two weeks [23]. In contrast, a study in which MSCs were encapsulated in fibrin gels, which are known to demonstrate stress relaxation, and then implanted into a femoral defect model showed significant persistence of the transplanted cells after four weeks [24]. The current study suggests stress relaxation as a possible mechanism underlying the discrepancy between the past studies. Additionally, previous work showing the effects of adhesion substrate degradation rate on the ability of transplanted osteoblasts to form bone in an ectopic site could perhaps also be related to effect of stress relaxation, as the mechanisms of stress relaxation and degradation in that study were coupled [25].

This study introduces substrate stress relaxation rate as a key regulator of bone regeneration. Several studies using transplanted MSCs have shown the influence of hydrogel degradation on bone regeneration [26, 27], and the findings here raise the possibility that altered relaxation of the hydrogels as they degrade over time could be contributing to some of the results found in those studies. Additionally, in the early stages of bone fracture healing, periosteal MSCs are known to migrate into the hematoma and participate in intramembranous ossification, differentiating into osteoblasts [28, 29]. This study suggests the stress relaxation property of hematomas could mediate both MSC invasion into sites of bone defects and their osteogenic differentiation during bone healing, though such effects are surely mediated by myriad factors such as defect stability and size.

Previously, tissue engineers were limited to chemical and biological factor delivery in order to influence bone regeneration, but as the findings of this and another recent study indicate, tissue engineers can leverage the physical properties of biomaterials, in addition to chemical/biological cues, to improve bone regeneration [19].

Materials and Methods

Alginate Hydrogels

Alginate type LF20/40 (FMC Biopolymer) was used as-received (average molecular weight of 280kDa) for the slow-relaxing hydrogels and was irradiated with an 8mRad cobalt source to form the fast-relaxing hydrogels (average molecular weight of 35kDa). Irradiation lowers the molecular weight while maintaining the same G to M block ratio [8]. Alginates were modified with GGGGRGDSP peptides (Peptide 2.0) at a ratio of 20 peptides per alginate with standard carbodiimide chemistry as described previously [8]. After modification, alginates were dialyzed against a NaCl gradient, treated with activated charcoal, and sterile-filtered. After lyophilization, all alginate was dissolved in serum-free DMEM (Lonza) at 2.5%.

Hydrogels were cast by rapidly mixing the alginate solution with a $CaSO_4$ slurry via two syringes and ejecting the mixture between two glass plates, where it gelled over 1.5 hours. Slow-relaxing gels consisted of 2% LF20/40 alginate and 20mM Ca, while fast relaxing gels consisted of 2% LF20/40 8mRad alginate and 42mM Ca. This difference in calcium concentration has previously been noted to have no effect on mesenchymal stem cell viability and differentiation [14]. 8mm disks were then cut from the gel using a biopsy punch.

Hydrogel Mechanical Characterization

Hydrogels were fabricated as described above at a thickness of 2mm and subjected to compression testing using a mechanical testing device (Instron). Gels

were compressed at a strain rate of 1mm/min and the Young's Modulus was calculated as the best-fit slope of the first 5-15% of the resulting stress/strain curve. At 15% strain, the strain was held and the time required for the stress to decay by a factor of two was noted.

In Vitro hMSC Differentiation

Human mesenchymal stem cells (Rooster Bio) were encapsulated in slow and fast relaxing hydrogels at a final concentration of 15 million cells/mL gel, gels were punched into disks, and placed into 24-well plates. The encapsulated cells were cultured in osteogenic differentiation medium (Stempro, Life Technologies) and cell culture medium was changed every 3-4 days for two weeks.

At two weeks, samples were fixed in 4% paraformaldehyde for 45 min on an orbital shaker, exposed to increasing concentrations of OCT in a sucrose solution, and flash frozen for cryosectioning. Gels were sectioned at a thickness of 50 μm before von Kossa Staining. Briefly, sections were incubated in a 1% silver nitrate solution under ultraviolet light for 20 seconds, rinsed with DI water, and incubated in 5% sodium thiosulfate for 5 min.

Elemental Analysis of hMSC Differentiation

A Tescan Vega environmental scanning electron microscope (SEM) with a Bruker XFlash 5030 energy dispersive X-ray spectrometer (EDS) was used for elemental characterization of *in vitro* hMSC differentiation. Gels were prepared in

frozen blocks as they were for von Kossa staining and then were sectioned at a thickness of 100 μm onto a p-type silicon wafer. Samples were washed in water, followed by drying under vacuum overnight. Elemental analysis and mapping of phosphorus were performed at an accelerator voltage of 20 keV and a pressure of 12 Pa.

Hydrogel Implantation in Rat Calvarial Defect Model

All animal experiments were performed in compliance with National Institutes of Health guidelines and were approved by the Institutional Animal Care and Use Committee at Harvard University. The rat calvarial defect surgery was performed on four-week old RNU Rats (Charles River Laboratories) as described previously [19]. Briefly, animals were anesthetized, and their heads were shaved. A sagittal incision was made along the head and the exposed periosteum was bluntly dissected to the level of the superior temporal line bilaterally. 8mm circular osteotomies were drilled under copious irrigation and the bone removed from the rat calvarium while maintaining the underlying dura intact. 8mm hydrogels encapsulating hMSCs at a density of 10 million cells/mL were implanted into the resulting void. Fascia and skin layers were sutured separately in order to keep the gels stationary.

After two weeks or three months, animals were euthanized with CO_2 and decapitated. The calvarium was removed using bone shears and placed in 10% formalin for 24 hours. Samples were then stored at 4°C in PBS until further use.

X-Ray Micro-Computed Tomography

Rat calvaria were wrapped in paraffin to prevent dehydration and scanned in an X-tek HMXST225 micro-computed tomography system at the Harvard University Center for Nanoscale Systems. Samples were reconstructed using CT Pro and rendered using VG Studio Max software. For new bone quantification in VG Studio Max, an 8mm diameter cylinder volume of interest was centered over the defect site, with a height equivalent to the thickness of the adjacent bone. The volume within the cylinder encapsulated in an isosurface rendering was calculated, and the percent of defect filled was treated as the fraction of the cylinder, thus representing the original defect volume, filled by the new bone. The spanned fraction was calculated by drawing a line through the center of the defect and calculating the fraction of the original defect diameter that contains bone. The reported maximum fraction is the maximum per animal of all of these lines.

Histology

After tomography, samples were sent to the Dana Farber Cancer Rodent Histopathology Core for paraffin embedding and sectioning, as well as Hematoxylin and Eosin, Van Gieson, Masson's Trichrome, and Alcian Blue staining. Imaging was performed on a Nikon histology microscope. Membrane thickness quantification was obtained by using the measure feature in ImageJ (NIH).

Immunofluorescence staining was performed using anti-human mitochondria primary antibodies (Abcam). Paraffin was removed from sections with two 5 minute xylene washes, and slides were rehydrated in successively lower concentrations of ethanol in DI water. For human mitochondria antigen retrieval, samples were incubated in sodium citrate buffer, pH 6.0, at 95°C for twenty minutes. Slides were blocked in 10% normal goat serum, 1% bovine serum albumin, and 0.05% Tween-20 in PBS for 1 hour at room temperature, and incubated in primary antibody solution using the manufacturer's recommended concentrations overnight at 4°C. Slides were then incubated in goat anti-mouse Alexa 555 secondary antibodies (Abcam) for 1 hour at room temperature and counterstained with Hoescht. Imaging was performed on a Carl Zeiss LSM 710 upright confocal microscope and pseudocolored using ImageJ. Quantification of human cells was obtained in ImageJ by first locating fields of view that previously contained hydrogel, thresholding and binarizing the nuclei, followed by masking the mitochondria channel and counting the masked regions that contained red signal, thus yielding the fraction of nuclei that belonged to human cells. Since human cells were not found outside of these fields, these quantities represent the composition of cells in the neighborhood of the implanted hydrogel.

In Vitro Scaffold Invasion Assay

Slow and fast relaxing hydrogels were fabricated as noted above and were cast on coverslips. Coverslips were placed in wells and NIH 3T3 fibroblasts were seeded at a density of 10,000 cells per square centimeter by pipetting a cell

suspension on top of the gels. After twelve hours, the hydrogels were moved to new wells to remove non-adherent cells and the hydrogels were cultured for one week at 37°C. The cells were then fixed with 4% paraformaldehyde for 15 minutes, permeablized with 0.1% Triton X-100 and stained for 15 minutes with rhodamine-tagged phalloidin. The gels were then placed in custom PDMS gaskets on microscope slides and imaged using a Zeiss LSM 710 upright confocal microscope. Z-stacks were captured and the distance from the hydrogel surface to the deepest cell was sampled at five random locations across three different z-stacks using Zeiss ZEN software.

Acknowledgements

The authors would like to thank Christine Cezar for help with

immunofluorescence protocols, and Jon Rowley from Rooster Bio for the hMSCs.

This work was funded by the NIH/NIDCR (R01 DE013033).

Associated Publication

M. Darnell, S. Young, L. Gu, N. Shah, E. Lippens, J. Weaver, G. Duda, D. Mooney, Adv. Healthcare Mater. 2017, 6, 1601185.

References

1. Huebsch, N. & Mooney, D.J. Inspiration and application in the evolution of biomaterials. *Nature* **462**, 426-432 (2009).
2. Murphy, W.L., McDevitt, T.C. & Engler, A.J. Materials as stem cell regulators. *Nat Mater* **13**, 547-557 (2014).
3. Mehta, M., Schmidt-Bleek, K., Duda, G.N. & Mooney, D.J. Biomaterial delivery of morphogens to mimic the natural healing cascade in bone. *Advanced Drug Delivery Reviews* **64**, 1257-1276 (2012).
4. Mooney, D.J. & Vandenburgh, H. Cell Delivery Mechanisms for Tissue Repair. *Cell Stem Cell* **2**, 205-213 (2008).
5. Szpalski, C., Wetterau, M., Barr, J. & Warren, S.M. Bone Tissue Engineering: Current Strategies and Techniques—Part I: Scaffolds. *Tissue Engineering Part B: Reviews* **18**, 246-257 (2011).
6. Mravic, M., Péault, B. & James, A.W. Current Trends in Bone Tissue Engineering. *BioMed Research International* **2014**, 865270 (2014).
7. Smith, B.D. & Grande, D.A. The current state of scaffolds for musculoskeletal regenerative applications. *Nat Rev Rheumatol* **11**, 213-222 (2015).
8. Alsberg, E., Anderson, K.W., Albeiruti, A., Franceschi, R.T. & Mooney, D.J. Cell-interactive Alginate Hydrogels for Bone Tissue Engineering. *Journal of Dental Research* **80**, 2025-2029 (2001).
9. Hao, J. et al. Mechanobiology of mesenchymal stem cells: Perspective into mechanical induction of MSC fate. *Acta Biomaterialia* **20**, 1-9 (2015).
10. Teo, B.K.K., Ankam, S., Chan, L.Y. & Yim, E.K.F. in Methods in Cell Biology, Vol. Volume 98. (ed. G.V. Shivashankar) 241-294 (Academic Press, 2010).
11. Bellas, E. & Chen, C.S. Forms, forces, and stem cell fate. *Current Opinion in Cell Biology* **31**, 92-97 (2014).
12. Chaudhuri, O. et al. Substrate stress relaxation regulates cell spreading. *Nat Commun* **6** (2015).
13. Cameron, A.R., Frith, J.E. & Cooper-White, J.J. The influence of substrate creep on mesenchymal stem cell behaviour and phenotype. *Biomaterials* **32**, 5979-5993 (2011).
14. Ovijit Chaudhuri, L.G., Darinka Klumpers, Max Darnell Sidi A. Bencherif, James C. & Weaver, N.H., Hong-pyo Lee, Evi Lippens, Georg N. Duda , David J. Mooney Hydrogels with tunable stress relaxation regulate stem cell fate and activity. *Nat Materials* **Accepted** (2015).
15. McKinnon, D.D., Domaille, D.W., Cha, J.N. & Anseth, K.S. Biophysically Defined and Cytocompatible Covalently Adaptable Networks as Viscoelastic 3D Cell Culture Systems. *Advanced materials (Deerfield Beach, Fla.)* **26**, 865-872 (2014).
16. Perez, R.A. & Mestres, G. Role of pore size and morphology in musculo-skeletal tissue regeneration. *Materials Science and Engineering: C* **61**, 922-939 (2016).

17. Huebsch, N. et al. Harnessing traction-mediated manipulation of the cell/matrix interface to control stem-cell fate. *Nat Mater* **9**, 518-526 (2010).
18. Spicer, P.P. et al. Evaluation of Bone Regeneration Using the Rat Critical Size Calvarial Defect. *Nature protocols* **7**, 1918-1929 (2012).
19. Huebsch, N. et al. Matrix elasticity of void-forming hydrogels controls transplanted-stem-cell-mediated bone formation. *Nat Mater* **advance online publication** (2015).
20. Haidar, Z., Hamdy, R. & Tabrizian, M. Delivery of recombinant bone morphogenetic proteins for bone regeneration and repair. Part A: Current challenges in BMP delivery. *Biotechnol Lett* **31**, 1817-1824 (2009).
21. Tan, S., Fang, J.Y., Yang, Z., Nimni, M.E. & Han, B. The synergetic effect of hydrogel stiffness and growth factor on osteogenic differentiation. *Biomaterials* **35**, 5294-5306 (2014).
22. Schultz, G.S. & Wysocki, A. Interactions between extracellular matrix and growth factors in wound healing. *Wound Repair and Regeneration* **17**, 153-162 (2009).
23. Mankani, M.H., Kuznetsov, S.A., Wolfe, R.M., Marshall, G.W. & Robey, P.G. In Vivo Bone Formation by Human Bone Marrow Stromal Cells: Reconstruction of the Mouse Calvarium and Mandible. *STEM CELLS* **24**, 2140-2149 (2006).
24. Seebach, E., Freischmidt, H., Holschbach, J., Fellenberg, J. & Richter, W. Mesenchymal stroma cells trigger early attraction of M1 macrophages and endothelial cells into fibrin hydrogels, stimulating long bone healing without long-term engraftment. *Acta Biomaterialia* **10**, 4730-4741 (2014).
25. Alsberg, E. et al. Regulating Bone Formation via Controlled Scaffold Degradation. *Journal of Dental Research* **82**, 903-908 (2003).
26. Hoffman, M.D., Xie, C., Zhang, X. & Benoit, D.S.W. The effect of mesenchymal stem cells delivered via hydrogel-based tissue engineered periosteum on bone allograft healing. *Biomaterials* **34**, 8887-8898 (2013).
27. Hoffman, M.D., Van Hove, A.H. & Benoit, D.S.W. Degradable hydrogels for spatiotemporal control of mesenchymal stem cells localized at decellularized bone allografts. *Acta Biomaterialia* **10**, 3431-3441 (2014).
28. Schindeler, A., McDonald, M.M., Bokko, P. & Little, D.G. Bone remodeling during fracture repair: The cellular picture. *Seminars in Cell & Developmental Biology* **19**, 459-466 (2008).
29. Kolar, P. et al. The Early Fracture Hematoma and Its Potential Role in Fracture Healing. *Tissue Engineering Part B: Reviews* **16**, 427-434 (2010).

CHAPTER 4

Uncovering Complexity in Substrate Sensing Networks

Abstract

The extracellular matrix (ECM) within tissues and organs, and biomaterials that aim to mimic the ECM for therapeutic applications, have been subject to a great deal of experimentation that has revealed key features that regulate cell fate and various aspects of function[1-11]. However, a highly reductionist approach has largely been taken to date, with little effort to understand the interplay and overlap among these various features in terms of how and whether they regulate cell behavior. The lack of a global view of substrate sensing raises questions about our understanding of the number and extent of cellular processes that are sensitive to the substrate, which could impact both the design of new therapeutic biomaterials and the responses to cell and molecular therapies in different tissues. Here we used a material system that allows one to independently control three key variables, substrate stiffness, stress relaxation, and the adhesion ligand density presented to cells in three-dimensional culture to perform a global transcriptomic analysis characterizing early gene expression changes in mesenchymal stem cells (MSCs). We found that each of these variables dramatically impact early MSC gene expression, in a highly coupled manner, although the number of differentially expressed genes as each variable is independently altered varies by orders of magnitude. Gene co-expression network analysis revealed networks that involve overlap with canonical signaling pathways as well as crosstalk with metabolic, cell cycle, immune, and morphogenesis-related processes. Stemming from these networks, MSCs were found to modulate their immunosuppressive capacity in response to inflammatory cytokines as a function of substrate stiffness.

Our findings highlight the importance of crosstalk resulting from the sensing of different material parameters and how the material background of the cell can contextualize molecular inputs, which could have important implications for understanding the substrate contextualization of molecular therapies. Additionally, as biomaterials engineers move to drive desired cell phenotypes using defined material specifications, these results introduce the possibility of developing a quantitative biomaterial design framework.

One of the most obvious differences between tissues in the body is their distinct mechanical and chemical properties, including stiffness. Stiffness has been shown to impact the fate of various cell types in culture and to impact tissue regeneration in vivo[12, 13]. However, many materials systems vary stiffness in ways that are coupled to other material properties, or only allow two-dimensional culture. Here we use ionically-crosslinked alginate hydrogels since they afford independent control of multiple material properties presented to cells in three-dimensional culture. Cell adhesion was enabled by covalently decorating the polymer with fibronectin mimicking RGD peptides[14]. MSCs are widely used today in various basic and clinical studies, with over 600 ongoing clinical trials[15], and here, a clonally-derived mouse MSC line was used to minimize the well described effects of cell-cell heterogeneity found in primary cultures[16]. MSCs encapsulated in these hydrogels maintained high viability and were distributed uniformly throughout the hydrogel (Fig. 11a, 16). Cells were cultured in hydrogels at both a low and a high stiffness that were previously shown to influence MSC fate choice (Fig. 11b)[5, 7]. The zonal mechanism of alginate crosslinking has been previously demonstrated to allow for the maintenance of hydrogel nanostructure even at different levels of crosslinking, minimizing differences in porosity and diffusion through the gels[17]. After 40 hours, we performed RNA-seq in order to, in a global and unbiased way, address the early events involved in MSC stiffness sensing. Hierarchical clustering by gene expression led to clear grouping of biological replicates by stiffness, as expected (Fig. 11c). Differential expression analysis revealed 241 differentially expressed

(DE) genes between soft and stiff materials, including the known mechanosensitive effectors zyxin, mmp9 and mmp13, as well as transcription factors such as E2F7 and TEAD4 (Fig. 11d,e). Enrichment analysis for gene ontology processes run on the 241 DE genes showed significant enrichment for cell cycle, morphogenetic, and metabolic processes (Fig. 11f), consistent with previous studies of the influence of stiffness on cell function.

In order to gain broader insight into the effects of stiffness, we used MetaCore to infer a regulatory network seeded from the DE genes, and from that network, identified significantly enriched regulatory hubs (Fig. 11g). Hubs were identified that relate to MAPK signaling, stem cell maintenance, and the cell cycle, as well as a set of transcription factors that included several early intermediate genes and that encompassed a large space of genetic targets[18, 19]. While consistent with previous studies concerning the role of substrate stiffness in regulating metabolism and the cell cycle[12], the identification of modular signaling hubs such as androgen receptor as well as promiscuous transcription factors such as E2F1 suggest that stiffness-sensing could be involved in crosstalk with a number of other cellular processes.

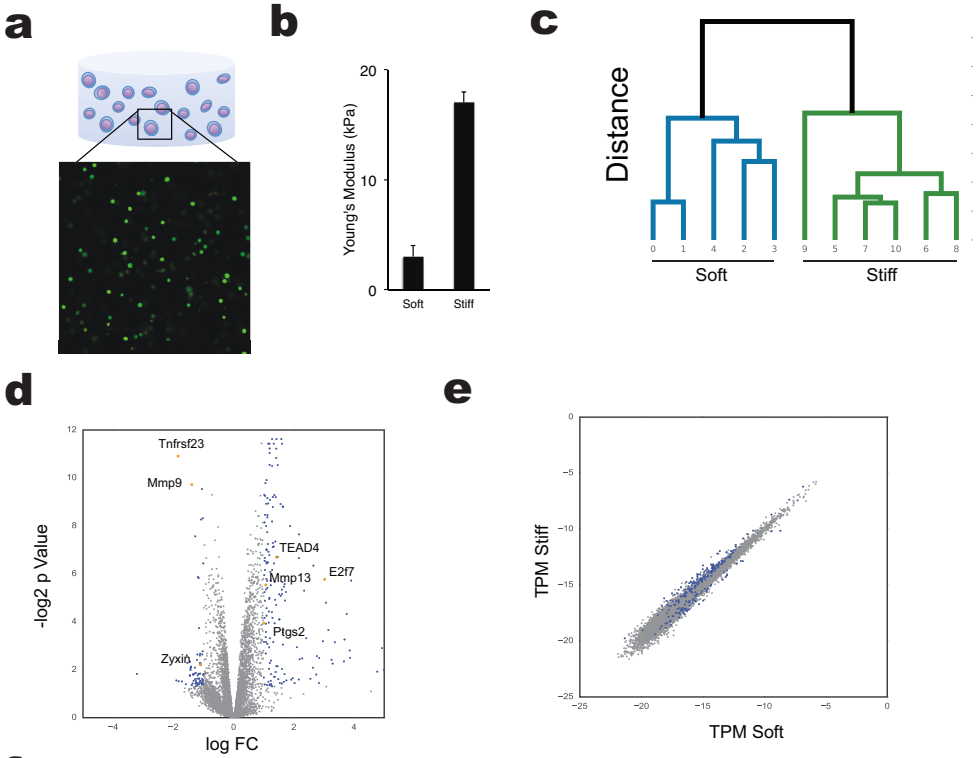

	Factor	FDR	Z-Score
Transcription factors	E2F4	1.10E-20	15.00
	GRHL2	1.08E-09	11.60
	E2F1	6.84E-15	10.34
	TRb/RXRb	6.75E-04	9.65
	GZF1	6.75E-04	9.65
	b-Myb	1.51E-08	8.82
	E2F3/DP1	1.01E-03	8.77
	p63	3.48E-08	7.18
	E2F3	7.29E-07	7.04
	YY1	5.48E-10	7.02
Kinases	CDK1 (p34)	9.20E-19	12.72
	Aurora-B	1.43E-12	11.54
	ATM	3.97E-09	8.39
	PLK1	9.27E-11	8.22
	PALM2	1.40E-03	8.09
	BUBR1	4.74E-06	7.34
	CDK2	1.65E-08	7.15
	PCTK3	1.42E-03	5.89
	SRPK1	2.93E-04	5.83
	Citron	6.21E-04	5.81
Phosphatases	PPP2R5E	1.71E-05	8.26
	PPP2R2A	1.90E-05	6.86
	PPP2R5A	4.82E-04	6.04
	PR61beta	1.76E-03	5.65
	PP2A	7.59E-05	5.33
	B56G	7.57E-04	5.10
	CDC25C	1.03E-03	4.88
	PPP2R2C	4.44E-03	4.65
	VHR	4.87E-03	4.05
Enzymes	APC/hCDH1	3.66E-18	19.06
	DNA	5.62E-07	14.42
	Anaphase-	2.14E-07	12.99
	APC/CDC20	1.88E-07	11.37
	DNA	1.01E-03	8.77
	DBR1	1.40E-03	8.09
	C1TC	7.09E-05	6.99
	CL6S	2.95E-03	6.68
	iPLA2-	2.95E-03	6.68
	LDHA	1.95E-05	6.48
Other	LIN-9	2.59E-11	14.20
	RMND1	2.05E-04	12.57
	CDH1	1.80E-10	11.50
	P38IP	1.74E-06	10.57
	TEX14	1.01E-05	10.32
	CDC27	8.25E-09	10.31
	PRC1	1.80E-07	10.27
	RPS7P4	6.75E-04	9.65
	SNX16	6.75E-04	9.65
	LRIG2	6.75E-04	9.65

Figure 11: RNA-seq analysis of MSC stiffness-sensing. A) Schematic of MSCs encapsulated in alginate hydrogels with representative phalloidin stain showing actual encapsulated cell distribution. B) Young's Moduli of soft and stiff alginate hydrogels. C) Dendrogram of RNA-seq transcripts per million (TPM) showing clustering of replicates by stiffness. The dendrogram uses a complete linkage and

Euclidean distance metric. Numbers indicate replicates, where 0-4 correspond to soft hydrogels and 5-10 correspond to stiff hydrogels. D) Volcano plot showing the log2 fold-change in expression of individual genes in soft versus stiff gels versus the FDR-adjusted p-value for the 8178 filtered genes. Differentially-expressed genes ($p<0.05$ and $\log_2 FC>1$) are shown in blue and selected DE genes are shown in orange and labeled. E) TPM of soft versus stiff samples across all filtered genes. DE genes are highlighted in blue. F) PathwayMap enrichment analysis of DE genes performed using MetaCore software using a hypergeometric test. P-values are FDR adjusted. G) Analysis of highly connected hub genes performed using MetaCore software. Shown are significantly (FDR p-value<0.05) enriched hub genes in sub-networks of up to 50 nodes inferred by seeding with DE genes.

Next we sought to understand how stiffness interacts with stress relaxation and ligand density. Adhesion ligand density was varied from 200 μM to 1500 μM (Fig. 17)[14], spanning an estimated physiologic range (calculations in Supp. Methods) and stress relaxation from $t_{½}$ of 35s to 790s at 15% strain, comparable to stress relaxation values measured in coagulated bone marrow and liver, respectively (Fig. 17)[5]. In order to isolate the effects of each of the three parameters, hydrogels were prepared in eight combinations of the low and high values for each (Fig. 12a), and we again performed RNA-seq on incorporated cells. Hierarchical clustering on the pairwise Spearman correlations between each pair of materials revealed, surprisingly, that materials clustered first by ligand density, then by stress relaxation, and finally by stiffness (Fig. 12b). Pearson correlations of gene expression demonstrated minimal response of the cells to the calcium concentrations in different gels (Fig. 18).

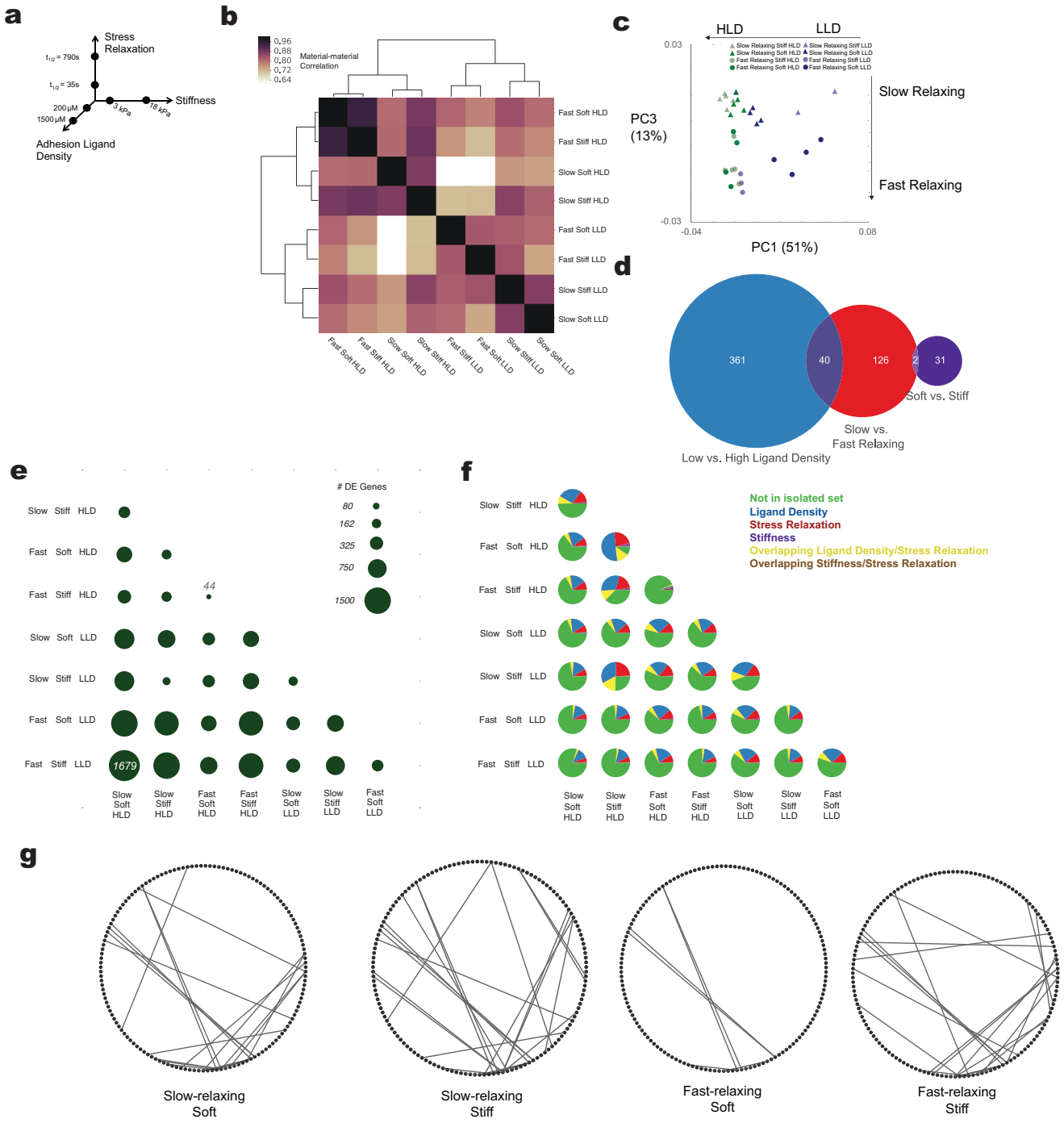

Figure 12: Transcriptomic comparison of material parameter sensing. A) Schematic of experimental conditions. Hydrogels were fabricated in each of the eight combinations of the low and high parameter values. B) Hierarchical clustering of pairwise spearman correlations between each material condition. Correlations were calculated across all filtered genes using the sequencing replicates. Hierarchical clustering uses a complete linkage and Euclidean distance

metric. Dark purple corresponds to high absolute value Spearman correlation. White corresponds to low absolute value Spearman correlation. Fast, fast-relaxing; slow, slow-relaxing; LLD, low adhesion ligand density; HLD, high adhesion ligand density. C) Principal component analysis of gene expression across all replicates for each material. Principal components 1 and 3 correspond to ligand density and stress relaxation separation, respectively. Percentages indicate percent of total variance explained by that component. Fig. 20 shows variance explained by all principal components. Triangles, slow-relaxing; circles, fast-relaxing; Green, high ligand density; purple, low ligand density; Dark, stiff; Light, soft. D) Venn diagram of DE genes for each material parameter comparison after controlling for other parameters. The number of DE genes shared by two parameters are indicated in the overlap in circles. E) Number of DE genes for all pairwise material comparisons. Circle area corresponds to the number of DE genes as indicated in legend. F) Fraction of DE genes from e) described by deconvolved genes in d) for all pairwise material comparisons. Green, DE genes not found in the sets from (d); Blue, DE genes from ligand density set from (d); Red, DE genes from stress relaxation set from (d); Purple, DE genes from stiffness set from (d). Yellow, DE genes from overlapping ligand density and stress relaxation set from (d). G) Representative changes in network topology for comparing ligand density as a function of other background material parameters. The background network is inferred from the four ligand density comparisons (fast-relaxing, soft; fast-relaxing, stiff; slow-relaxing, soft; slow-relaxing, stiff) using Metacore software. These network nodes are arrayed in circles and connections between nodes correspond to Metacore-inferred regulatory connections for comparing ligand density in the specified material background. The network is visualized using Cytoscape.

Principal component analysis identified two principal components that separated conditions based on ligand density and stress relaxation, respectively, but failed to separate conditions by stiffness. Intriguingly, the low ligand density condition that clustered most-closely to the high ligand density conditions was fast-relaxing (Fig. 12c), consistent with previous reports that substrate stress relaxation leads to adhesion ligand clustering[5]. We next used a linear model to extract DE genes affected by one of the parameters regardless of the background parameters. A venn diagram of the resulting deconvolved DE genes strikingly finds a large discrepancy in the number of DE genes for the different parameter comparisons (Fig. 12d). Mirroring the hierarchical clustering of gene expression

previously noted (Fig. 12b), ligand density drove the largest number of DE genes, followed by stress relaxation and then stiffness. qPCR on selected transcripts and material conditions mirrored the sequencing results (Fig. 18). We then performed all contrasts to get the number of DE genes for each material pairwise comparison, and found that the number of DE genes varies by over an order of magnitude, between 44 and 1679. This number far exceeded that of the deconvolved gene sets (Fig. 12e), which suggests the superposition of different independent material sensing mechanisms. We then mapped the deconvolved gene sets to those from each material comparison and found that the covariation of multiple material parameters gives rise to a large increase in the number of DE genes not noted in the deconvolved sets. Moreover, the relative contribution of these gene sets varied dramatically based on the background material parameters, indicating the presence of coupling and switching mechanics in these material-sensitive gene networks (Fig. 12f). While many studies have focused on the effects of specific substrate parameters such as stiffness, few control for the material background parameters. This contextualization of a mechanosensing effect is analogous to other biological processes, such as alteration of growth factor activity by integrin binding[20]. We next explored how varying one material parameter effects the others by taking the DE genes from the four ligand density comparisons in our dataset, each having a different combination of background stress relaxation and stiffness, and using Metacore to infer a regulatory network taking into account all of these comparisons. We found that the regulatory relationships are highly dependent on the background parameters (Fig. 12g).

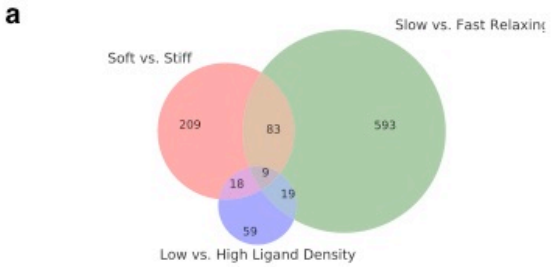

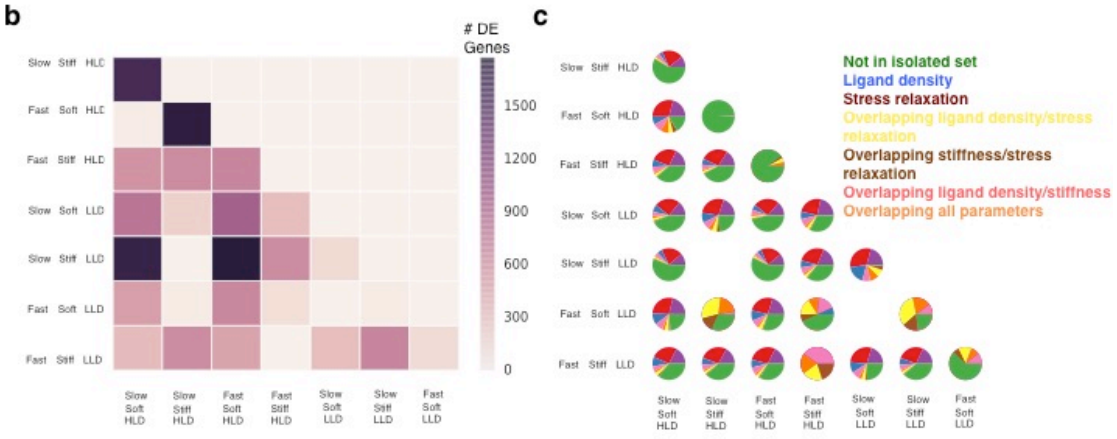

Stiffness

Terms	FDR
Signal transduction_mTORC2 downstream signaling	6.061E-04
Apoptosis and survival_TNF-alpha-induced Caspase-8 signaling	1.193E-02
Regulation of GSK3 beta in bipolar disorder	1.193E-02
Development_Thromboxane A2 signaling pathway	1.193E-02
Cell cycle_Chromosome condensation in prometaphase	1.193E-02
Tau pathology in Alzheimer disease	1.193E-02
Immune response_IL-16 signaling pathway	1.193E-02
Oxidative stress_Activation of NADPH oxidase	1.365E-02
Apoptosis and survival_Role of nuclear PI3K in NGF/ TrkA signaling	1.365E-02
Neurophysiological process_Dopamine D2 receptor transactivation of PDGFR in CNS	1.365E-02
Neurophysiological process_Constitutive and regulated NMDA receptor trafficking	1.365E-02
Apoptosis and survival_nAChR in apoptosis inhibition and cell cycle progression	1.644E-02
NETosis in SLE	1.853E-02
Development_Gastrin in differentiation of the gastric mucosa	3.145E-02

Stress Relaxation

Terms	FDR
Signal transduction_mTORC2 downstream signaling	5.545E-05
Protein folding and maturation_Angiotensin system maturation \ Human version	5.420E-04
Cell cycle_Role of Nek in cell cycle regulation	5.420E-04
Protein folding and maturation_Angiotensin system maturation \ Rodent version	6.747E-04
Cytoskeleton remodeling_Neurofilaments	9.857E-04
Aberrant B-Raf signaling in melanoma progression	1.288E-03
Immune response_IL-4 signaling pathway	1.376E-03
Apoptosis and survival_BAD phosphorylation	1.376E-03
NETosis in SLE	2.061E-03
Cell cycle_Chromosome condensation in prometaphase	3.086E-03
Development_Growth factors in regulation of oligodendrocyte precursor cell survival	4.820E-03
Signal transduction_mTORC1 upstream signaling	5.647E-03
Transcription_Role of heterochromatin protein 1 (HP1) family in transcriptional silencing	5.647E-03
Transcription_Epigenetic regulation of gene expression	5.647E-03
Cell cycle_Initiation of mitosis	5.647E-03
Development_Regulation of cytoskeleton proteins in oligodendrocyte differentiation and myelination	5.647E-03
Transcription_Sin3 and NuRD in transcription regulation	5.647E-03
Immune response_IL-3 signaling via ERK and PI3K	6.973E-03
Immune response_IL-15 signaling	8.138E-03

Ligand Density

Terms	FDR
neuronal signal transduction	1.486E-03
adenosine receptor signaling pathway	1.865E-03
regulation of serotonin secretion	1.865E-03
cellular response to ATP	2.498E-03
G-protein coupled purinergic nucleotide receptor signaling pathway	3.243E-03
synaptic transmission, dopaminergic	3.588E-03
regulation of catecholamine secretion	4.274E-03
regulation of membrane hyperpolarization	4.274E-03
positive regulation of chronic inflammatory response to non-antigenic stimulus	4.274E-03
G-protein coupled purinergic receptor signaling pathway	4.404E-03

Figure 13: Cortical Neuron Progenitor Differential Expression. A) Venn Diagram of the number of DE genes tied to each material parameter. B) Heatmap of the number of DE genes for all pairwise comparisons. Darker color indicates more genes. C) Fractions of DE genes for each pairwise comparison corresponding to deconvolved genes from A). D) Metacore PathwayMap terms corresponding to the deconvolved gene sets from A) for each of the material parameters.

In order to test whether similar relationships generalized to different cell types, we again performed RNA-seq on human iPS-derived cortical neuron progenitor cells (NPCs) cultured in alginate hydrogels with all combinations of low and high stiffness, stress relaxation, and ligand density. We adjusted the low and high stiffnesses used to 1kPa and 10kPa, respectively to reflect the stiffnesses found in the CNS. We found that the deconvolved gene sets tied to each parameter obeyed a different relationship to that of the MSCs, with stress relaxation, then stiffness, then ligand density contributing the most DE genes, although we found more overlap among the different parameters for these cells (Fig. 13a). Mirroring the MSCs, we also found large discrepancies in the number of DE genes across all pairwise material comparisons and again noted the dependence of the response to one parameter on the background parameters (Fig. 13b). Examining the composition of these DE genes revealed that, as with the MSCs, responses to combinations of material parameters result in the differential expression of many genes not otherwise found in the deconvolved sets. However, the presence of DE genes corresponding to the overlap of these deconvolved sets was enhanced (Fig. 13c). Metacore PathwayMap analysis of the deconvolved gene sets revealed terms for neurotransmitter secretion, cytoskeletal remodeling, cell cycle, immune signaling, and pathologies such as Alzheimer's Disease,

suggesting that substrate sensing could play a role in regulating the physiology of the CNS (Fig. 13d). It should also be noted that he list of DE genes for the NPCs includes upwards of forty drug targets. Testing the efficacy of these drugs as a function of the microenvironmental mechanical properties could give insight into mechanical regulation of drug responses *in vivo* and possibly provide clues for how to enhance the efficacy of these drugs. The data from these neural progenitors is consistent with the view of substrate sensing as a complex, coupled, and context-dependent process.

Since certain features of regulatory networks might not be reflected in differential-expression analyses, weighted gene co-expression analysis[21] (WGCNA) was performed on the MSC data to identify modules of highly coexpressed genes that correspond to the sensing of each parameter (Fig. 14a). The three modules with the strongest correlations to our parameters of interest were chosen for further analysis (Fig. 19). Plotting the average module significance for each module as a function of the material confirmed the correspondence of each module to the parameter of interest (Fig. 14b). Metacore PathwayMap enrichment analysis on the member genes for these modules revealed processes involving cytoskeletal remodeling, cell adhesion, and PDGF signaling (Fig. 14c). Inspection of the top hub genes in these modules revealed modular genes involved in signal transduction and protein transport. Of particular note were Klf6 and Klf4 found in the ligand density and stiffness-associated modules, respectively, both of which have been shown to regulate stem cell differentiation. Also of note in the stiffness module were the immune related

kinase Prkra and the YAP target gene Ankrd26, while Ptges2, a key regulator of MSC immunomodulation was noted in the stiffness module (Fig. 14d). The correlation of each of these modules to the others identified by WGCNA, along with the corresponding ontology annotation provided a quantitative metric for the inferred regulatory connectedness of the sensing of a material property with other cellular processes (Fig. 14e). Intriguingly, we found that certain immune-related processes such as PDE4 expression, TNF-induced NFkB signaling, and IL-3 signaling were enriched in modules with strong correlations to the one of the modules of interest (Fig. 14e). These results were used to inform a putative limited network of material-sensitive genes that again revealed the prominent presence of MAPK, Wnt, and TGFb signaling pathways, and genes involved in cell adhesion such as FAK and integrins was noted (Fig. 14f). These results are consistent with studies linking each of these pathways to substrate-sensing[1, 12]. Since a large number of ligands activate these pathways, including many drug targets, implications for crosstalk between molecular signaling and substrate sensing are potentially far reaching[22-24].

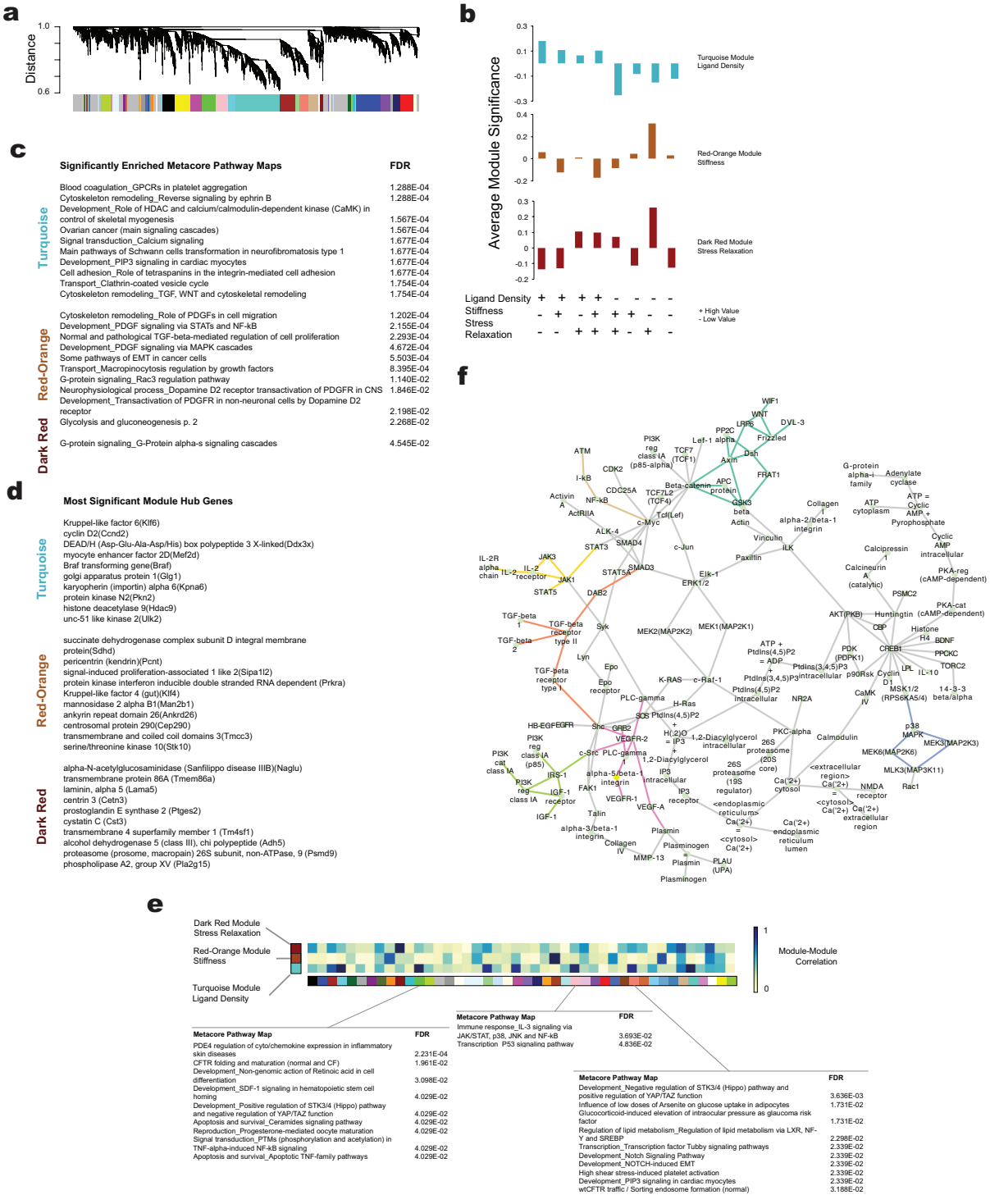

Figure 3: Weighted gene co-expression analysis of material parameter sensing networks. A) Cluster dendrogram of gene expression showing module identification from WGCNA analysis using an unsigned network and a soft thresholding parameter of 10. Genes appear on the horizontal axis and are clustered based on correlation across the RNA-seq dataset. Module colors

correspond to the clusters of coexpressed genes chosen from the dendrogram using the soft thresholding procedure. B) Selection of modules that most closely map to ligand density, stiffness, and stress relaxation. Average module significance is plotted as a function of each material, showing the correspondence between the module and that parameter of interest. These modules are identified in Fig. 19. C) Top Significant Metacore Enriched Pathway Maps for the member genes of the three modules of interest. D) Most significant hub genes for each module of interest. Genes were identified by the WGCNA networkScreening function as having high intramodular connectivity and correlation to the parameter of interest for each module (stiffness, stress relaxation, ligand density). E) Heatmap showing absolute value of spearman correlations between the turquoise, orange-red, and dark red modules and all other modules, calculated by correlating the expression levels of genes for each module. Module member genes for select comparisons showing particularly high or low correlations to the turquoise, orange-red, and dark red modules were selected and the most significant Metacore PathwayMaps were identified. Blue corresponds to high correlations and white to low correlations. F) Putative gene network seeded using the top hub genes from each of the modules corresponding to ligand density, stiffness, and stress relaxation (turquoise, red-orange, dark red). Enriched sub-networks were inferred using Metacore software and the three most significantly-enriched (highest z-score) sub-networks were chosen and merged to arrive at the network shown. Connections corresponding to the Wnt (teal), TGFb (orange), VEGF (pink), NFkB (brown), Jak/STAT (yellow), IGF (green), and MAPK (purple) pathways are highlighted.

Inspection of the inferred gene networks, regulatory hubs, and enrichment analyses revealed a link between substrate sensing and immune modulation. While the influence of substrate properties on MSC differentiation has been widely studied, an understanding of their influence on immunosuppresion is lacking, in spite of the many clinical trials exploiting this function of MSCs[10]. We chose to focus on NF-kB, as it is responsive to substrate stiffness, acts as a signaling hub for immunosuppression[25, 26], and its enrichment in our inferred material-responsive networks suggests that substrate stiffness could affect NF-kB. We first selected a stiffness comparison from the RNA-seq data and performed Metacore network analysis on the DE genes. Inspection of the significant sub-

networks revealed a network linking cell adhesion to an NFkB hub via the PI3K/Akt pathway (Fig. 15a).

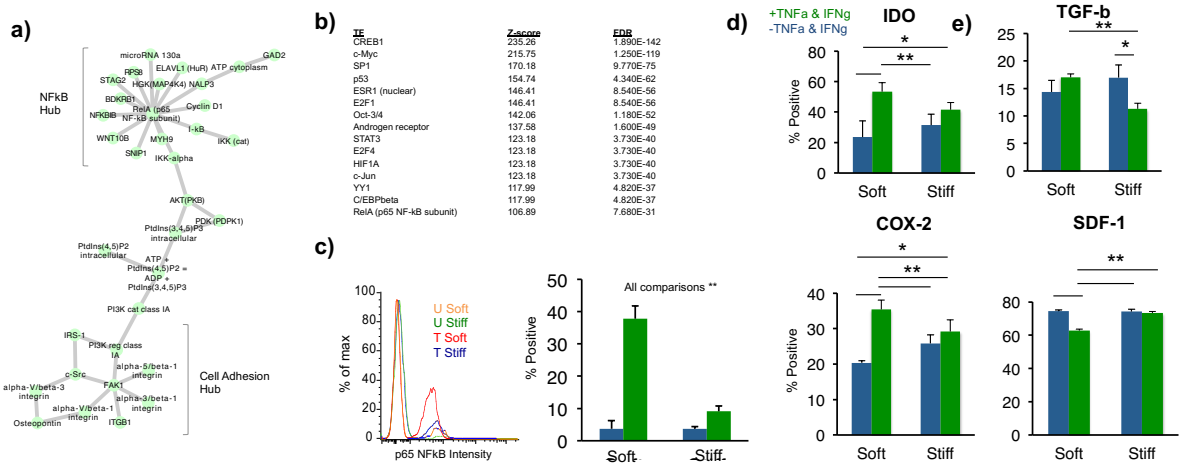

Figure 15: Effects of substrate stiffness on MSC immunosuppressive and differentiation markers. A) Network identified by Metacore AnalyzeNetwork function seeded with DE genes from RNA-seq data in soft vs. stiff slow-relaxing, low ligand density hydrogels. This network was selected as having enriched immune-related gene ontology processes as well as crosstalk between an NFkB hub and a cell adhesion hub. Network was visualized using Cytoscape. B) Significantly enriched inferred transcription factor hubs identified by Metacore after seeding with DE genes from RNA-seq data in soft vs. stiff slow-relaxing, low ligand density hydrogels. C) (Left) Overlaid representative flow cytometry histograms of pNFkB-p65 expression in MSCs stimulated for 4 days in soft or stiff slow-relaxing, low ligand density hydrogels with or without IFNg and TNFa. Orange, untreated (U), soft; Indigo, treated (T), stiff; Green, untreated (U), stiff; Red, treated (T), soft. (Right) Quantification of % pNFkB-p65+ cells. Green, with stimulation. Blue, without stimulation. (One-way ANOVA, Tukey post-hoc test, ** $p<0.01$). D) Percentage of MSCs positive for IDO and COX-2, respectively, after stimulation for 4 days in soft or stiff slow-relaxing, low ligand density hydrogels with or without IFNg and TNFa. Green, with stimulation. Blue, without stimulation. (One-way ANOVA, Tukey post-hoc test, * $p<0.05$, ** $p<0.01$). E) Percentage of MSCs positive for TGFb and SDF-1, respectively, after stimulation for 4 days in soft or stiff slow-relaxing, low ligand density hydrogels with or without IFNg and TNFa. Green, with stimulation. Blue, without stimulation. (One-way ANOVA, Tukey post-hoc test, * $p<0.05$, ** $p<0.01$).

Additionally, inference of transcription factors likely driving the DE genes identified NFkB-p65 (RelA) as significantly enriched (Fig. 15b). Stiffness was

then compared in the same low-ligand density, slow-relaxing gels and the MSCs were cultured in media with or without the known NF-kB activators TNFa and IFNg. Analysis for activated NFkB-p65 showed that soft substrates enhanced enrichment with stimulation (Fig. 15c). The downstream effects of this enrichment were then explored by examining expression of MSC immunomodulatory markers IDO, TGF-b, SDF-1, and COX-2. Stimulation upregulated IDO and COX-2 to a greater extent on soft substrates that on stiff ones, indicating that the stiffness of the substrate can be used to enhance the immunomodulatory effects of MSCs (Fig. 15d). Altogether these results suggest that MSC immunomodulation is dependent on the inflammatory milieu and substrate of the cell. This is likely to have implications in the use of MSCs in a variety of therapies. A precedent for these results is found in the context-dependent regulation of transcriptional modules in immune cells[27].

These findings demonstrate that the influence of substrate adhesion ligand density, stiffness, and stress relaxation on MSCs is highly interdependent and far-reaching. We also demonstrate that substrate mechanical properties modulate MSC immunomodulatory behavior in response to pro-inflammatory cytokines, showing that a molecular signal can be contextualized by the material microenvironment of the cell. As the design space open to biomaterials engineers is now vast, a systems-level understanding of substrate sensing will help define new material design rules. Additionally, given the diverse substrates in the body, mapping these axes of regulation is critical to designing and understanding new

molecular therapeutics as well as the delivery and engraftment of cell therapies. Overall, we expect that a global and network view of material-sensing will allow for a variety of new behaviors in various cell types to be engineered through biomaterials and an improved understanding of the context-dependence of molecular therapies.

References

1. Sun Y, Villa-Diaz LG, Lam RH, Chen W, Krebsbach PH, Fu J. Mechanics regulates fate decisions of human embryonic stem cells. PLoS One. 2012;7.
2. McBeath R, Pirone DM, Nelson CM, Bhadriraju K, Chen CS. Cell shape, cytoskeletal tension, and RhoA regulate stem cell lineage commitment. Dev Cell. 2004;6.
3. Engler AJ, Sen S, Sweeney HL, Discher DE. Matrix elasticity directs stem cell lineage specification. Cell. 2006;126.
4. Engler A, Bacakova L, Newman C, Hategan A, Griffin M, Discher D. Substrate compliance versus ligand density in cell on gel responses. Biophys J. 2004;86.
5. Ovijit Chaudhuri LG, Darinka Klumpers, Max Darnell Sidi A. Bencherif, James C. , Weaver NH, Hong-pyo Lee, Evi Lippens, Georg N. Duda , David J. Mooney. Hydrogels with tunable stress relaxation regulate stem cell fate and activity. Nat Materials. 2015;Accepted.
6. Cameron AR, Frith JE, Cooper-White JJ. The influence of substrate creep on mesenchymal stem cell behaviour and phenotype. Biomaterials. 2011;32(26):5979-93.
7. Huebsch N, Arany PR, Mao AS, Shvartsman D, Ali OA, Bencherif SA, et al. Harnessing traction-mediated manipulation of the cell/matrix interface to control stem-cell fate. Nat Mater. 2010;9(6):518-26.
8. Chaudhuri O, Gu L, Darnell M, Klumpers D, Bencherif SA, Weaver JC, et al. Substrate stress relaxation regulates cell spreading. Nat Commun. 2015;6.
9. Huebsch N, Mooney DJ. Inspiration and application in the evolution of biomaterials. Nature. 2009;462(7272):426-32.
10. Kim N, Cho S-G. Clinical applications of mesenchymal stem cells. The Korean Journal of Internal Medicine. 2013;28(4):387-402.
11. Yang C, Tibbitt MW, Basta L, Anseth KS. Mechanical memory and dosing influence stem cell fate. Nat Mater. 2014;13(6):645-52.
12. Mammoto A, Mammoto T, Ingber DE. Mechanosensitive mechanisms in transcriptional regulation. Journal of Cell Science. 2012;125(13):3061.
13. Huebsch N, Lippens E, Lee K, Mehta M, Koshy ST, Darnell MC, et al. Matrix elasticity of void-forming hydrogels controls transplanted-stem-cell-mediated bone formation. Nat Mater. 2015;advance online publication.

14. Alsberg E, Anderson KW, Albeiruti A, Franceschi RT, Mooney DJ. Cell-interactive Alginate Hydrogels for Bone Tissue Engineering. Journal of Dental Research. 2001;80(11):2025-9.
15. Health USNIo. ClinicalTrails.gov [cited 2016]. Available from: http://www.clinicaltrials.gov.
16. Diduch DR, Coe MR, Joyner C, Owen ME, Balian G. Two cell lines from bone marrow that differ in terms of collagen synthesis, osteogenic characteristics, and matrix mineralization. The Journal of Bone & Joint Surgery. 1993;75(1):92.
17. Lee KY, Mooney DJ. Alginate: properties and biomedical applications. Progress In polymer science. 2012;37(1):106-26.
18. Janmey PA, Wells RG, Assoian RK, McCulloch CA. From tissue mechanics to transcription factors. Differentiation; research in biological diversity. 2013;86(3):112-20.
19. Ng H-H, Surani MA. The transcriptional and signalling networks of pluripotency. Nat Cell Biol. 2011;13(5):490-6.
20. Yamada KM, Even-Ram S. Integrin regulation of growth factor receptors. Nat Cell Biol. 2002;4(4):E75-E6.
21. Zhang B, Horvath S. A General Framework for Weighted Gene Co-expression Network Analysis. Stat Appl Genet Mol Biol. 2005;4.
22. Chen JC, Jacobs CR. Mechanically induced osteogenic lineage commitment of stem cells. Stem Cell Research & Therapy. 2013;4(5):1-10.
23. Kim JB, Leucht P, Lam K, Luppen C, Ten Berge D, Nusse R, et al. Bone regeneration is regulated by wnt signaling. J Bone Miner Res. 2007;22.
24. Wozniak MA, Cheng CQ, Shen CJ, Gao L, Olarerin-George AO, Won K-J, et al. Adhesion Regulates MAP Kinase-Ternary Complex Factor Exchange to Control a Proliferative Transcriptional Switch. Current biology : CB. 2012;22(21):2017-26.
25. Nam J, Aguda BD, Rath B, Agarwal S. Biomechanical Thresholds Regulate Inflammation through the NF-κB Pathway: Experiments and Modeling. PLoS ONE. 2009;4(4):e5262.
26. Young SRL, Gerard-O'Riley R, Harrington M, Pavalko FM. Activation of NF-κB by Fluid Shear Stress, but not TNF-α, Requires Focal Adhesion Kinase in Osteoblasts. Bone. 2010;47(1):74-82.
27. Jojic V, Shay T, Sylvia K, Zuk O, Sun X, Kang J, et al. Identification of transcriptional regulators in the mouse immune system. Nat Immunol. 2013;14(6):633-43

Materials and Methods

Casting of Alginate Hydrogels

Alginate type LF20/40 (FMC Biopolymer) was used as-received for the slow-relaxing hydrogels and was irradiated with an 8mRad cobalt source to form the fast-relaxing hydrogels. Irradiation has been shown to lower the molecular weight while maintaining the same G to M block ratio[1]. Alginates were modified with GGGGRGDSP peptides (Peptide 2.0) at the reported densities with standard carbodiimide chemistry as described previously[2]. After modification, alginates were dialyzed against a NaCl gradient, treated with activated charcoal, and sterile-filtered. After lyophilization, all alginate was dissolved in serum-free DMEM (Lonza) at 2.5%.

Hydrogels were cast by rapidly mixing the alginate solution with a $CaSO_4$ slurry via two syringes and ejecting the mixture between two glass plates, where it gelled over 1.5 hours. Stiff slow-relaxing gels consisted of 2% LF20/40 alginate and 20mM Ca, while fast relaxing gels consisted of 2% LF20/40 8mRad alginate and 42mM Ca. Soft slow-relaxing gels consisted of 2% LF20/40 alginate and 8mM Ca, while fast relaxing gels consisted of 2% LF20/40 8mRad alginate and 19mM Ca. This difference in calcium concentration has previously been noted to have no effect on mesenchymal stem cell viability and differentiation [3]. 8mm disks were then cut from the gel using a biopsy punch.

Estimation of Physiologic Range of Adhesion Ligand Concentration

Two methods were used to derive relevant physiologic ranges of adhesion ligand concentration. Developing de-cellularized myocardium was found by mass spectroscopy to contain predominantly Collagen I and at a concentration of ~500ng collagen/g tissue[4]. At a 2% protein concentration, comparable to our hydrogel's overall polymer content, this implies a 1e15 collagens/mL. With seven integrin binding sites per collagen, this value implies a 70 μM concentration of integrin binding sites.

A second reference measured collagen concentrations in breast tissue, finding ~50mg/mL collagen[5]. At a molecular weight of ~300kDa, this concentration is equivalent to 170 μM. Again, at seven integrin binding sites per collagen, this value implies a binding site concentration of 1190 μM.

Hence, given these methods to estimate an order of magnitude for the number of adhesion sites, and given numerous other papers that show at least tenfold changes in ECM component concentrations as a function of tissue, age, and disease, our range of adhesion ligand densities falls within a physiologically reasonable range.

Hydrogel Mechanical Characterization

Hydrogels were fabricated as described above at a thickness of 2mm and subjected to compression testing using a mechanical testing device (Instron). Gels were compressed at a strain rate of 1mm/min and the Young's Modulus was

calculated as the best-fit slope of the first 5-15% of the resulting stress/strain curve. At 15% strain, the strain was held and the time required for the stress to decay by a factor of two was noted.

15% strain was chosen based on previous reports of cell-mediated strains in hydrogels and tissues. Material strains of 20-30% have been observed in the vicinity of fibroblasts in 3D hydrogel culture[6], while strains of 40% have been reported in the skin of the knee[7], 30% in muscles during contraction[8], and around 15% in the lung during breathing[9], suggesting that materials experience comparable levels of strain in cell-laden environments.

RGD Peptide Quantification

RGD coupling density was determined using the LavaPep assay following the manufacturers instructions. Coupled alginate was dissolved at a concentration of 0.1 mg/mL in PBS before incubation with the LavaPep reagents. A standard curve of GGGGRGDSP peptides was prepared in PBS containing 0.1 mg/mL uncoupled alginate as background. Fluorescence was read using a Biotek plate reader and the resulting concentration was used to find the molar ratio of alginate to peptide. Molar concentration of peptide was calculated assuming a 2% alginate gel from the molar ratio.

Cell Culture

D1 mouse mesenchymal stem cells (MSCs) (ATCC) were encapsulated in the hydrogels during the mixing step at a concentration of 10 million cells/mL.

Immediately before mixing, cells were rinsed and centrifuged twice to ensure the removal of any residual ECM components. After casting and punching, gels were placed in 24-well plates and cultured at 37 C in DMEM (Lonza) with 10% fetal bovine serum and 1% penicillin/streptomycin.

For the differentiation of iPSCs into NSCs, the protocol of Rigamonti was used in which a spinning bioreactor containing mTesr media (Stem Cell Technologies) including Rock inhibitor was seeded with single cells from the iPSC line 1016A. A neural fate was induced on day 2 through the addition of SB431542, 10μM; LDN193189, 100nM and XAV939, 2μM. Starting at day 3, the media was stepped from KSR media (15% Knock Out Serum Replacement, KnockOut DMEM, 1x Glutamax, 1x NEAA, 1x Pen/Strep, 1x BME) to NIM media (DMEM-F12,1x N2 supplememnt, 1x B27 -VitA Supplement, 1x Glutamax, 1x NEAA, 1x Pen/Strep). On day 10, the spheres were collected and dissociated with trypsin before seeding onto a tissue culture plate coated with laminin, polyornithine, and fibronectin. Cells were trypsinized and collected before encapsulation in the alginate gels.

Live-Dead Staining

Gels were treated with Life Technologies Live/Dead reagent per the manufacturer's specifications and were then transferred to a microscope slide with a custom-made PDMS well. A coverslip was placed over the hydrated gel and the gels were imaged on a Zeiss LSM 710 upright confocal microscope. Viability was

quantified by computing the number of live and dead cells across five representative fields of view using ImageJ.

Cell Retrieval from Gels

After 40 hours of culture, gels were removed from the wells and placed into eppendorf tubes with 50mM EDTA in HEPES on ice for 10 minutes. An equal volume of trypsin-EDTA was then added to the tubes for an additional 5 minutes at 37C to ensure the removal of cells from the alginate chains. Cells were centrifuged and rinsed twice before proceeding to additional analysis.

RNA-seq

After cell retrieval as described above, cells were lysed and total RNA was extracted per manufacturer's instructions with the Qiagen RNeasy Micro kit. Samples were then submitted to the Harvard Medical School Biopolymers Facility, where mRNA enrichment and library preparation was performed. Individual samples were barcoded and run on two lanes of an Illumina HiSeq 2500 Rapid. The data presented here represents two independent sequencing experiments that were pooled to yield the reported number of replicates per sample.

Flow Cytometry

After cell retrieval as described above, cells were treated with the Life Technologies Fixable Live/Dead stain, then fixed for 10 minutes with 4%

paraformaldehyde on ice. For intracellular staining, an additional 10 minutes of permeablization with Triton-X100 was performed, before blocking for 30 minutes with 5% bovine serum albumin, 0.5% Tween-20 in PBS. Primary antibodies (or pre-conjugated antibodies) were incubated at the below indicated concentrations or two hours, and secondary antibodies were incubated at a concentration of 1 μg/mL for one hour on ice. Samples were run on a BD LSRII flow cytometer at the Harvard Center for Systems Biology Bauer Core facility and data was analyzed using FlowJo. Example gates for are given in Figure 22.

Statistical Methods

Statistics for RNA-seq experiments are described in the RNA-seq Analysis section. For flow cytometry experiments, Igor Pro software was used to run one-way ANOVA, followed by a Tukey-post-hoc test.

RNA-seq Differential Expression Analysis

Raw reads were aligned to the UCSC Genome Browser mm10 genome using Subread[10] and counts were aggregated per gene using FeatureCount16[1]. Since multiple independent sequencing experiments were run, we removed batch effects be applying ComBat to the counts data across the replicates for each experimental condition. After aggregating read counts, we performed TMM normalization. Voom[12] and Limma[13] were then used to perform differential expression analysis using a multi-level factorial design. Differentially-expressed genes were defined as those with a fold-change of at least 2 and a BH-adjusted p-value of less than

0.05. TPM was calculated after applying TMM normalization and variance stabilization. Principal component analysis was coded manually using the TPM for each biological replicate.

Weighted Gene Coexpression Network Analysis (WGCNA)

WGCNA[14,15] was run on TPM data and the topological overlap matrix was calculated using an unsigned network and a soft power of 10. Modules were defined using the dynamic tree cut algorithm. Module significance for stiffness, stress relaxation, and ligand density was computed for each module by correlating the expression of module member genes each parameter encoded as low (0) or high (1) and taking the average gene significance for that module. The most significant genes for each module were found using the NetworkScreening function and were defined as those having high module membership and high intra-modular connectivity.

Metacore Network Analysis

For the Figure 1 analysis, the DE genes were imported into MetaCore and used as the seed genes for finding enriched PathwayMaps and hub genes using the MetaCore standard analysis pipelines. In Figure 2g, the DE genes from all four ligand density comparisons were aggregated and used as the seeds for the Metacore AnalyzeNetwork function, which yielded an overall network. Then for each individual comparison, the regulatory connections from the overall network that would have been yielded if the AnalyzeNetwork function had just been run

on that comparison were highlighted. These networks were imported into Cytoscape and visualized in order to give a qualitative picture for how the regulatory connections in a background material-sensitive network change as a function of the background material parameters. In

For Figure 3, the member genes for the three modules of interest were used as the seed genes to identify inferred PathwayMaps (Fig. 14c) and regulatory hubs (Fig. 14d). In Fig. 14e, the member genes corresponding to modules with high or low module-module correlations were used as seeds and the PathwayMap enrichment analysis was performed. P-values are BH-adjusted. In Fig. 14f, the member genes from the three modules of interest were combined and used as seeds for the Metacore AnalyzeNetwork function. This function yields sub-networks that are ranked by an enrichment score. We selected and merged the top three sub-networks to arrive at the network shown in Fig. 14f, which represents a putative version of a network that captures material-sensing behaviors across our parameters of interest. In Fig. 15a, the AnalyzeNetwork function was again used after being seeded with the DE genes from the low ligand density, slow-relaxing, stiffness comparison. The sub networks were inspected to find a network enriched for immune processes as well as the presence of NFkB. This sub-network was selected and visualized using Cytoscape.

qPCR

Cells were retrieved from gels as described above and total RNA was extracted using the Qiagen RNeasy micro kit following manufacturer's instructions. Reverse transcription was carried out using BioRad iScript Advanced cDNA synthesis kit and PrimePCR validated primers (Table S2) along with BioRad sso Advanced Universal SYBR Green Supermix were used for the qPCR assay. Samples were run on a BioRad QFX96 at the Harvard Center for Systems Biology Bauer Core facility. Relative expression was calculated from normalized ΔCt values using a GAPDH housekeeping gene.

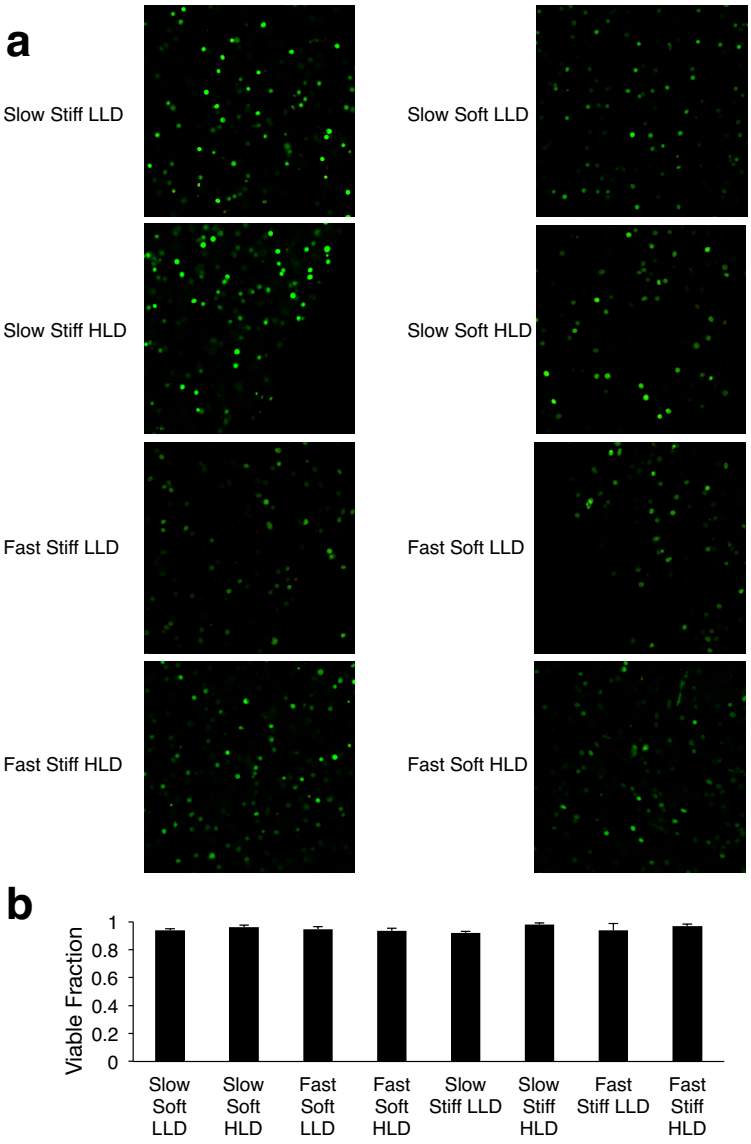

Figure 16: Viability and distribution of MSCs in hydrogels

a) Live/Dead staining of MSCs in hydrogels. Live cells appear green and dead cells appear red.

b) Quantification of fraction of viable cells in hydrogels, computed from five representative fields of view for each gel. Cells were segmented and counted using ImageJ. Error bars represent S.D.

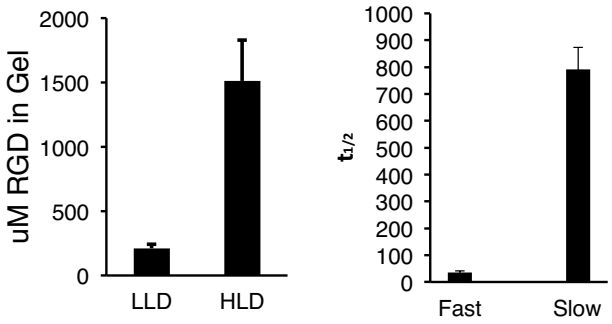

Figure 17: Characterization of RGD-coupled alginate hydrogels

a) Quantification of RGD coupling per LavaPep assay. Error bars represent S.D.
b) Time to achieve 50% relaxation of maximal stress in hydrogels when held at 15% strain. Error bars represent S.D.

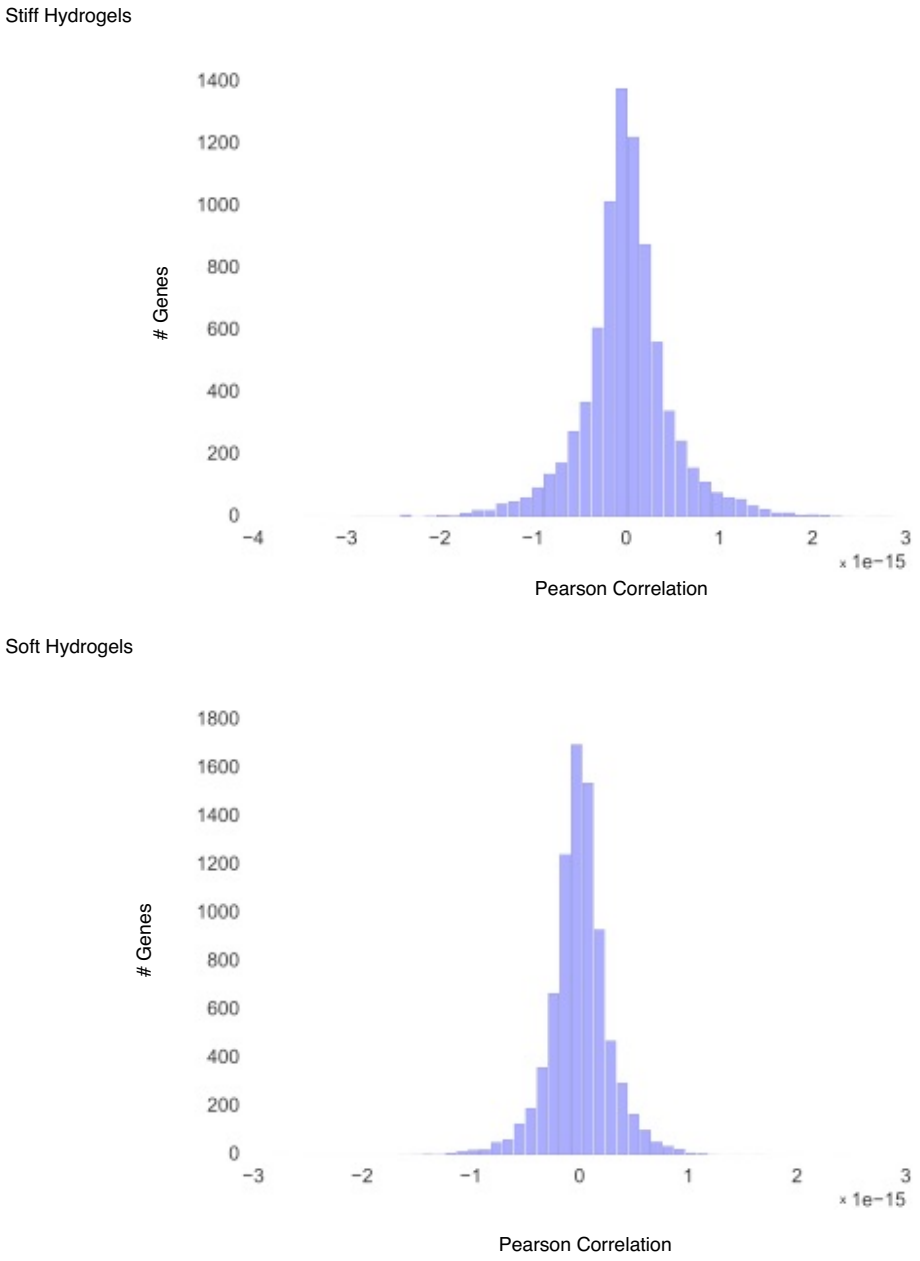

Fig. 18: Distributions across all genes of Pearson correlations of gene expression as a function of hydrogel Ca concentration for soft and stiff hydrogels. All replicates were used to calculate the correlations.

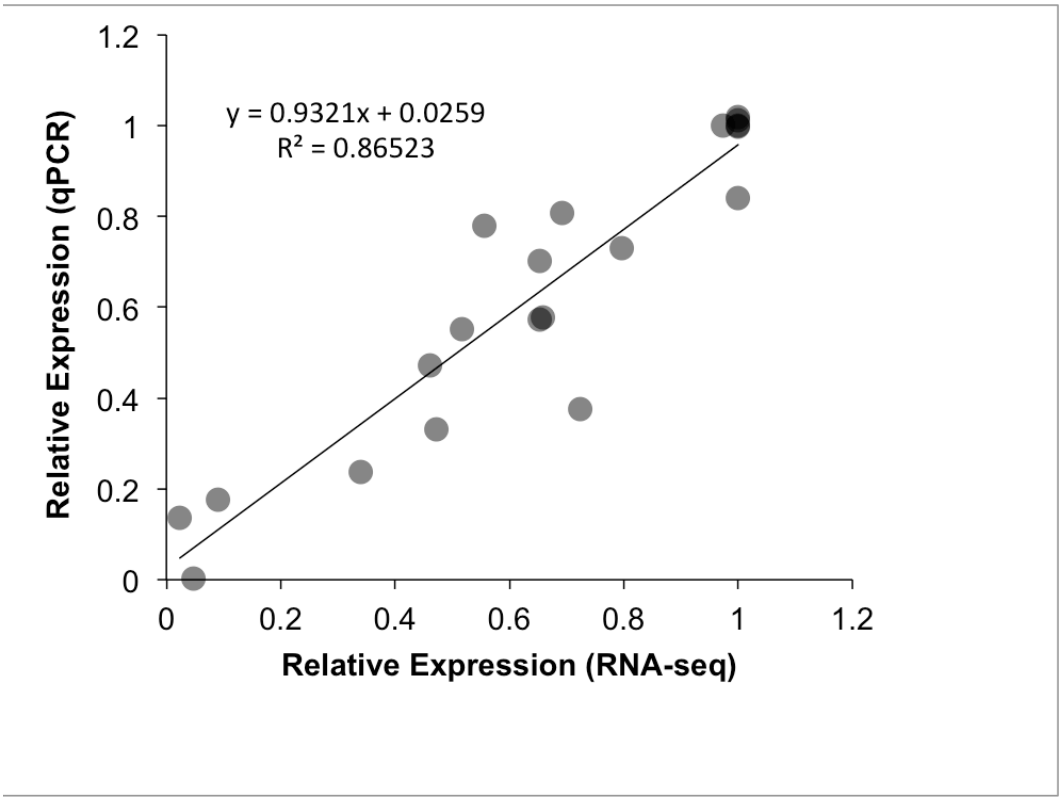

Fig. 19: Validation of RNA-seq results by qPCR. Sampled DE genes for qPCR analysis were Ptges2, E2F7, Bmp3, Zyx, Klf6. This validation experiment was carried out in slow-relaxing soft LLD, slow-relaxing stiff LLD, slow-relaxing soft HLD, and slow-relaxing stiff HLD hydrogels. Each data point represents a specific transcript for a specific material.

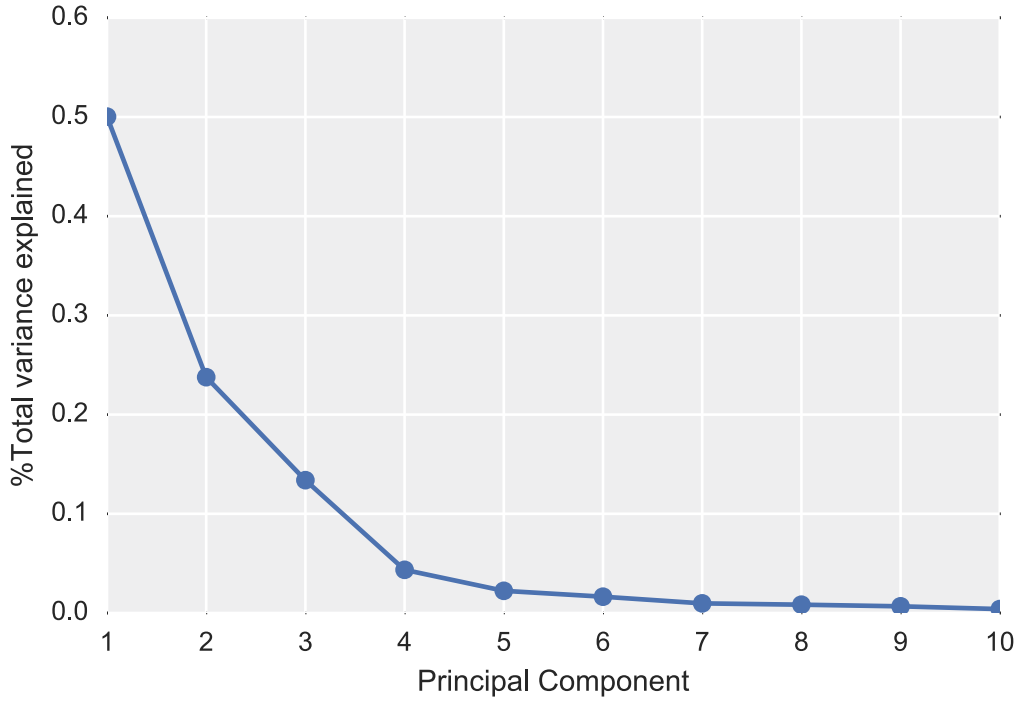

Fig. 20: % of variance described by each principal component.

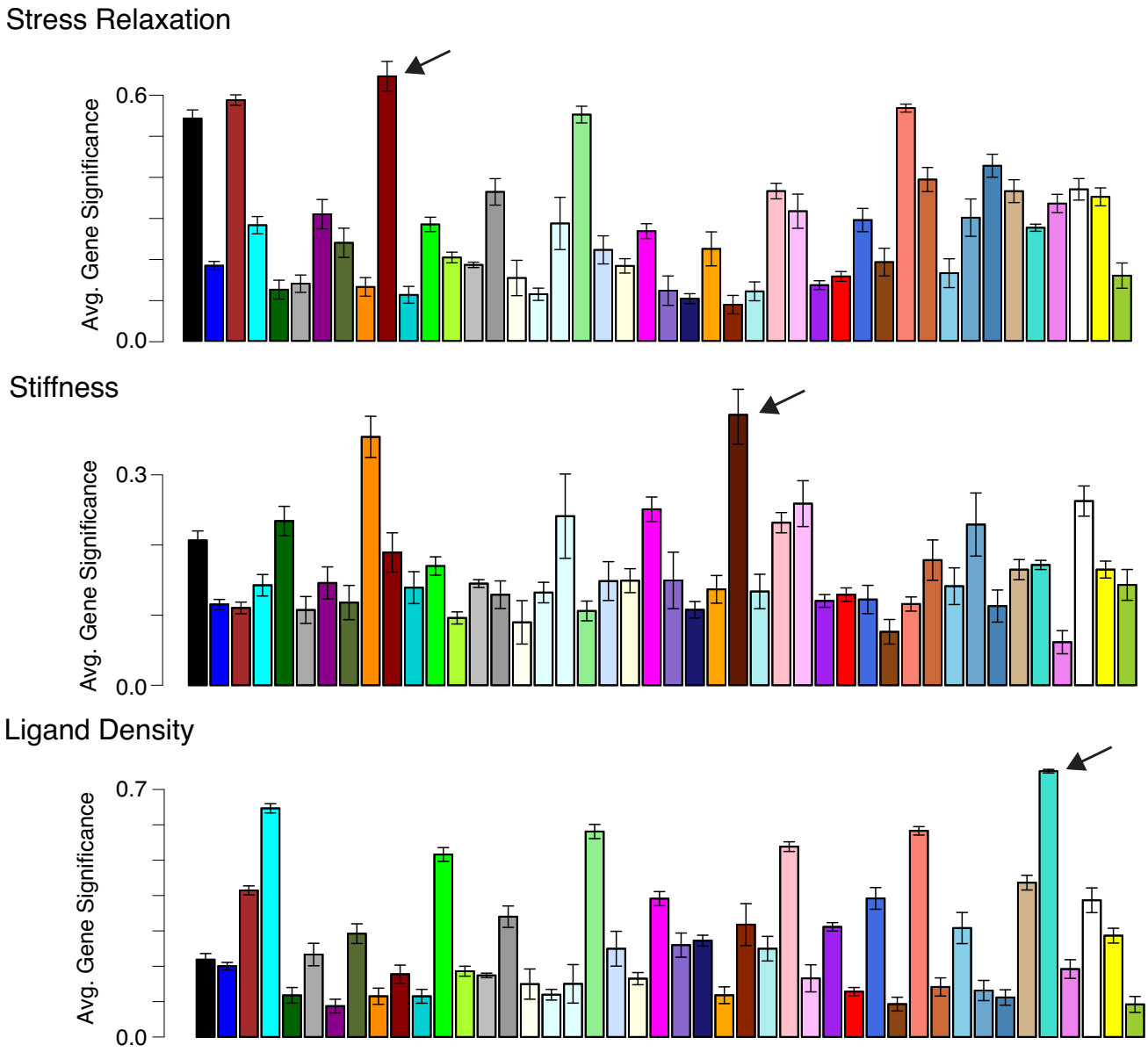

Figure 21: Identification of WGCNA modules corresponding to material parameter of interest. Average gene significance for each module with respect to each parameter. The most significant modules were chosen for further analysis and are highlighted with arrows. Error bars represent S.D.

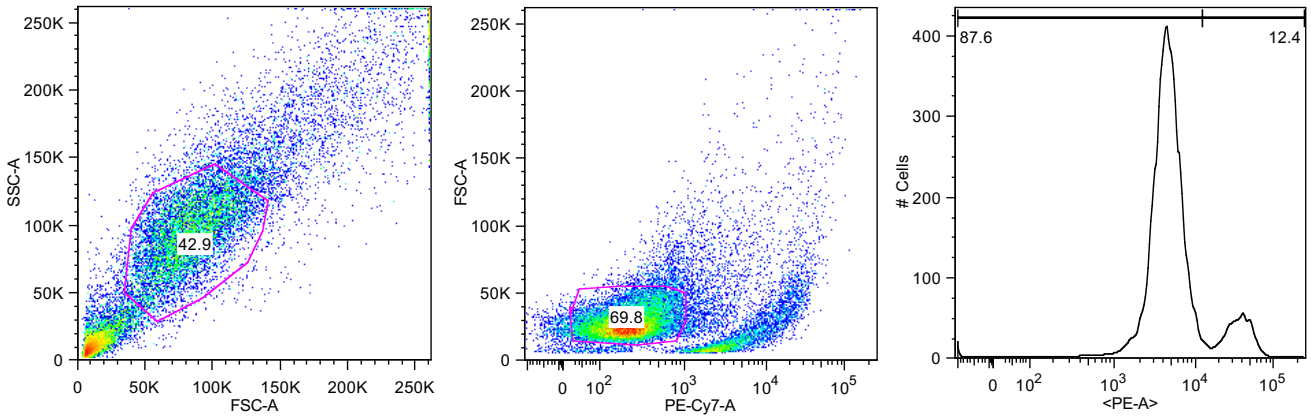

Fig. 22: Examples of gates for FSC/SSC (left), Live Cells (middle), and Stain +/- Cells (right).

Supplemental Tables

Supplier	Number	Antigen	Concentration
Abcam	ab92486	TGF-beta	1 µg/mL
Abcam	ab23672	COX-2	1 µg/mL
Abcam	ab91655	OPN	1 µg/mL
BioLegend	122402	IDO	1 µg/mL
ThermoFisher	MA5-23547	SDF-1	1 µg/mL
Santa Cruz	sc-22538	OSX	1 µg/mL
Cell Signaling	3033S	Phospho-NF-κB p65 (Ser536)	1 µg/mL
Cell Signaling	13008S	Phospho-YAP (Ser127)	1 µg/mL

Table S1: Source and concentrations of antibodies used for flow cytometry.

Supplier	Unique Assay ID	Gene
BioRad	qMmuCID0005139	Ptges2
BioRad	qMmuCID0018612	Gapdh
BioRad	qMmuCID0008584	Bmp3
BioRad	qMmuCID0010274	E2F7
BioRad	qMmuCID0006114	Zyx
BioRad	qMmuCID0016866	Klf6

Table S2: PCR primers used for RNAseq validation

Materials and Methods References

1. Lee, K. Y. & Mooney, D. J. Alginate: properties and biomedical applications. *Progress in polymer science* **37**, 106-126, doi:10.1016/j.progpolymsci.2011.06.003 (2012).
2. Alsberg, E., Anderson, K. W., Albeiruti, A., Franceschi, R. T. & Mooney, D. J. Cell-interactive Alginate Hydrogels for Bone Tissue Engineering. *Journal of Dental Research* **80**, 2025-2029 (2001).
3. Ovijit Chaudhuri, L. G., Darinka Klumpers, Max Darnell Sidi A. Bencherif, James C. & Weaver, N. H., Hong-pyo Lee, Evi Lippens, Georg N. Duda , David J. Mooney. Hydrogels with tunable stress relaxation regulate stem cell fate and activity. *Nat Materials* **Accepted** (2015).
4. Johnson, T. D. *et al.* Quantification of decellularized human myocardial matrix: A comparison of six patients. *PROTEOMICS – Clinical Applications* **10**, 75-83, doi:10.1002/prca.201500048 (2016).
5. Taroni, P. *et al.* Breast Tissue Composition and Its Dependence on Demographic Risk Factors for Breast Cancer: Non-Invasive Assessment by Time Domain Diffuse Optical Spectroscopy. *PLoS ONE* **10**, e0128941, doi:10.1371/journal.pone.0128941 (2015).
6. Legant, W. R. et al. Measurement of mechanical tractions exerted by cells in three-dimensional matrices. Nat Meth 7, 969–971 (2010).
7. Wessendorf, A. M. & Newman, D. J. Dynamic understanding of human-skin movement and strainfield analysis. IEEE Trans. Biomed. Eng. 59, 3432–3438 (2012).

8. Gordon, A. M., Huxley, A. F. & Julian, F. J. The variation in isometric tension with sarcomere length in vertebrate muscle fibres. J. Physiol. 184, 170–192 (1966).
9. Huh, D. et al. Reconstituting organ-level lung functions on a chip. Science 328, 1662–1668 (2010).
10. Liao, Y., Smyth, G. K. & Shi, W. The Subread aligner: fast, accurate and scalable read mapping by seed-and-vote. *Nucleic Acids Research* **41**, e108, doi:10.1093/nar/gkt214 (2013).
11. Liao, Y., Smyth, G. K. & Shi, W. in *Bioinformatics* (2013).
12. Law, C. W., Chen, Y., Shi, W. & Smyth, G. K. voom: precision weights unlock linear model analysis tools for RNA-seq read counts. *Genome Biology* **15**, 1-17, doi:10.1186/gb-2014-15-2-r29 (2014).
13. Smyth, G. in *Bioinformatics and Computational Biology Solutions using R and Bioconductor* (eds R. Gentleman *et al.*) (Springer, 2005).
14. Zhang, B. & Horvath, S. A General Framework for Weighted Gene Co-expression Network Analysis. *Stat Appl Genet Mol Biol* **4** (2005).
15. Presson, A. *et al.* in *BMC Systems Biology* (2008).

CHAPTER 5

Leveraging Advances in Biology to Design Biomaterials

Abstract

Biomaterials have dramatically increased in functionality and complexity, allowing unprecedented control over the cells that interact with them. From these scientific and engineering advances arises the prospect of improved biomaterial-based therapies, yet practical constraints favor simplicity. A biomaterial design approach is needed that uses these techniques to maximize functionality, yet incorporates these constraints upfront in the design process. Tools from the biology community are enabling high-resolution and high-throughput bioassays that, if incorporated into a biomaterial design framework, could help achieve unprecedented functionality while minimizing the complexity of biomaterial designs by identifying the most important material parameters and biological outputs. However, in order to avoid data explosions and to effectively match the information content of an assay with the goal of the experiment, material screens and bioassays must be arranged in specific ways. By borrowing methods to design experiments and workflows from the bioprocess engineering community, we outline a framework for the incorporation of next-generation bioassays into biomaterials design in order to effectively optimize function while minimizing complexity. The framework presented here can inspire biomaterials designs that maximize functionality and translatability.

Introduction

Recent advances in both interrogating and perturbing cells have generated a wealth of knowledge about the factors influencing cell behavior. Advances in biomaterials, in particular, have allowed engineers and biologists to not only learn about the myriad factors of a cell's material environment that affect phenotype, but also design strategies to use that influence therapeutically. Leveraging this axis of control has led to a multitude of applications, including the use of biomaterials as carriers for cell therapy[1, 2], scaffolds for tissue engineering[3], medical devices[4], and as miniature factories for manipulating the immune system[5-8].

Despite the powerful functionality of many new biomaterials, their complexity actually represents a barrier for translation into the clinic, as practical, economic, and regulatory hurdles favor simplicity. Balancing this need for simplicity with the large parameter space now available to the biomaterials engineer creates a demand for strategies to identify the biomaterial design with the minimum necessary complexity for a given application. The fine control possible over modern biomaterials need not contribute to more complex products, but rather enable more effective products that still meet translational constraints. A host of revolutionary technologies, such as next generation sequencing (NGS) and high-content imaging, that enable high-throughput and high-resolution interrogation of biological systems may allow the biomaterials engineer to test cell-material interactions along a spectrum of biological throughput and resolution. These technologies offer not only improved characterization of

materials designs, but also the prospect of uncovering novel functionality. A design strategy utilizing the right combinations of these technologies at specific stages of the design process could allow engineers to screen materials subject to arbitrary design constraints. However, these data-rich techniques must be employed in clever ways to avoid combinatorial data explosions.

In this Progress Report, we highlight the technologies signaling a new era in biomaterials development and barriers to the most effective use of these technologies, focusing on biomaterials that are designed to guide cell fate and function. By leveraging design methods from the bioprocess field, we outline a biomaterial design approach that maximally leverages recent advances in both biology and materials methods. As a case study, we illustrate how this framework could be used for developing new biomaterials for pancreatic beta cell transplantation. We propose that these ideas will aid in the development of biomaterials that do not sacrifice functionality for translatability.

Complexity in Biomaterials Design

The last several decades have seen the biomaterials field transform from the simple adoption of industrial materials for biomedical use to the leveraging by biomaterials engineers of the high degree of control afforded by appropriately designed chemical and structural features to design precise cell interactions and functions (Fig. 23). Here, we first survey a variety of prominent developments.

Advances in polymerization and coupling chemistries, and the incorporation of different chemical and molecular functionalities have driven

many biomaterial improvements. For instance, living polymerization techniques enable highly uniform and monodisperse polymer chain growth[9], while new strategies in fabricating hydrogels from artificial recombinant proteins have yielded new avenues to manipulate material properties[10]. In addition, the adoption of click chemistries for crosslinking biomaterials and coupling functional biomolecules such as adhesion peptides, nucleic acids, growth factors, and drugs to biomaterials has allowed for precise control over chemical functionalization *in situ* even in the presence of cells[11, 12]. The orientation of the coupling of these molecules can be controlled, affecting their cellular function[13, 14]. One particularly fruitful area of biomaterials chemistry has been the recapitulation of features of native ECM in controllable, synthetic systems. For example, a library of peptide mimics for adhesion ligands such as fibronectin and collagen has emerged that allows for cell adhesion by certain subsets of receptors[15]; similar advances have been made in the provision of morphogen binding and presentation peptides from hydrogels[16].

In addition to chemical functionality, the physical and structural aspects of biomaterials have also proven to be biologically important, and techniques to control have improved dramatically. Material systems have been fabricated to specifically modulate biomaterial mechanical properties such as stiffness[17, 18], viscoelasticity[19], and nonlinear elasticity[20] and subsequently shown to dramatically impact the phenotypes of cells exposed to those materials. In conjunction with the mechanical properties of a material, the nano- and micro-scale structures of biomaterials exert potent effects on cells[21]. A variety of

techniques have been developed to build porosity into materials[22, 23], while advances in self-assembly and supramolecular chemistry have allowed for a spectrum of tubular and fiber-like structures to be fabricated[24-27]. 3D printing of biomaterials is an emerging area that allows the further patterning of materials of different mechanical and structural properties in highly defined ways[28, 29].

The native extracellular matrix of tissues is dynamic, and control over the temporal properties of biomaterials has also been shown to impact cell function. Namely, numerous strategies for designing degradability exist, from hydrolysis to the incorporation of protease-cleavable crosslinks[30-32]. Efforts to temporally vary biomaterial mechanical properties similar to what is seen during development have also been successful, as cells have been shown to retain a memory of their mechanical environments[33-35]. Sequential delivery of morphogens from biomaterials, mimicking the temporal action of these agents during development, has also been used to control tissue formation with a variety of approaches[36, 37]. Combining the dynamic physical and chemical aspects of native ECM, recent work has demonstrated the ability for synthetic hydrogel systems to support organoid and stem cell culture previously only possible through chemically undefined, complex natural ECM systems such as matrigel[38].

Recent innovations in material screening technologies have aided in the discovery of new biomaterials and the identification of material parameter combinations that influence cell fate and function in desired ways. For instance, arrays of artificial stem cell niches have been fabricated in microwells in order to assay stem cell differentiation or maintenance as a function of these niche

parameters[39-41]. Combinatorial chemistry techniques can be applied to discover biomaterials with novel functionality by arraying spots of randomly combined monomers from a chemical library and testing the surface chemistry or biological functionality of each combination[42]. Droplet microfluidics has also recently been applied to biomaterial screening. In this approach, materials are often polymerized on-chip around individual cells, allowing for the study of these materials on a single cell basis[43-45].

Advanced Biology Techniques Relevant to Biomaterial Design

Methods for assaying biology in unprecedented throughput and resolution have emerged, many of which could potentially be applied to biomaterials development (Fig. 23). One class of methods surrounds assaying the high-resolution molecular state of the cell. In particular, transcriptomic methods such as qPCR and RNA-seq have offered an unparalleled global view of the cell's transcriptional landscape, while proteomics is emerging as a complementary technology that captures the rich post-translational modifications that represent an increasingly important level of regulation. Meanwhile, methods for epigenomic profiling such as Hi-C[46], FAIRE-seq[47], and ATAC-seq[48] give a snapshot of the epigenetic status of a cell, capturing genome-scale regulation. Glycobiology is emerging as an area important to diverse cellular processes and proteomics techniques are being increasingly employed to understand how these post-translational modifications impact protein function[49, 50].

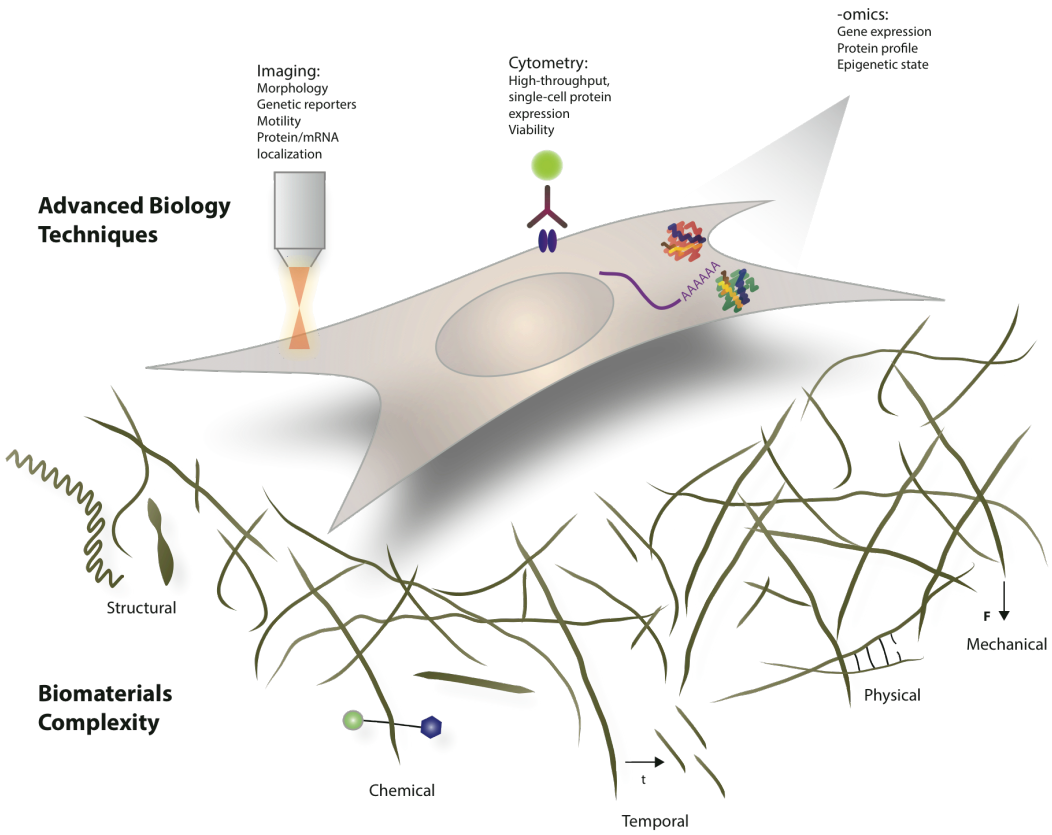

Figure 23: Advances in biomaterials fabrication and bioassays. Biomaterials fabrication has advanced along several axes of control, while bioassays have advanced along spectra of data dimensionality and throughput. The concerted merging of these techniques offers strategies for biomaterials design.

Some of these technologies have been coupled with microfluidic technology to enable the single-cell profiling of the transcriptome[51, 52], proteome[53], and epigenome[54], which provides information about the distribution of these outputs across a population of cells. These technologies offer high-throughput molecular analysis, while technologies such as mass cytometry seek to expand the multiplexing capability of flow cytometry[55].

Advances in imaging have also revolutionized biology in the last several decades. In particular, super-resolution imaging methods have allowed for sub-diffraction limit imaging of labeled biomolecules, revealing previously hidden

biology[56]. At the same time, methods for imaging extremely large samples at high resolution enable a new view of the structure of tissues. For example, full developing embryos have been imaged dynamically using lightsheet microscopy[57], while intact organs have been imaged at high resolution using CLARITY[58]. Additionally, driven by phenotypic screening in the pharmaceutical industry, high-content screening enables the multiplexed imaging of fluorescent reporters, cell morphology, and cell motility in thousands of samples in parallel[59]. The survey of techniques presented here is not comprehensive, but serves to illustrate the spectrum of methods that a biomaterials engineer has at their disposal.

The Importance and Challenge of Marrying Advanced Biology and Next-Generation Biomaterial Development

The marriage of advanced biology techniques with state of the art biomaterials control could yield unprecedented materials functionality. Yet translation of the myriad of new biomaterials currently under development must account for the practical, economic and regulatory constraints imposed on complex combination products, such as biomaterials that incorporate biologics, drugs, or cells[60-62], and the reluctance of the medical industry to introduce new biomaterial chemistries into the body[63]. Incorporating additional components and complexity generates a multitude of issues that must be addressed. For instance, increasing the complexity of a design raises not just the synthesis and fabrication technical complexity and costs, but also the number of quality control steps. More

components leads to a more complicated supply chain, increases the chances of shelf life concerns or external environmental influences affecting the product, and makes failure mode analysis more complex, among others[63]. Altogether, these emphasize the importance of both defining the minimum necessary complexity to achieve the desired biological response, and optimizing the biomaterial design as early as possible, as one is unlikely to get multiple opportunities to navigate these issues at late stages of product development and clinical trials.

Combining high-throughput and high-resolution control over material chemistry and physical properties with high-throughput and high-resolution biological assays is one promising avenue to address these challenges. Fully utilizing the biology techniques in biomaterials development would simultaneously allow the biomaterials engineer to more effectively screen material variants by identifying the best biomarkers for a given desired phenotype, while a subsequent high-resolution look at the resulting phenotypes would give a more complete view of the effects of the materials on the cells[64]. This would allow for a fuller exploration of the design space, yielding designs that could potentially satisfy functional, economic and regulatory constraints in non-intuitive ways.

Despite the appeal of combining these techniques, the mixing and matching of material screening with biology methods can quickly lead to a data explosion. For example, performing a broad transcriptomic analysis on thousands of combinatorial material variants would produce terabytes of data and likely be cost and throughput-prohibitive[64]. A step-wise approach to biomaterial design is

clearly needed, in which data-intensive methods such as combinatorial screening and RNA-seq are used to identify the most high-leverage material parameters and biological outputs, respectively, while lower-throughput methods such as narrow parameter sweeps and functional assays are used later in the process to fine-tune the design.

Attempts to date to marry next-generation biology techniques with biomaterials development have demonstrated the potential of the approach, but have mostly either sacrificed screening throughput for resolution or visa versa[64]. Hence, these attempts would have difficulty scaling to a translational environment, where the increased number of constraints dictates that one needs both high resolution and throughput to effectively find acceptable designs.

Design Strategies Borrowed from Bioprocess Engineering

Next-generation biomaterial design will likely involve optimizing a biological and thus inherently non-deterministic output by tuning parameters in a high-dimension design space. Unlike many other areas of engineering, constitutive equations that can be used to analytically optimize these designs often simply do not exist for biological systems. However, this design challenge is not without precedent. The bioprocess engineering field involves upstream process issues such as finding optimal sets of cell strain/line characteristics and culture conditions, and downstream process constraints such as purification in order to maximize the output of a pharmaceutical or industrial product. Techniques used in upstream bioprocess engineering such as design of experiments (DOE) and

biomarker identification and validation are likely to be applicable to finding the most high-leverage material and biological parameters, respectively, in biomaterials design.

Bioprocesses feature many adjustable parameters, including temperature, pH, feedstock characteristics, and cell density. Testing all possible combinations of parameters to determine the best performing set is not practical, so DOE approaches save significant resources by capturing key characteristics of the parameter space by only sampling a subset. For example, fractional factorial designs such as Box-Behnken and Placket-Burman have been used successfully to dramatically reduce the number of experiments needed to identify dominant design parameters through clever sampling of the possible parameters space[65-68]. Since these methods vary multiple parameters simultaneously to find an optimal design, they reduce the likelihood of finding only a local optimum, as can result from approaches that attempt to tune one parameter at a time. Once a small number of the most dominant parameters have been identified, experiments are performed using all combinations of two or three values of each parameter, ideally bounding the global optimal solution. The response to each of these combinations maps a solution space that can be used to further tune the parameters, an approach referred to as response surface methodology (RSM)[65, 68]. In addition to these purely empirical approaches, if prior knowledge informs a relationship of how cells are known to respond to certain inputs, such as cell metabolism as a function of media glucose concentration, mathematical models can be used to reduce the number of experiments performed by both decreasing

the number of experimental parameters and by offering the possibility of analytically solving for an optimal solution[65-68]. It should be noted that if the response is especially nonlinear or stochastic, a larger number of experiments could be necessary to capture the behavior.

Upstream bioprocess optimization also involves identifying the set of biomarkers that are most predictive of success without the need for testing the entire manufacturing process to screen individual designs. Chinese Hamster Ovary (CHO) cells are the most commonly used mammalian platform for biomolecule production in the pharmaceutical industry[69]. Recent mapping of the CHO reference genome, metabolic profile, and proteome has given engineers a benchmark against which to reverse engineer successful process designs[69, 70]. For example, by comparing two processes and seeing which produces a higher titer product, engineers can now compare the transcriptomes, proteomes, and metabolomes from those two processes to each other and to the reference. This reverse engineering has led to new biomarkers as well as the identification of key pathways and processes most strongly tied to differences in output, directly leading to improvements in cell line development and culture conditions[69, 70]. However, despite the use of DOE techniques, using the above approaches invariably still leads to large biological datasets. Key features such as signaling pathway activity or biomarkers must be extracted from that data. Principal component analysis, hierarchical and k-means clustering, and Kalman filtering are all mature methods for extracting these important features, while artificial neural networks are emerging as a powerful tool for dealing with the most otherwise

intractable datasets[65, 67, 71]. The bioengineer could use these techniques to identify biomarkers that are most strongly correlated to the desired function of the material or to specific material parameters, enabling screening to be performed with the most informative outputs. This approach is of course dependent on the existence of such biomarkers.

Potential Next-Generation Biomaterial Design Framework

We propose that next-generation biomaterial design should maximally leverage the advantages of the available technologies in order to optimize designs in a high-dimension, yet highly-constrained design parameter space. The DOE and biomarker identification techniques mentioned above are directly applicable to biomaterials, but the design problem is overall markedly different. For example, in design of cell-interacting biomaterials, oftentimes the desired phenotype is defined by a specific set of molecular markers, a functional output, or a combination of the two, instead of merely maximizing the yield and purity of a biomolecule. These outputs could even respond in coupled, nonlinear, or stochastic ways. Additionally, because of regulatory and manufacturing considerations, the number of inputs and components should be minimized in a biomaterial. Hence the strategy for the placement of various techniques will likely need to differ.

We propose a framework for the design process that can be divided into three phases: screening, surface response, and optimization (Fig. 24). In the screening phase, materials are fabricated in combinations of the controllable parameters per a full or partial factorial design, depending on the number of

parameters. Cells are then exposed to these materials in 2D or 3D culture, depending on the end-use case and if the outputs being screened are dependent on phenotypic differences between 2D and 3D culture. If reliable biomarkers for the desired phenotype already exist, either genetic reporters or other outputs amenable to highly parallel interrogation can be used. Otherwise, a trial experiment using a small number of material parameter combinations followed by proteomics or transcriptomics can identify biomarkers that are both sensitive to the material parameters being tested and related to the desired phenotype. The large material screen can then be performed using these markers, allowing the engineer to identify the minority of parameters that have the largest effects. This selection of the smallest possible number of important parameters is critical to simplifying the design.

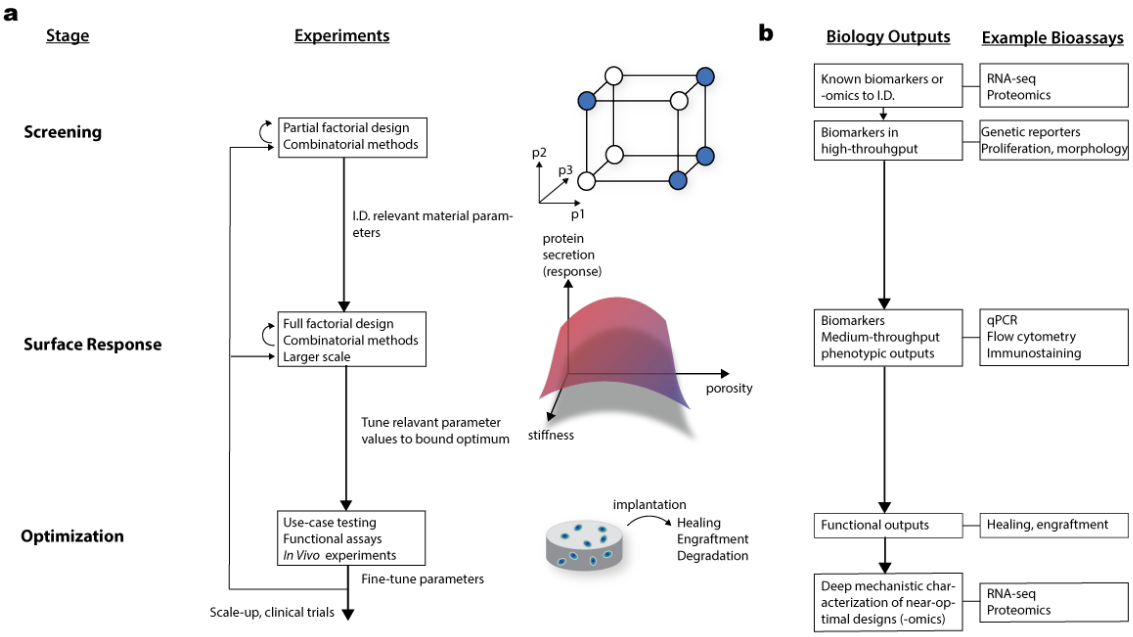

Figure 24: General next-generation biomaterial design framework. A) Experimental designs and workflow. B) Associated bioassays for each design stage.

At this point, a small number of material parameters will have been found to have the largest impact on the phenotype of the cells. Since the complexity of the material will scale with the number of design parameters, the ability to select the most high-leverage parameters is critical. The design process moves into the response surface phase, where the individual values of these parameters are tuned. At this phase, the scale and duration of the cultures and the complexity of outputs can also be increased since the experimental space has been reduced. In this way, more subtle differences in designs can also be captured. This stage can be iterated as necessary to converge on near-optimal designs.

Once a small number of near-optimal designs have been found *in vitro*, they can be moved to functional and use-case testing. For a biomaterial designed to support the culture of certain primary cell types, this functional testing could involve testing cells from many individual donors. For a regenerative medicine or tissue engineering application, this testing would involve *in vivo* studies. The previous steps are intended to have produced near-optimal candidate designs, with the goal that the smaller parameter space explored by these relatively low-throughput experiments is not as costly. However, as issues with these candidate designs arise, these results can be fed back into the screening stage as different or additional parameters, or into the surface response stage as expanded parameter ranges or different constraints. Finally, once a successful design has been found in the final stage, high-resolution biology techniques such as –omics technologies

can be revisited to fully characterize the design before moving forward with the next stages of translation, whether that is scale-up or a clinical trial.

As an example of the application of this framework to a current biomaterials design challenge, Box 1 outlines an example approach to develop an optimal biomaterial coating for pancreatic beta cell transplantation. The general approach outlined here more closely resembles traditional engineering design in that engineering specifications are taken into account early in the design process and drive all stages of product development, as opposed to optimizing a design independent of these constraints and attempting to incorporate them later. This aspect aids in simplifying designs as less critical design parameters are eliminated earlier in the design process. It is also flexible enough to incorporate technologies that can be tailored to the individual problem.

BOX 1
Integrative Biomaterial Design Challenge: Cell carrier for β-cell transplantation

Background:
Type I Diabetes Mellitus (T1DM) involves the autoimmune destruction of the insulin-producing β-cells of the pancreatic islets. Transplantation of allogeneic or xenogeneic islets has long been seen as a promising therapeutic strategy[72]. However, since transplantation of free islets requires the patient to undergo lifelong immunosuppression, biomaterial-based delivery strategies that obviate the need for immunosuppression have been developed[72], and strategies such as transplantation site pre-vascularization have also been introduced[73]. Moreover, limitations in islet availability and donor-donor variability have driven attempts to produce β-cells directly from autologous or allogeneic pluripotent stem cells as the transplanted cell source[74]. The convergence of biology and materials trends promise to dramatically enhance the efficacy of cell therapy to treat T1DM.

Hydrogels have been developed as -cell carriers to allow diffusion of small soluble species such as insulin and glucose between the host and the cells, while physically and chemically localizing the cells to a specific anatomic location, and isolating the transplanted cells from immune cells and their secreted factors such as antibodies. Islet-laden hydrogel microcapsules can bypass the need for immunosuppression, and can be injected to lodge in small-diameter vessels, usually in the kidney, liver, or omentum[72]. These capsules provide a supportive substrate to the cells, aiding in viability and function, but the optimal hydrogel to provide these functions is unknown. In addition, most examples feature capsules that are significantly larger than the islets themselves, presenting a diffusion barrier and thus a lag in the response to glucose challenge. Variability in the islet size also represents a challenge for optimizing the microcapsules[72]. Conformal coating of small numbers of cells increases the number of potential transplantation sites and prevents the formation of a hypoxic core in the collection of encapsulated cells[72, 75]. One can also incorporate islets into larger-scale biomaterial devices, as these facilitate the retrieval of the device from the patient[72], but the islets are again often encapsulated within a hydrogel within these devices. Recent work has demonstrated that β-cells transplanted via material carriers can induce a long-term insulin response without inducing fibrosis[2], demonstrating the promise of this approach, but the large parameter space available to the materials engineer for this application is still very underexplored, suggesting room for improvements.

Design Approach:
Many islet and β-cell transplantation strategies involve encapsulating cells in a hydrogel matrix. Thus, we here focus on designing hydrogels with optimal characteristics for β-cell transplantation. After optimization of the cell-material interaction, the material could be used in a variety of schemes such as conformal coating for intravascular injection or as the central reservoir of a macroencapsulation device. Given the potential plasticity in this cell source, careful characterization of the cells in each stage of the design process is important. For instance, donor variability could impact a beta cell's response to a material, highlighting the need for the ability to include donor-donor variability upfront in the design process and the importance of involving advanced bioassays in biomaterials development.

Biomaterial Design Specifications:
- Not cytotoxic
- Be able to support adhesion, viability, and insulin production of β-cells reliably across donors
- Be able to support diffusion of insulin, glucose, and cellular metabolism waste products
- Feature small pore size to prevent invasion of autoreactive T cells or outward migration of -cells, as well as diffusion of antibodies
- Provide sufficiently thick coating to minimize effects of rapidly-decaying, reactive oxygen species released by immune cells
- Not pro-inflammatory or fibrosis-inducing
- Be able to image *in vivo* to evaluate engraftment

Example Design Framework:

Note that for each phase, iteration might be necessary to achieve desired outputs.

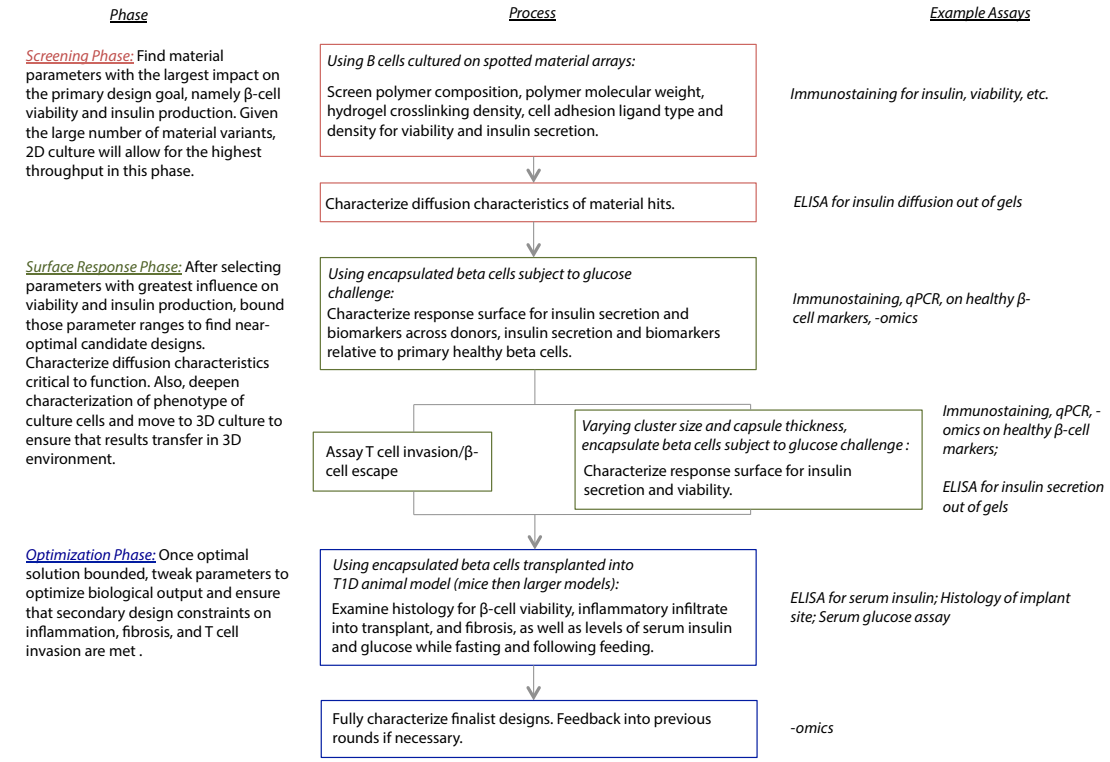

Conclusions

Biomaterials design now has the opportunity to benefit from the advances of both materials fabrication and bioassays. The vast experimental space available to the bioengineer necessitates a concerted design methodology but also calls for the use of experimental design and optimization techniques commonly used in other areas of engineering. Through the framework presented here, bioengineers could effectively explore the design space in order to simplify the design as much as possible upfront while still maximizing the functionality. We hope that through such a framework, biomaterials design can become even more rational and quantitative. Since a large design space can potentially be more effectively explored and more deeply characterized, functionality can be maximized and engineering specifications imposed by clinical or industrial translation will hopefully present a lower barrier, improving the chances for translational success of biomaterials.

References

1. Han, W.M. et al. Microstructural heterogeneity directs micromechanics and mechanobiology in native and engineered fibrocartilage. *Nat Mater* **15**, 477-484 (2016).
2. Vegas, A.J. et al. Long-term glycemic control using polymer-encapsulated human stem cell-derived beta cells in immune-competent mice. *Nat Med* **22**, 306-311 (2016).
3. Zhang, B. et al. Biodegradable scaffold with built-in vasculature for organ-on-a-chip engineering and direct surgical anastomosis. *Nat Mater* **15**, 669-678 (2016).
4. Singh, A. et al. Enhanced lubrication on tissue and biomaterial surfaces through peptide-mediated binding of hyaluronic acid. *Nat Mater* **13**, 988-995 (2014).

5. Ali, O.A., Huebsch, N., Cao, L., Dranoff, G. & Mooney, D.J. Infection-mimicking materials to program dendritic cells in situ. *Nat Mater* **8**, 151-158 (2009).
6. Moon, J.J. et al. Interbilayer-crosslinked multilamellar vesicles as synthetic vaccines for potent humoral and cellular immune responses. *Nat Mater* **10**, 243-251 (2011).
7. DeMuth, P.C. et al. Polymer multilayer tattooing for enhanced DNA vaccination. *Nat Mater* **12**, 367-376 (2013).
8. Kuai, R., Ochyl, L.J., Bahjat, K.S., Schwendeman, A. & Moon, J.J. Designer vaccine nanodiscs for personalized cancer immunotherapy. *Nat Mater* **advance online publication** (2016).
9. DiPasquale, S.A. & Byrne, M.E. Controlled architecture for improved macromolecular memory within polymer networks. *Current Opinion in Biotechnology* **40**, 170-176 (2016).
10. Dooling, L.J., Buck, M.E., Zhang, W.-B. & Tirrell, D.A. Programming Molecular Association and Viscoelastic Behavior in Protein Networks. *Advanced Materials* **28**, 4651-4657 (2016).
11. Jiang, Y., Chen, J., Deng, C., Suuronen, E.J. & Zhong, Z. Click hydrogels, microgels and nanogels: Emerging platforms for drug delivery and tissue engineering. *Biomaterials* **35**, 4969-4985 (2014).
12. Wang, L.L. & Burdick, J.A. Engineered Hydrogels for Local and Sustained Delivery of RNA-Interference Therapies. *Advanced Healthcare Materials* **6**, 1601041-n/a (2017).
13. Alberti, K. et al. Functional immobilization of signaling proteins enables control of stem cell fate. *Nat Meth* **5**, 645-650 (2008).
14. DeForest, C.A. & Tirrell, D.A. A photoreversible protein-patterning approach for guiding stem cell fate in three-dimensional gels. *Nat Mater* **14**, 523-531 (2015).
15. Ruoslahti, E. RGD AND OTHER RECOGNITION SEQUENCES FOR INTEGRINS. *Annual Review of Cell and Developmental Biology* **12**, 697-715 (1996).
16. Mitchell, A.C., Briquez, P.S., Hubbell, J.A. & Cochran, J.R. Engineering growth factors for regenerative medicine applications. *Acta Biomaterialia* **30**, 1-12 (2016).
17. Engler, A.J., Sen, S., Sweeney, H.L. & Discher, D.E. Matrix elasticity directs stem cell lineage specification. *Cell* **126** (2006).
18. Cosgrove, B.D. et al. N-cadherin adhesive interactions modulate matrix mechanosensing and fate commitment of mesenchymal stem cells. *Nat Mater* **15**, 1297-1306 (2016).
19. Chaudhuri, O. et al. Hydrogels with tunable stress relaxation regulate stem cell fate and activity. *Nat Mater* **15**, 326-334 (2016).
20. Hall, M.S. et al. Fibrous nonlinear elasticity enables positive mechanical feedback between cells and ECMs. *Proceedings of the National Academy of Sciences* (2016).

21. Dalby, M.J., Gadegaard, N. & Oreffo, R.O.C. Harnessing nanotopography and integrin-matrix interactions to influence stem cell fate. *Nat Mater* **13**, 558-569 (2014).
22. Annabi, N. et al. Controlling the Porosity and Microarchitecture of Hydrogels for Tissue Engineering. *Tissue Engineering. Part B, Reviews* **16**, 371-383 (2010).
23. Bencherif, S.A. et al. Injectable cryogel-based whole-cell cancer vaccines. *Nature Communications* **6**, 7556 (2015).
24. Freeman, R., Boekhoven, J., Dickerson, M.B., Naik, R.R. & Stupp, S.I. Biopolymers and supramolecular polymers as biomaterials for biomedical applications. *MRS Bulletin* **40**, 1089-1101 (2015).
25. Han, L.-H., Yu, S., Wang, T., Behn, A.W. & Yang, F. Microribbon-Like Elastomers for Fabricating Macroporous and Highly Flexible Scaffolds that Support Cell Proliferation in 3D. *Advanced Functional Materials* **23**, 346-358 (2013).
26. Hudalla, G.A. et al. Gradated assembly of multiple proteins into supramolecular nanomaterials. *Nat Mater* **13**, 829-836 (2014).
27. Sun, F., Zhang, W.-B., Mahdavi, A., Arnold, F.H. & Tirrell, D.A. Synthesis of bioactive protein hydrogels by genetically encoded SpyTag-SpyCatcher chemistry. *Proceedings of the National Academy of Sciences of the United States of America* **111**, 11269-11274 (2014).
28. Homan, K.A. et al. Bioprinting of 3D Convoluted Renal Proximal Tubules on Perfusable Chips. *Scientific Reports* **6**, 34845 (2016).
29. Kolesky, D.B., Homan, K.A., Skylar-Scott, M.A. & Lewis, J.A. Three-dimensional bioprinting of thick vascularized tissues. *Proceedings of the National Academy of Sciences of the United States of America* **113**, 3179-3184 (2016).
30. Zhu, J. & Marchant, R.E. Design properties of hydrogel tissue-engineering scaffolds. *Expert review of medical devices* **8**, 607-626 (2011).
31. Luo, Y. & Shoichet, M.S. A photolabile hydrogel for guided three-dimensional cell growth and migration. *Nat Mater* **3**, 249-253 (2004).
32. Mosiewicz, K.A. et al. In situ cell manipulation through enzymatic hydrogel photopatterning. *Nat Mater* **12**, 1072-1078 (2013).
33. Yang, C., Tibbitt, M.W., Basta, L. & Anseth, K.S. Mechanical memory and dosing influence stem cell fate. *Nat Mater* **13**, 645-652 (2014).
34. Tibbitt, M.W. & Anseth, K.S. Dynamic Microenvironments: The Fourth Dimension. *Science Translational Medicine* **4**, 160ps124 (2012).
35. Jeon, H. et al. Directing cell migration and organization via nanocrater-patterned cell-repellent interfaces. *Nat Mater* **14**, 918-923 (2015).
36. Mehta, M., Schmidt-Bleek, K., Duda, G.N. & Mooney, D.J. Biomaterial delivery of morphogens to mimic the natural healing cascade in bone. *Advanced Drug Delivery Reviews* **64**, 1257-1276 (2012).
37. Lee, T.T. et al. Light-triggered in vivo activation of adhesive peptides regulates cell adhesion, inflammation and vascularization of biomaterials. *Nat Mater* **14**, 352-360 (2015).

38. Gjorevski, N. et al. Designer matrices for intestinal stem cell and organoid culture. *Nature* **539**, 560-564 (2016).
39. Ranga, A. et al. 3D niche microarrays for systems-level analyses of cell fate. *Nature Communications* **5**, 4324 (2014).
40. Kobel, S. & Lutolf, M. High-throughput methods to define complex stem cell niches. *Biotechniques* **48**, ix-xxii (2010).
41. Mei, Y. et al. Combinatorial development of biomaterials for clonal growth of human pluripotent stem cells. *Nat Mater* **9**, 768-778 (2010).
42. Hook, A.L. et al. High throughput methods applied in biomaterial development and discovery. *Biomaterials* **31**, 187-198 (2010).
43. Shembekar, N., Chaipan, C., Utharala, R. & Merten, C.A. Droplet-based microfluidics in drug discovery, transcriptomics and high-throughput molecular genetics. *Lab on a Chip* **16**, 1314-1331 (2016).
44. Mao, A.S. et al. Deterministic encapsulation of single cells in thin tunable microgels for niche modelling and therapeutic delivery. *Nat Mater* **16**, 236-243 (2017).
45. Brandenberg, N. & Lutolf, M.P. In Situ Patterning of Microfluidic Networks in 3D Cell-Laden Hydrogels. *Advanced Materials* **28**, 7450-7456 (2016).
46. Belton, J.-M. et al. Hi-C: A comprehensive technique to capture the conformation of genomes. *Methods (San Diego, Calif.)* **58**, 10.1016/j.ymeth.2012.1005.1001 (2012).
47. Giresi, P.G., Kim, J., McDaniell, R.M., Iyer, V.R. & Lieb, J.D. FAIRE (Formaldehyde-Assisted Isolation of Regulatory Elements) isolates active regulatory elements from human chromatin. *Genome Research* **17**, 877-885 (2007).
48. Buenrostro, J.D., Giresi, P.G., Zaba, L.C., Chang, H.Y. & Greenleaf, W.J. Transposition of native chromatin for fast and sensitive epigenomic profiling of open chromatin, DNA-binding proteins and nucleosome position. *Nat Meth* **10**, 1213-1218 (2013).
49. Bennun, S.V. et al. Systems Glycobiology: Integrating Glycogenomics, Glycoproteomics, Glycomics, and Other 'Omics Data Sets to Characterize Cellular Glycosylation Processes. *Journal of Molecular Biology* **428**, 3337-3352 (2016).
50. Babu, P. Glycans in Regeneration. *ACS Chemical Biology* **9**, 96-104 (2014).
51. Macosko, E.Z. et al. Highly parallel genome-wide expression profiling of individual cells using nanoliter droplets. *Cell* **161**, 1202-1214 (2015).
52. Klein, Allon M. et al. Droplet Barcoding for Single-Cell Transcriptomics Applied to Embryonic Stem Cells. *Cell* **161**, 1187-1201.
53. Angelo, M. et al. Multiplexed ion beam imaging of human breast tumors. *Nat Med* **20**, 436-442 (2014).
54. Rotem, A. et al. Single-cell ChIP-seq reveals cell subpopulations defined by chromatin state. *Nature biotechnology* **33**, 1165-1172 (2015).
55. Depince-Berger, A.E., Aanei, C., Iobagiu, C., Jeraiby, M. & Lambert, C. New tools in cytometry. *Morphologie* **100**, 199-209 (2016).

56. Fujita, K. Follow-up review: recent progress in the development of super-resolution optical microscopy. *Microscopy* **65**, 275-281 (2016).
57. Chen, B.-C. et al. Lattice light-sheet microscopy: Imaging molecules to embryos at high spatiotemporal resolution. *Science* **346** (2014).
58. Chung, K. et al. Structural and molecular interrogation of intact biological systems. *Nature* **497**, 332-337 (2013).
59. Bougen-Zhukov, N., Loh, S.Y., Lee, H.K. & Loo, L.-H. Large-scale image-based screening and profiling of cellular phenotypes. *Cytometry Part A*, n/a-n/a (2016).
60. Prestwich, G.D. et al. What Is the Greatest Regulatory Challenge in the Translation of Biomaterials to the Clinic? *Science Translational Medicine* **4**, 160cm114 (2012).
61. Ratcliffe, A. Difficulties in the translation of functionalized biomaterials into regenerative medicine clinical products. *Biomaterials* **32**, 4215-4217 (2011).
62. Hench, L.L. & Thompson, I. Twenty-first century challenges for biomaterials. *Journal of The Royal Society Interface* **7**, S379 (2010).
63. Amato, S.E., R Regulatory Affairs for Biomaterials and Medical Devices, Edn. 1st Edition. (Woodhead Publishing, 2014).
64. Groen, N. et al. Stepping into the omics era: Opportunities and challenges for biomaterials science and engineering. *Acta biomaterialia* **34**, 133-142 (2016).
65. Kumar, V., Bhalla, A. & Rathore, A.S. Design of experiments applications in bioprocessing: Concepts and approach. *Biotechnology Progress* **30**, 86-99 (2014).
66. Mandenius, C.-F. & Brundin, A. Bioprocess optimization using design-of-experiments methodology. *Biotechnology Progress* **24**, 1191-1203 (2008).
67. Keskin Gündoğdu, T., Deniz, İ., Çalışkan, G., Şahin, E.S. & Azbar, N. Experimental design methods for bioengineering applications. *Critical Reviews in Biotechnology* **36**, 368-388 (2016).
68. Lim, M. et al. Intelligent bioprocessing for haemotopoietic cell cultures using monitoring and design of experiments. *Biotechnology Advances* **25**, 353-368 (2007).
69. Lewis, A.M., Abu-Absi, N.R., Borys, M.C. & Li, Z.J. The use of 'Omics technology to rationally improve industrial mammalian cell line performance. *Biotechnology and Bioengineering* **113**, 26-38 (2016).
70. Wuest, D.M., Harcum, S.W. & Lee, K.H. Genomics in mammalian cell culture bioprocessing. *Biotechnology advances* **30**, 629-638 (2012).
71. Villaverde, A.F. & Banga, J.R. Reverse engineering and identification in systems biology: strategies, perspectives and challenges. *Journal of the Royal Society Interface* **11**, 20130505 (2014).
72. Scharp, D.W. & Marchetti, P. Encapsulated islets for diabetes therapy: History, current progress, and critical issues requiring solution. *Advanced Drug Delivery Reviews* **67–68**, 35-73 (2014).
73. Pepper, A.R. et al. A prevascularized subcutaneous device-less site for islet and cellular transplantation. *Nat Biotech* **33**, 518-523 (2015).

74. Pagliuca, F.W. et al. Generation of functional human pancreatic β cells in vitro. *Cell* **159**, 428-439 (2014).
75. Tomei, A.A. et al. Device design and materials optimization of conformal coating for islets of Langerhans. *Proceedings of the National Academy of Sciences of the United States of America* **111**, 10514-10519 (2014).